COHERENT OPTICAL SPECTROSCOPY OF A SINGLE SEMICONDUCTOR QUANTUM DOT

by

Xiaodong Xu

A dissertation submitted in partial fulfillment
of the requirements for the degree of
Doctor of Philosophy
(Physics)
in The University of Michigan
2008

Doctoral Commitee:

Professor Duncan G. Steel, Chair
Professor Roberto D. Merlin
Professor Theodore B. Norris
Professor Georg A. Raithel
Associate Professor Luming Duan

ACKNOWLEDGEMENTS

6 years ago when I joined the group, Elaine gave me a lab tour. I saw Jun and Yanwen sitting in the dark and taking data. At that time there was a big chiller in the time domain lab and making huge noise. Frankly, I was a bit scared since I had never been in a real lab before graduate school. I was wondering whether I could do well in such a lab as an experimental physicist. Now it is 6 years later and I am so happy to say that I made it. During the entire graduate school, there are so many people I would like to thank. The first and the most important person I would like to thank is my advisor Professor Duncan Steel. I am so lucky to have Duncan as my advisor. He is such a smart scientist with great personality. His working ethics and conscientious attitudes inspired me a lot in research. He always tries to create the best education and research support for me. One of the greatest things is that he tried to develop my weakness, exploit my strength, and carefully shape me to be a good physicist. Duncan is also an advisor with a great sense of humor and it is so much fun to work with him.

I would like to thank Professor Paul Berman. His lectures of quantum optics is the class I enjoyed most in my graduate school, which opened the door for me to the wonderful world of quantum optics. He is always there when you need help. He is so knowledgeable that whenever I walk into his office with a question, he always have an answer for me.

I would to thank my committee members: Professor Luming Duan, Roberto Merline, Ted Noriss and Georg Raithel. Although Luming is a theorist, he is so smart and understand all the experimental details that sometimes it makes me feel like he is an experimentalist. Ted is such a great lecturer that I learned a lot of optical knowledge from his classes on classical optics and ultrafast optical science. Roberto's office is next door to Duncan's. I feel like every time when I was meeting with Duncan, Roberto was there. I enjoyed all the discussions with him both on science and on the "problems" in China.

For the work in this thesis, I gave my special thanks to my collaborators: Dr. Dan Gammon's research group in NRL and Prof Lu Sham's research group in University of California at San Diego. Allan provides the best quantum dot samples in the world, which makes all the work in this thesis possible. Morgan gave me a lot of help when I started to work on the bias controlled quantum dot samples. Lu is that type of physicist who stands on top of the mountain and always gives you the best help. I would also like to thank Wang's creative thoughts on the nuclear spin control work presented in Chapter 7. Clive gave me a lot help on the theoretical calculations of the optical pumping experiment, which is presented in Chapter 5. There were also a lot of fun discussions with Matt, Danny, Michael, Sophia and Renbao, Semion in the conferences.

One of the wonderful things about working in Duncan's lab is that I always work with a group of talented people. It is impossible to finish my thesis work without the help of my labmates: Liz, Ealine, Gurudev, Jun, Yanwen, Qiong, Erik, Katherine, Bo, Vasudev, John and Chris, and the visiting scholars: Alberto and Geng. My first mentor was Ealine. She share with me her own experience and also assigned me a few small projects, which helped me a lot to get a good start in the lab. During that time, I learned the calculations for the bi-exciton system and started the first experience in the experiment. Later on, I worked with Yanwen, a very smart labmate with a lot of patience. She is a also a good friend and gave me a lot of suggestions both on science and life. I used to call her my intelligence officer No.1. After that I worked with Gurudev on the charged quantum dots system. I learned a lot from him about time domain experimental techniques, the four-level calculations, and the coherent control experiment. Those are really fun experience. Starting from my third year I worked with Jun. He is such a smart guy with great working attitude. He taught me how to use the instruments in the CW lab, which laid a foundation for my thesis work. Eirk is a great labmate to have and it is so much fun to have him around. I enjoyed all the discussions with him on science, sports, and some “spread” offenses on peach blossoms. He is also a “xiong di” and my intelligence officer No.2. I was so lucky to have Bo as my lackey since he is a super talented guy. We worked together on many experiments. He is so patient and did wonderful jobs on proof reading all my papers. Katherine also helped me a lot on proof reading some of the papers and all the thesis chapters. I also thank John and Vasudev for proof reading part of my thesis. Beyond science, I won’t forget all the fun experience I had with this wonderful group of guys, such as pot lucks, football parties, Friday lunches and the great Virginia white water rafting. I would also thank the past graduate students in the lab: Gang, Tod and Anthony. Especially Anthony gave me a lot of suggestions when I started to work on the self-assmebled quantum dots system.

I would also like to thank all my friends. The life in Ann Arbor would not have been as much fun as it was without those guys. BBQs, playing cards, sports and PC games with those guys gave me extra dimension of happiness.

Finally, I would like to thank my family. Although I cannot see them often, they always support me and encourage me whenever I talked to them. Once my mom told me that my uncle was wondering whether I was held in the graduate school because of bad grades since I did not graduate after the fifth year. She said it was ok to tell them the truth, they would always support me. The best thing in the graduate school is that I got married with Ying. It is impossible for me to finish my PhD without her support. Although she was also a PhD student, she did all the house work and took care of me very well. She also kept checking my research progress with questions like “Did you get a good QD state today?”. I was joking to her that she actually finished two PhDs. But certainly, to be married with her is the best and smartest thing I have ever done in my life.

TABLE OF CONTENTS

CHAPTER

LIST OF FIGURES

LIST OF APPENDICES

Appendix

CHAPTER 1

Introduction to Quantum Dots

Semiconductor quantum dots (QDs), which are solid state analogs of atoms, have been a hot research topic in the last decade due to their unique physical properties. A QD is a three dimensional confined solid state system. Therefore, it has atomic-like quantum properties, such as a discrete energy density of states (DOS). However, in some sense, it is better than an atom since it can be customized for new technologies and quantum electronic devices [1].

From quantum mechanics we know that the wave function of a particle can be strongly modified by quantum confinement [2]. Figure 7.1 shows the DOS as a function of the quantum confinement. For a bulk semiconductor, the DOS is a continuum, as shown in Fig. 7.1(a). When a narrow bandgap semiconductor is sandwiched by a wide bandgap semiconductor material a QW is formed, which is a one dimensional confined system. As shown in Fig. 7.1(b), the DOS has staircase shape. If a semiconductor nanostructure is two dimensionally confined, such as nanowires or nanotubes, the DOS has a Van Hove singularity [3] shown in Fig. 7.1(c). When a semiconductor heterostructure is three dimensionally confined, it is known as a QD and has a delta function-like discrete DOS, shown in Fig. 7.1(d). The atomic shell structure of a quantum dot has been shown in both a voltage-capacitance spectrum [17] and an optical luminescence spectrum [1].

The commonly used methods for growing QDs are colloidal synthesized semiconductor nanocrystals [6] by a chemical reaction process, and molecular beam epitaxy (MBE) technology. In the MBE process a two dimensional electron gas (2DEG) is generated by growing a high quality semiconductor heterostructure, such as GaAs/AlGaAs. The lateral confinement can be provided by electrostatic gates [7], a strain gradient originating from lattice mismatch [11], or monolayer thickness fluctuations of QWs [9].

QDs can have very good optical properties due to their unique structures [1, 2]. A QD can interact with light like an atom, but with a stronger interaction strength than that of an atom due to the large dipole moment of a QD. Compared to an atom, the optical dipole moment of the a QD is 1 to 2 orders of magnitude larger [15, 28]. Although a QD is embedded in a complex solid state environment, the problems which occur in higher dimensional semiconductor structures, such as many body effects [12], are strongly suppressed due to the three dimensional confinement. The suppression of many body effects in QDs was confirmed by a nonlinear optical experiment in 1998 [5] and a few recent experiments [15, 16]. In some sense, the QD system can be a better testing platform for quantum optics than an atomic system, since there is no collision broadening or Doppler broadening effects as in the atomic systems.

The QD system has a great potential for opto-electronic devices. The absorption/emission energy of a quantum dot can be controlled by bandgap engineering. By properly choosing the semiconductor materials, the quantum emission energy can be tuned from ultraviolet to near infrared. The absorption/emission energy can also be controlled by controlling the size of QDs during the growth process. For a particular QD, the absorption/emission energy can also be fine tuned through the DC Stark effect by applying a DC voltage across the QD.

In this chapter, we first review a few applications of the QD system. The thesis outline is provided afterwards.

1.1 Quantum Dot Light Emitting Diodes (LED)

As we mentioned above, since the emission colors of QDs can be tuned by controlling their sizes and components during the growth process, QDs are very promising for making LEDs. The advantages of LEDs compared to normal light bulbs are a long life time and low energy consumption. It has been estimated that the use of

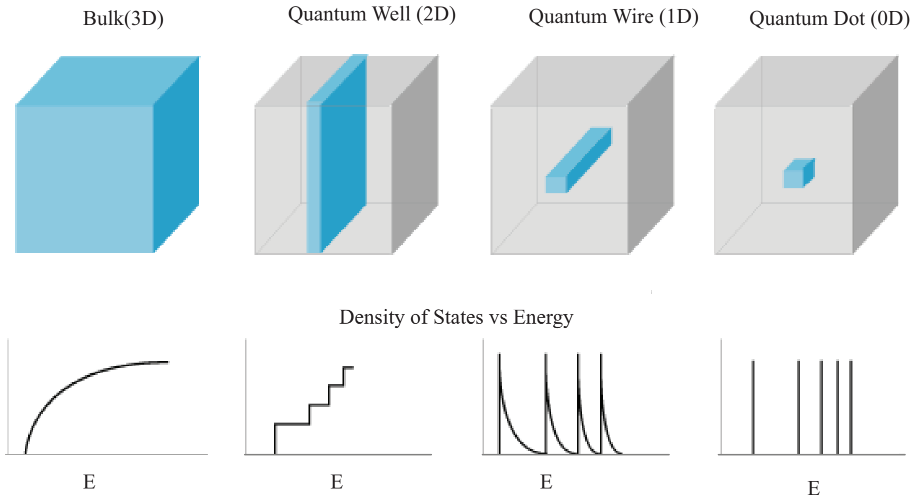

Figure 1.1: Energy Density of States as a Function of Quantum Confinement. Cartoons show the energy density of states as a function of quantum confinement

LED lighting could reduce 50% of global electricity use.

One application of LEDs is to make high quality displays. Commonly used liquid crystal displays (LCD) depend on a backlight illuminating the pixels. Each pixel has 3 sub-pixles, which correspond to red, blue and green, respectively. By adjusting the relative intensities between the three color components, the display shows all kinds of colors. There are a few drawbacks of LCDs. First, the sub-pixel is color impure, which will affect the quality of the image. Second, dark pixels just block the light which is a waste of energy. A display made of QD-LED can overcome these drawbacks [15]. Due to the three dimensional confinement, the QD has a sharp emission linewidth. Therefore, the QD-LED can output pure blue, green or red colors, which leads to high quality displays. The QD-LED emits rather than filters light, thus saving energy. The QD emission spectrum is mostly inside the visible regime, which has been shown to cover 30% more colors than Cathode ray tube (CRT). Since the QD-LED does not emits a lot of infrared light, it reduces the heat generated in the lighting process, which also leads to higher efficiency.

QD-LEDs emitting red, green and blue colors have been demonstrated in the past few years [16]. One example is a research group in MIT that produced hybrid QD-LED devices [17]. The QDs used were CdSe colloidal synthesized core-shell QDs. A single layer of QDs were sandwiched by two organic thin films. The electro-luminescence was generated by applying a bias across the device. Due to the narrow emission bandwidth, 32nm for their devices, a specific color can be produced by the QD-LED devices. A company, named QD VISION in MA, has made a 32×64 pixel monochromatic QD-LED display in 2006. In the future, it is possible to use these low energy consuming QD-LEDs to make high-definition displays for computers, TV, and portable electronic apparatus.

Besides making energy efficient, high-definition displays, QD-LEDs have important applications in making solid state white light sources. For a normal LED light source, there are two ways to generate white light. The first way is to carefully mix the green, red and blue light together. In this way, energy is lost due to the internal absorption and the mixing process. The second way is to add phosphor to blue LEDs. The emission wavelength of a blue LED is around 380-420 nm, where the absorption efficiency of conventional phosphors is low. Therefore, high conversion efficiency phosphors are needed for generating white light. Researches have shown that the colloidal synthesized QDs can be good nano-particle phosphors. The advantages of QDs as a phosphors are: (1) QDs have very high quantum yields; (2) the energy of emitted photon can be easy tuned by varying the size of QDs; (3) small dot size indicates that more atoms are at the surface sites and any change of the chemical components of those atoms will affect the emission energy of the dot, thus single size QDs can emit multiple colors. In 2003, a research group in Sandia National Labs successfully made the first white light LED using cadmium sulfide QDs [16]. The drawback of this scheme is that an extra chemical compound needed to be added into the QDs during the growth process, which took several weeks for the entire growth process. Later, a research group in Vanderbilt University successfully made white light QD-LED using CdSe QDs with the right size, which they called magic size QDs [18]. Using no extra chemical elements in the QDs, the production process only takes a couple of hours. The white light QD-LED shows a smoother spectrum with a low energy cost, which has huge potential to replace the normal light bulb.

1.2 Quantum Dot Solar Cell

There has been a global focus to search for new and renewable energy due to the energy shortage and the demand of environmental protection. Solar energy is one of the promising candidates for clean and renewable energy. One can convert the sunlight into energy through solar cells, i.e. photovoltaic devices. One of the current research goals is to design a solar cell with a high conversion efficiency and low fabrication cost. The solar cells currently on the market are second generation thin film solar cells with about 10% power conversion efficiency. The advantage of thin film solar cells is the low fabrication cost. The drawback is the low solar power conversion efficiency. The way the common solar cell works is that if the photon energy is larger than the bandgap E_g, the photon creates an exciton, which is an electron hole pair. Since one photon can only create one exciton, the excess energy of the photon is lost to the dissipation processes, such as lattice vibrations, i.e. the emission of phonons. The upper-limit of the power conversion efficiency of conventional single absorber solar cells is about 30%, which is known as Schokely-Queisser limit [19] .

One way to increase the power conversion efficiency is to avoid the loss of the excess photon energy by creating multiple excitons with one photon. This process is known as impact ionization. In the impact ionization process, if the excess photon energy $\Delta = \hbar\omega - E_g$ is larger than the bandgap, it will excite additional electron-hole pairs. Impact ionization was observed in bulk semiconductors in 1950s. In the bulk semiconductor, impact ionization requires both energy and momentum conservation, which limits the impact ionization efficiency. Furthermore, the phonon induced exciton relaxation process is very fast, which competes with the impact ionization process. It has been found that when the excess photon energy is many times the bandgap, the impact ionization efficiency in bulk silicon is about 5% [20].

It has been demonstrated recently that impact ionization is very efficient in the colloidally synthesized QD systems. Due to the three dimensional confinement, the exciton has discreet energy states, which leads to the suppression of the phonon interaction with the exciton states. The impact ionization rate is enhanced due to quantum confinement. Also, in the zero dimensional system, angular momentum is not a good quantum number. Crystal momentum does not need to be conserved in the impact ionization process. In 2004, R. D. Schaller and V. I. Klimov first demonstrated impact ionization by using PbSe nanocrystals [21]. In the experiment, the optical power of the pump pulse was set to excite at most one exciton when the photon energy $E_g < \hbar\omega < 2E_g$, i.e. to avoid direct multi-exciton generation. The weak probe pulse was tuned to probe the ground state exciton population. If there is only one exciton, the radiative lifetime is about a few ns. It has been shown that the the exciton decay through Auger process is dramatically enhanced in the presence of multiple exciton states [22]. Thus, if there are a few ground state excitons, a fast decay will be observed on the time scale of tens of pico second. After the initial decay, the signal level stays constant due to the long lifetime of a single exciton state. If the background level is defined as B and the initial single amplitude is defined as A, then the number of generated excitons is A/B. In Klimov's work, when the input photon energy is $3.8E_g$, one photon can generate two excitions, which corresponds to a quantum yeild of 218%, where quantum yield is defined as the number of ground state excitons generated by a photon.

Following Klimov's work, progress has been made to improve the quantum yield of the impact ionization process. A quantum yield value of 300% was achieved with a photon energy of $4E_g$ exciting PbSe QDs [23]. The difference in Ellingson *et al.*'s work is that the diameter of QDs is 3.9 nm. In this work, they also show that quantum yield has a strong dependence on the QD size. Later, Klimov's group improved the quantum yields to a value of 700% with a photon energy of $7.8E_g$, which means one photon generates 7 excitons. A quantum yield value of 700% corresponds an energy conversion efficiency of 65% with a 0.3 eV bandgap [24]. This is about a 100% increase compared to the Schokely-Queisser limit. QD based photovoltaic devices are very promising as the third generation of solar cells.

1.3 Quantum Dot Quantum Computing

No one who grew up in the technology age can imagine what the life would be like without computers. Since the first computer was built in the early 1940s, its size has shrunk from the huge monoliths to the present day portable and powerful personal computers. The key for this great development is the highly integrated electronic circuit, i.e. many transistors can be built onto a small semiconductor chip. The speed of the central processing unit (CPU) has been increasing exponentially according to Moore's law over the past few decades. However, as of the end of the last century, the development of the CPU's speed has deviated from what Moore has expected because the size of the transistors has reached the nanometer scale, on which quantum mechanical effects show up and the classical theory is no longer applicable. Quantum computation and quantum information theory were born as a result of this situation and have drawn a lot of attentions for the past few years.

In a classical computer, the basic computation and information storage unit is the binary bit represented by either 0 or 1. As we know, in quantum mechanics, any state can be represented by a coherent supposition of the eigenstates. If 0 and 1 are chosen to be the computation basis, then a quantum bit (qubit) can be written as $\alpha|0\rangle + \beta|1\rangle$, where $|\alpha|^2 + |\beta|^2 = 1$. Thus, in the classical computation, n classical bits can only represent 1 possible state out of 2^n possible states. On the other hand, n qubits can represent all 2^n states. The quantum superposition is one of the reasons why quantum computation is more powerful than classical computation. Based on the quantum mechanical features of the qubits, such as quantum entanglement between the qubits and quantum superpositions, a few problems intractable to the classical computation can be easily solved by quantum algorithms using a quantum computer. A famous example is Shor's algorithm [25], which can factor a big integer with ease by a quantum computer. Currently, public-key cryptography is based on the assumption that it is infeasible to factor a big integer number by classical computations. This approach was first proposed by Ron Rivest, Adi Shamir, and Leonard Adleman and is known as the RSA scheme. By using Shor's algorithm, an integer N can be factored by using polynomial time in $O(LogN)$, which is much shorter than $O(2^{LogN^{1/3}})$ of the classical computation. Shor's discovery puts current cryptography schemes in danger if quantum computers are eventually successfully made.

Many schemes have been proposed for quantum computing devices. Ion trap systems are a great example of the atomic systems [26]. The entanglement of the ion-qubits located in remote ion-traps has been demonstrated recently [27]. The solid state approaches towards the quantum computations include superconducting Josephson tunnelling junctions [28], nitrogen vacancy centers in diamonds [29], and solid state semiconductor QD system [30]. Since QDs behave like atoms in many ways, the well developed experimental techniques for atomic systems can be applied to the QD systems. QD systems are also solid state based and close to our current computer hardware. The well-developed semiconductor fabrication technology provides strong support for engineering such advanced quantum devices.

DiVincenzo proposed five requirements for the implementation of quantum computations [7]. In the following, the five requirements are discussed with respect to the quantum dot system.

1. *A scalable physical system with well characterized qubits.* In the QD system, a qubit can be represented by a few means. In a neutral QD, the ground state and excited state of an exciton can form a qubit. In a charged QD, the spin degree of freedom can form a two-level system, either spin up or spin down, which can represent a qubit. In an electrostatically confined double QD, a logical quit can be formed by a spin singlet state and a spin triplet state. The ability to manipulate one qubit a time, i.e. one QD a time is already demonstrated in many experiments. In the near future, the focus will be on the manipulation of coupled qubits in double QDs, which is an important step towards scalable quantum computation. In principle, scalability can be achieved by fabricating patterned QD arrays.

2. *The ability to initialize qubit states.* For any computation, we need to prepare the system to a known state before operations. In order to satisfy fault tolerant quantum computation, we have to continuously supply initial qubit states for computation and gate operations. In the quantum dot system, fast qubit initialization can be realized by optical pumping, which is going to be discussed in Chapter 5.

3. *Long relevant decoherence time, much longer than gate operation time.* In order to realize fault tolerant quantum computation, the qubit has to be operated on 10^4

times before it loses coherence. Thus, the qubit must have long relevant coherence times compared to the gate operation time. Due to three dimensional confinement, an electron spin trapped inside a quantum dot is immune to the environment. It has been experimentally demonstrated that the electron spin coherence time is on the order of μs [5, 6]. Considering the ultrafast optical operatons on the order of ps, the spin qubit can be operated at least on 10^6 times before decoherence happens, which satisfies element 3.

4. *A universal set of quantum gates.* It has been shown that any quantum operation can be constructed by a control-not gate (cnot) with a single qubit rotation gate [34]. A cnot gate is formed by two qubits. In the quantum dot system, a cnot gate has been demonstrated in the bi-exciton system [35], however, this scheme is not scalable. Scalable quantum gates can be realized by using electron spins in coupled quantum dots [36]. A single qubit rotation can be demonstrated by using the Rabi oscillation technique. An arbitrary single exciton qubit rotation has been demonstrated in our lab [37].

5. *A qubit-specific measurement capability.* In the ideal case, we would like to do cyclic non-demolition measurements. In this case, the read out efficiency is high and the quantum state will not be disturbed after read out. This is the read out process used in ion-trap systems. However, it is not trivial to find a cyclic transition in QD system. Recently, a scheme for the cyclic read out has been demonstrated experimentally by using a double-QDs system [38], which is a big step towards optical-driven quantum computation.

1.4 Thesis chapter outlines

In Chapter 2, the sample structure and experimental techniques are going to be introduced. The basic idea of excitons, trions, and the selection rules of a trion state in the presence of heavy-light hole mixing are discussed. In Chapter 3, the Autler-Townes Splitting and the optical Mollow absorption spectrum are demonstrated in a single neutral QD. In Chapter 4, the optical Mollow absorption spectrum is demonstrated in a single charged QD, which shows the two level atomic feature of the charged QD system even under a strong optical field. Fast electron spin state initialization by using an optical pumping technique is realized in Chapter 5. In Chapter 6, the coherence of the spin ground states of an electron is generated by the means of coherent population trapping in a single charged QD. Based on the coherent population trapping technique developed in Chapter 6, the dynamic nuclear spin polarization is investigated in Chapter 7, where a hole spin assisted nuclei spin self-focusing effect is observed. This self-focusing effect leads to the suppression of nuclear spin fluctuations. Chapter 8 will summarize this thesis work and look into the future directions.

References

[1] D.Gammon, D. G. Steel, Physics Today **55**, 36 (2002).

[2] N. Peyghambarian, S. W. Koch, A. Mysyrowicz, Introduction to Semiconductor Opitcs, Prentice-Hall Inc. (1993)

[3] L. Van Hove, Phys. Rev. **89**, 1189C1193 (1953).

[4] H. Drexler, D. Leonard, W. Hansen, J.H. Kotthaus, P. M. Petroff, Phys. Rev. Lett. **73**, 2252 (1994).

[5] R. J. Warburton *et al.*, Nature **405**, 926 (2000).

[6] C. B. Murray, D. J. Noms, and M. G. Bawendi, J. Am. Chem. Soc. **115**, 8706(1993).

[7] L. R. Kouwenhoven *et al.*, in the proceedings of the Advanced Study Institute on Mesoscopic Electron Transport, edited by L.L. Sohn, L.P. Kouwenhoven, G. Schon (1997).

[8] D. Leonard, M. Krishnamurthy, C. M. Reaves, S. P. DenBaars, P. Petroff, Appl. Phys. Lett. **63**, 3203 (1993)

[9] A. Zrenner, L. V. Butov, M. Hagn, G. Abstreiter, G. Bohm, and G. Weimann, Phys. Rev. Lett. **72**, 3382 (1994).

[10] J. R. Guest *et al.*, Phys. Rev. B. **65**, 241310(R) (2002).

[11] Xiaodong Xu *et al.*, Science **317**, 929 (2007).

[12] V. M. Axt, A. Stahl, Z. Phys. B **93**, 195 (1994).

[13] N. H. Bonadeo *et al.*, Phys. Rev. Lett. **81**, 2759 (1998).

[14] A. Muller *et al.*, Phys. Rev. Lett. **99**, 187402 (2007).

[15] A. H. Mueller *et al.*, Nano Lett. **5**, 1039(2005)

[16] L. E. S. Rohwer, B. L. Abrams, J. P. Wilcoxon, and S. G. Thoma, Proc. SPIE, Vol. **5366**, 66 (2004);

[17] Seth Coe, Wing-Keung Woo, Moungi Bawendi, Vladimir Bulovic, Nature **420**, 800 (2002).

[18] Michael J. Bowers II, James R. McBride, and Sandra J. Rosenthal, J. AM. CHEM. SOC. **127**, 15378 (2005)

[19] W. Shockley, H. J. Queisser, J. Appl. Phys. **32**, 510(1961).

[20] O. J. Christensen, Appl. Phys. **47**, 690(1976).

[21] R. D. Schaller and V. I. Klimov, Phys. Rev. Lett. **92**, 186601(2004).

[22] V. I. Klimov, A. A. Mikhailovsky, D. W. McBranch, C. A. Leatherdale, M. G. Bawendi, Science **287**, 1011(2000).

[23] Randy J. Ellingson *et al.*, Nano Lett. **5**, 865(2005).

[24] Richard D. Schaller, Milan Sykora, Jeffrey M. Pietryga, and Victor I. Klimov, Nano Lett. **6**, 424(2006)

[25] P.W. Shor, in Proceedings of the 35th Annual Symposium on the Foundations of Computer Science 124C 133 (IEEE Computer Society Press, Los Alamitos, California, 1994).

[26] Cirac, J. I. and Zoller, P. Phys. Rev. Lett. **74**, 4091 (1995).

[27] D. L. Moehring *et al.* Nature **449**, 68 (2007)

[28] D. Vion et al.. Manipulating the quantum state of an electrical circuit. Science 296, 886 (2002).

[29] David D. Awschalom, Ryan Epstein and Ronald Hanson, Scientific American, 89(October, 2007).

[30] D. Loss, D. P. DiVincenzo, Physical Review A **57**, 120 (1998).

[31] D. P. DiVincenzo, Fortschr. Phys. **48**, 771 (2000).

[32] J.R. Petta et al., Science **309**, 2180 (2005).

[33] A. Greilich et al., Science **317**, 1896 (2007).

[34] M. Nielsen and I. Chuang, Quantum Computation and Quantum Information, Cambridge University Press, 2000

[35] Xiaoqin Li *et al.*, Science **301**, 809 (2003).

[36] C. Piermarocchi, Pochung Chen, L. J. Sham, and D. G. Steel , Phys. Rev. Lett. **89**, 167402 (2002).

[37] Yanwen Wu, Xiaoqin Li, L. M. Duan, D. G. Steel, and D. Gammon, Phys. Rev. Lett. **96**, 087402 (2006).

[38] D. Kim *et al.* To be published

CHAPTER 2

Samples, Experimental Techniques and Theoretical Background

The first generation of quantum dots (QDs) investigated in our lab was the GaAs interface fluctuation QDs (IFQD) [1,2]. This type of QD is formed at the interface of lattice matched heterostructures during growth interruptions. The critical feature of IFQDs is that they have large dipole moments. Optical absorption measurement in our lab has yielded a dipole moment of around 100 Debye [28]. The large dipole moment indicates a strong interaction between laser light and the quantum dot, which lead to many fantastic achievements, such as Rabi oscillations [4,10,11], controlled exciton qbuit rotation gate [7], arbitrary rotations of an exciton qubit [8], and optical generation and control of electron spin coherence [10,24]. Despite all of these wonderful achievements, there is a major drawback of the IFQD system, which is the dot's weak lateral confinement. The lack of strong lateral confinement deteriorates the atomic properties of the IFQD.

In this thesis, another type of QDs, self assembled QDs (SAQDs) [11,12], are used. Since SAQDs are formed at the interface of two lattice mismatched semiconductor systems, the lateral confinement is provided by the strain, which is much stronger than the lateral confinement of IFQD. Therefore, SAQDs have very good optical qualities and behave like isolated atomic systems in many cases [1,4,14]. Less favorable characteristics of SAQD include a ground state excitation energy in the near-infrared regime and an optical dipole moment much smaller than that of IFQD. But with the development of laser technology and detection techniques, we are able to perform optical excitation and detection of a single SAQD.

In this chapter, the sample structure is illustrated first. Then the detailed experimental setup and detection techniques will be discussed. Finally, the physical models and some theoretical background will be provided for the neutral and charged exciton systems, which are the focus of this thesis.

2.1 Schottky Diode Sample Structure

The sample under study contains InAs self-assembled quantum dots (SAQDs) grown by molecular beam epitaxy. The QDs are embedded in an n^+ intrinsic Schottky diode structure [1,2,17]. As shown in Fig. A.1(a), the sample layer structure is a 100 nm aluminum thick mask with micron-sized apertures, 5 nm titanium, 10 nm GaAs cap, 40 nm $Al_{0.3}Ga_{0.7}As$, 230 nm GaAs, 2.5 nm InAs QDs layer, 80 nm GaAs, 500 nm GaAs Te-doped ($5 \times 10^7 cm^{-3}$) layer and an electronic contact formed by the GaAs substrate. The dot density is about 1 dot/μm^2. The micron-size apertures provide the spatial resolution to investigate single QDs.

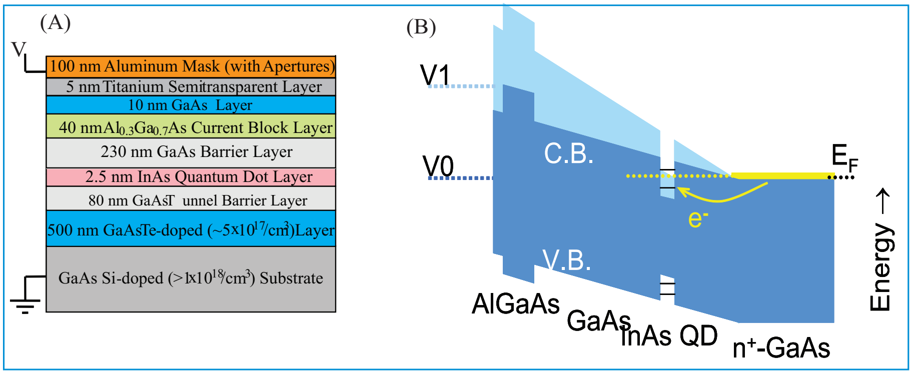

Figure 2.1: Schematics of Sample Structure. (a) The sample layer structure. (b) A schematic showing the relative energy level between the dot and the electron reservoir that can be controlled by the DC bias across the sample.

The ground state emission wavelength of the SAQDs is usually above 1μm, which is beyond the tuning range of common Ti-Saphire lasers and beyond the working range of the silicon detector. Instead of using rapid thermal annealing to blue shift the QD ground state energy [19], an In-flush technique [3,4] is used during the growth process. The As-grown dots are capped with a 2.5 nm layer of GaAs. The growth process is then interrupted and the temperature is raised to remove InAs from the still-exposed portion of the QDs. This produces disk-shaped dots with a transition wavelength shorter than $1\mu m$, so that silicon detectors can be used to detect the signals.

Since the QDs are embedded in a Schottky diode structure, the transition energies can be electrically tuned by the DC Stark effect by varying the DC gate voltage across the sample [5], as shown in Fig. A.1(b). By continuously adjusting the QD potential relative to the Fermi sea level from high to low, the QD can be changed from positively charged state to multi-electron charged state [1, 24]. When the DC Stark shift is modulated by a small square wave modulation voltage, the transmission signal can be detected at the modulation frequency by a phase-sensitive lock-in amplifier. We will discuss this in detail in the next section.

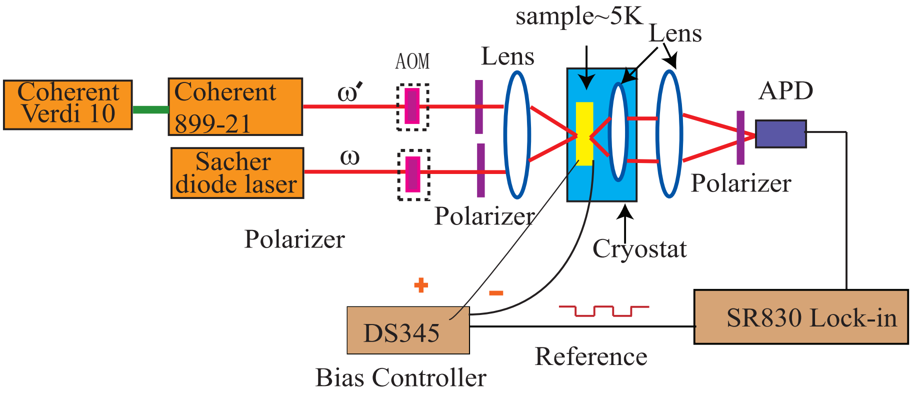

Figure 2.2: Schematics of General Experimental Setup

2.2 Experimental setup and detection techniques

The experimental setup for the experiments in this thesis is shown in Fig. 3.2. Two continuous wave lasers (CW) are in the setup. One is a Coherent 899-21 Ti-Sapphire laser and the other is a Sacher diode laser. The individual linewidths of the lasers are less than 1 MHz. The mutual coherence between the two lasers have been measured to be a few MHz. Depending on the experimental purpose, either one or two lasers is used. The polarizations of the lasers are individually controlled by linear polarizers. The sample is held in a continuous helium-flow superconductor coil magneto-cryostat at a temperature of 5 K. There is a tight focus lens inside the cryostat to increase the signal collection efficiency. The QD signal is detected by a detector outside the cryostat and sent into a lock-in amplifier (model number SR830). The detector used is a silicon avalanche photodiode with peak sensitivity wavelength at 940 nm (model number Hamamatsu S8890-15). In the pump-probe experiment, we set both pump and probe beams to be orthogonally polarized. Hence, we can filter out the pump beam with a polarizer in front of the detector and detect the probe beam only.

When a pump-probe differential transmission (DT) experiment is performed, two acoustic optic modulators are used to chop the laser beams individually and detect the signal at the difference of the chopping frequencies. The DT technique has been well explained in my colleagues' thesis [21, 22] and is not going to be discussed in detail here. Instead, I will focus on the other experimental technique, known as DC Stark shift modulation and used quite often in this thesis.

As discussed in the sample structure section, the QD transition energies can be controlled by varying the DC gate voltage across the sample. On top of the DC voltage, a small square wave modulation voltage is applied with amplitude κ and frequency ω_m, as shown in Fig. 3.3(a). Therefore, the QD transition frequency is also modulated at the frequency ω_m, and the modulation amplitude $\delta\omega$ depends linearly on κ when the linear DC Stark shift dominates, as shown in Fig. 3.3(b). The QD signal also oscillates at this modulation frequency and is demodulated by the lock-in amplifier. The lineshape of the singal can be qualitatively understood from the following. Assuming the lineshape without modulation is Lorentizan, which corresponds to $A\left(\omega, \omega_o\right) = \frac{\alpha\gamma^2}{(\omega-\omega_o)^2+\gamma^2}$, the detected signal for laser frequency ω is $S\left(\omega\right) = A\left(\omega, \omega_o + \delta\omega\right) - A\left(\omega, \omega_o - \delta\omega\right)$. If the modulation amplitude $\delta\omega << \gamma$, we obtain $S\left(\omega\right) = \frac{4\alpha\gamma^2(\omega-\omega_o)\delta\omega}{((\omega-\omega_o)^2+\gamma^2)^2}$, which corresponds to the derivative of a normal Lorentizan lineshape, illustrated in Fig. 3.3(c). We can see that the signal strength also depends linearly on the modulation amplitude $\delta\omega$. When $\delta\omega >> \gamma$, as shown in Fig. 3.3(d), the detected spectra are two Lorentizan lineshapes separated by $2\hbar\delta\omega$,

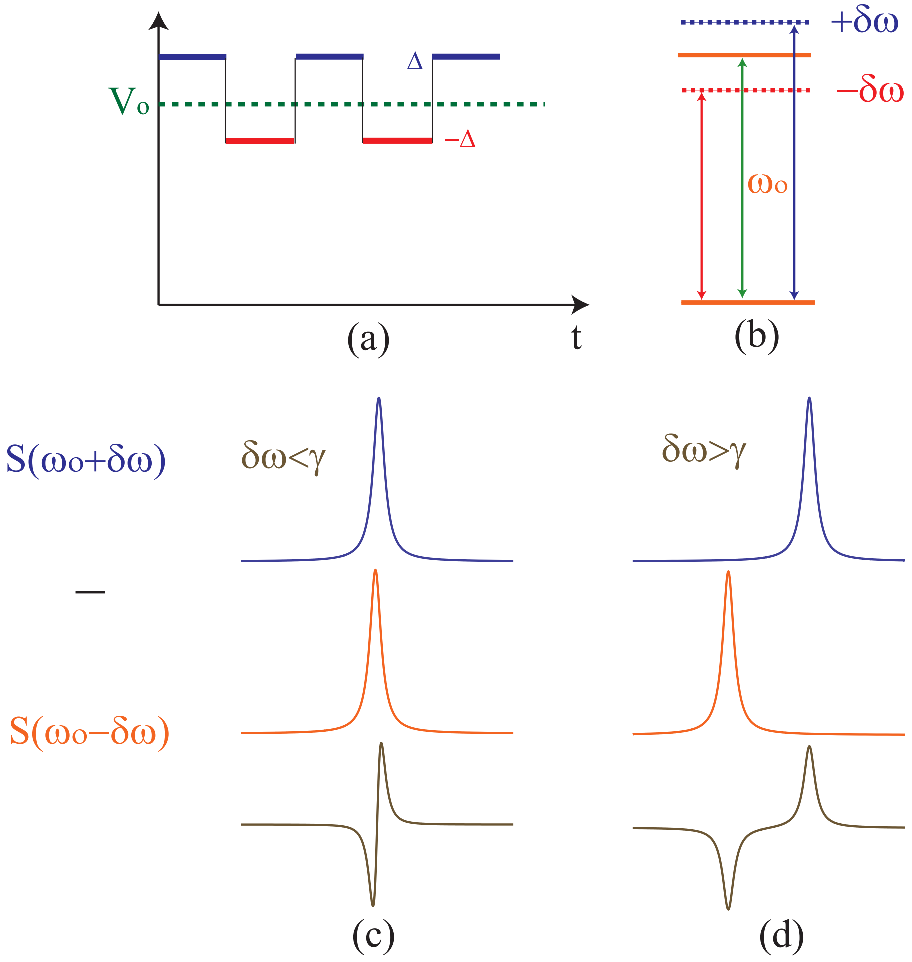

Figure 2.3: Theory of DC Stark Shift Modulation Technique. A series of cartoons show how the DC stark shift modulation works. (a) DC bias across the sample is modulated by a square wave modulation, which leads to (b) the modulation of the atomic transition. The expected lineshape for modulation amplitudes (c) smaller or (d) larger than the transition linewidth.

one of which is absorption and the other is transmission. Therefore, the physical parameters can be extracted directly from the measurements. In our experiment, we use large modulation voltages at a frequency of 1.103 KHz to avoid complexities associated with small modulation amplitude [5].

2.3 Physical models and the polarization selection rules for the QD system

In this section, the physical models with the polarization selection rules will be discussed for the neutral and singly charged exciton systems, where the QD interacting with the external magnetic fields is emphasized.

Depending on the number of electrons in the quantum dots, the QD states have different physical models and have different optical responses. Two types of QD states are studied in this thesis. One is for neutral QDs and the other is for single negatively charged QDs. For a neutral QD, there is no excess electron or hole in the QD. Without the optical excitation, the QD is in the crystal ground state. With the optical excitation, an electron and hole pair is formed, which is known as an exciton, as shown in Fig. 3.4(a). If there is an excess charge in the QD without optical excitation, it is known as a charged QD, as shown in Fig. 3.4(b). A QD charged with exactly one electron is the focus of this thesis.

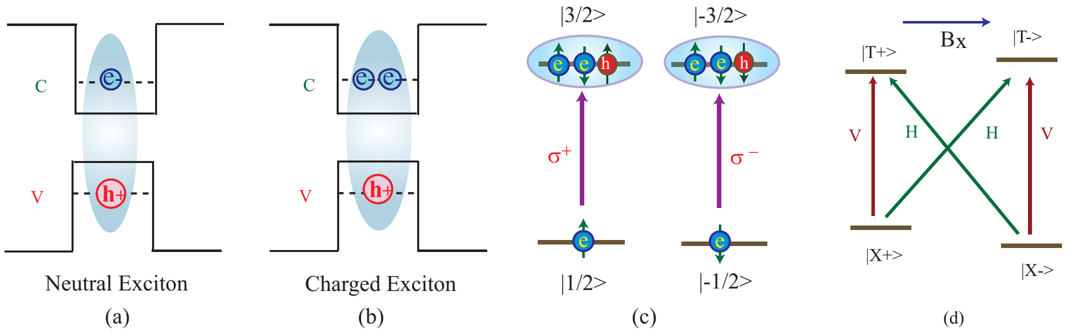

Neutral Exciton
(a)

Charged Exciton
(b)

(c)

(d)

Figure 2.4: Physical Models of Excitons and Trions. (a) Band structure of (a) a neutral exciton and (b) a charged exciton. Energy level diagram of a charged QD (c) without and (d) with a magnetic field.

The hamiltonian of the electron and hole system in the magnetic field is

$$\begin{aligned} H_{Zeeman} &= H_e + H_h \\ H_e &= g_e \mu_B \sum_{i=x,y,z} S_{ei} B_i \\ H_h &= -2\mu_B \sum_{i=x,y,z} (kJ_{h,i} + qJ_{h,i}^3) B_i \end{aligned}$$

, where H_e is the electron Hamiltonian and H_h is the hole Hamiltonian, g_e, k and q are the Luttinger Zeeman splitting constants [25–27]. In the QD system, if the lateral confinement is much weaker than the vertical confinement, the heavy-light hole mixing can be ignored. Since the energy separation between the heavy hole and light hole is much larger than the the Zeeman splitting due to the strong spin-orbital coupling, the light hole can be ignored. The sublevels of the heavy hole can be represented by an effective spin $\widetilde{S_h} = \frac{1}{2}$, where $J_h = \frac{3}{2}(-\frac{3}{2})$ corresponds to $\widetilde{S_h} = \frac{1}{2}(-\frac{1}{2})$. The Zeeman term can be written as

$$H_{Zeeman} = g_e \mu_B \sum_{i=x,y,z} S_{ei} B_i - g_h \mu_B \sum_{i=x,y,z} \widetilde{S_{hi}} B_i. \tag{2.1}$$

Fig. 3.4(c) shows the energy level diagram of a single negatively charged exciton at zero magnetic field. Without optical excitation, the electron is in the ground state with two fold degeneracy, either spin up $\left|\frac{1}{2}\right\rangle$ or spin down $\left|-\frac{1}{2}\right\rangle$. Under optical excitation, the two electrons form a spin singlet state. So the angular momentum of the trion state is determined by the hole spin, either $\left|\frac{3}{2}\right\rangle$ or $\left|-\frac{3}{2}\right\rangle$. The two trions are also energetically degenerate. After the magnetic field is turned on, the degeneracy of both spin ground states and the trion states are lifted. There are two configurations depending on the applied magnetic field direction.

2.3.1 Magnetic Field Applied in the Faraday Geometry

The magnetic field is applied along the sample growth direction (Z axis), *i.e.* only B_z is non-zero, which is known as the Faraday geometry. By taking the inner product of the hamiltonian described by Equ. 2.1 in the basis of $|\pm 1/2\rangle, |\pm 3/2\rangle$, the Zeeman energy term is

$$H_{Zeeman,f}=\frac{\mu_B B_z}{2}\begin{array}{c|cccc} & \left|\frac{1}{2}\right\rangle & \left|-\frac{1}{2}\right\rangle & \left|\frac{3}{2}\right\rangle & \left|-\frac{3}{2}\right\rangle \\ \hline \left\langle\frac{1}{2}\right| & g_{e,z} & 0 & 0 & 0 \\ \left\langle-\frac{1}{2}\right| & 0 & -g_{e,z} & 0 & 0 \\ \left\langle\frac{3}{2}\right| & 0 & 0 & -g_{h,z} & 0 \\ \left\langle-\frac{3}{2}\right| & 0 & 0 & 0 & g_{h,z} \end{array}$$

The Hamiltonian without the interaction of the magnectic field is

$$H_0=\begin{array}{c|cccc} & \left|\frac{1}{2}\right\rangle & \left|-\frac{1}{2}\right\rangle & \left|\frac{3}{2}\right\rangle & \left|-\frac{3}{2}\right\rangle \\ \hline \left\langle\frac{1}{2}\right| & 0 & 0 & 0 & 0 \\ \left\langle-\frac{1}{2}\right| & 0 & 0 & 0 & 0 \\ \left\langle\frac{3}{2}\right| & 0 & 0 & \omega_0 & 0 \\ \left\langle-\frac{3}{2}\right| & 0 & 0 & 0 & \omega_0 \end{array}$$

There are only two optically allowed transitions from the spin ground states to the trion states. These are $\left|\frac{1}{2}\right\rangle \overset{\sigma+}{\rightarrow} \left|\frac{3}{2}\right\rangle$, with a corresponding transition energy $\hbar\omega_0 - \frac{\mu_B B_z}{2}(g_{e,z}+g_{h,z})$, and $\left|-\frac{1}{2}\right\rangle \overset{\sigma-}{\rightarrow} \left|-\frac{3}{2}\right\rangle$, with a corresponding transition energy $\hbar\omega_0 + \frac{\mu_B B_z}{2}(g_{e,z}+g_{h,z})$.

2.3.2 Magnetic Field Applied in the Voigt Geometry

The magnetic field lies in the XY plane perpendicular to the Z axis, which can be represented by $\overrightarrow{B} = (B\cos(\theta), B\sin(\theta), 0)$. By taking the dot product of the Eqn. 2.1, we get the Hamiltonian

$$H_{Zeeman,V}=\begin{array}{c|cccc} & \left|\frac{1}{2}\right\rangle & \left|-\frac{1}{2}\right\rangle & \left|\frac{3}{2}\right\rangle & \left|-\frac{3}{2}\right\rangle \\ \hline \left\langle\frac{1}{2}\right| & 0 & \frac{g_{e,x}\mu_B B\cos(\theta)}{2} & 0 & 0 \\ \left\langle-\frac{1}{2}\right| & \frac{g_{e,x}\mu_B B\cos(\theta)}{2} & 0 & 0 & 0 \\ \left\langle\frac{3}{2}\right| & 0 & 0 & 0 & -\frac{g_{h,x}\mu_B B\cos(\theta)}{2} \\ \left\langle-\frac{3}{2}\right| & 0 & 0 & -\frac{g_{h,x}\mu_B B\cos(\theta)}{2} & 0 \end{array} \tag{2.2}$$

$$H_{Zeeman,y}= \begin{array}{c} \\ \left\langle\frac{1}{2}\right| \\ \left\langle-\frac{1}{2}\right| \\ \left\langle\frac{3}{2}\right| \\ \left\langle-\frac{3}{2}\right| \end{array} \begin{array}{c} \begin{array}{cccc} \left|\frac{1}{2}\right\rangle & \left|-\frac{1}{2}\right\rangle & \left|\frac{3}{2}\right\rangle & \left|-\frac{3}{2}\right\rangle \end{array} \\ \begin{pmatrix} 0 & -i\frac{g_{e,y}\mu_B B\sin(\theta)}{2} & 0 & 0 \\ i\frac{g_{e,y}\mu_B B\sin(\theta)}{2} & 0 & 0 & 0 \\ 0 & 0 & 0 & i\frac{g_{h,y}\mu_B B\sin(\theta)}{2} \\ 0 & 0 & -i\frac{g_{h,y}\mu_B B\sin(\theta)}{2} & 0 \end{pmatrix} \end{array} \tag{2.3}$$

So the total Hamiltonian of the spin field interaction is $H_{Zeeman,x} + H_{Zeeman,y}$. For example, if $\theta = 0$, i.e. the field is along the x direction, then the eigen states and the respective eigen energies are

$$\begin{bmatrix} Eigenenergy & -\frac{g_{e,x}\mu_B B}{2} & \frac{g_{e,x}\mu_B B}{2} & -\frac{g_{h,x}\mu_B B}{2} & \frac{g_{h,x}\mu_B B}{2} \\ Eigenstates & \{-1,1,0,0\} & \{1,1,0,0\} & \{0,0,1,1\} & \{0,0,-1,1\} \end{bmatrix} \tag{2.4}$$

If $\theta = \frac{\pi}{2}$, i.e. the field is along the y direction, then the eigen states and eigen energies are

$$\begin{bmatrix} Eigenenergy & -\frac{g_{e,y}\mu_B B}{2} & \frac{g_{e,y}\mu_B B}{2} & -\frac{g_{h,y}\mu_B B}{2} & \frac{g_{h,y}\mu_B B}{2} \\ Eigenstates & \{i,1,0,0\} & \{-i,1,0,0\} & \{0,0,-i,1\} & \{0,0,i,1\} \end{bmatrix} \tag{2.5}$$

The corresponding selection rules can be derived from the above eigenstates. Figure 3.4(d) displays the trion energy level diagram with the applied magnetic field in the $\overrightarrow{X}$ direction. The outer pair of transitions are vertically polarized and the inner pair of transitions are horizontally polarized.

2.4 The heavy and light hole mixing effect

In the previous section, we ignored the heavy and light hole mixing (HLHM) due to the large spin-orbit coupling. This is legitimate for weakly confined QD systems. For SAQDs, the large lateral strain along with the in-plane anisotropy will induce a heavy and light hole mixing [10–13]. The trion state is formed by two electrons and one hole. Since the two electrons form a spin singlet pair, the net spin property of the trion is determined by the hole spin. Therefore, the charged QD is a good system to monitor the physical properties of the hole spin. In the following, the selection rules for the charged QD with a hole mixing effect are going to be discussed.

2.4.1 Zero Magnetic Field

Without the HLHM, there are only two optically allowed transitions for a singly charged QD, which are

$$|1/2\rangle \underset{\longrightarrow}{\sigma^+} |+3/2\rangle \; and \; |-1/2\rangle \underset{\longrightarrow}{\sigma^-} |-3/2\rangle \tag{2.6}$$

In the presence of the HLHM, the trion states can be written as

$$|\psi_t^{\pm}\rangle = |\pm 3/2\rangle - \beta_{\pm}|\mp 1/2\rangle \tag{2.7}$$

where, $\beta_{\pm} = \beta e^{\pm i2\theta}$, represents the hole mixing strength, and θ is the direction of the polarization axis [10, 13]. The electron spin ground states can be excited to the light hole states by

$$|1/2\rangle \underset{\longrightarrow}{\sigma^-} |-1/2\rangle \; and \; |-1/2\rangle \underset{\longrightarrow}{\sigma^+} |1/2\rangle \tag{2.8}$$

Thus, with the HLHM effect, either of the spin ground states $|1/2\rangle$ and $-|1/2\rangle$ can couple to the trion state with both σ^+ and σ^- polarizations. The selection rules become elliptically polarized. The degree of polarization can be denoted by ρ_p, where

$$\rho_p = \frac{2\beta^{3/2}}{1+\beta^{5/2}} \tag{2.9}$$

ρ_p can be determined by polarization dependent photoluminescence spectroscopy [10] and absorption spectroscopy (see Chapter 5). From Equation 2.9, the mixing strength β can be inferred.

2.4.2 Hole Mixing Effect in The Presence of an External Magnetic Field

In the above section, it was shown that the HLHM affects the selection rules. This section shows how the HLHM affects the selection rules in the presence of the magnetic field. This is important because the selection rules are critical for the design of the experimental schemes.

When the magnetic field is applied in the $\overrightarrow{X}$ direction, the energy level diagram associated with the selection rules is shown in Fig. 3.4(d) in the absence of the HLHM. With the HLHM mixing, the trion states are

$$|T\pm\rangle = \frac{1}{\sqrt{2}}(\pm e^{-i\theta}|\psi_t^+\rangle + e^{i\theta}|\psi_t^-\rangle) \tag{2.10}$$

where $|\psi\pm\rangle$ is the same as in Eqn 2.7. The spin ground states are

$$|X\pm\rangle = \frac{\pm|1/2\rangle + |-1/2\rangle}{\sqrt{2}} \tag{2.11}$$

The unit vectors for the circularly polarized light are

$$\widehat{\varepsilon}^{\pm} = \mp\frac{\widehat{\epsilon}_x \pm i\widehat{\epsilon}_y}{\sqrt{2}} \tag{2.12}$$

The electric field can be represented as

$$\overrightarrow{E} = E_x\widehat{\epsilon}_x + E_y\widehat{\epsilon}_y \tag{2.13}$$

Inserting Eqn 2.12 into the above equation, we get

$$\overrightarrow{E} = -E_{-1}\widehat{\epsilon}^{+} - E_{+1}\widehat{\epsilon}_{-} \tag{2.14}$$

where

$$E_{\mp 1} = -\frac{\mp E_x + iE_y}{\sqrt{2}} \tag{2.15}$$

This is similar to the dipole operator

$$\overrightarrow{r} = -r_{-1}\widehat{\epsilon}^{+} - r_{+1}\widehat{\epsilon}^{-} \tag{2.16}$$

and

$$\overrightarrow{r}.\overrightarrow{E} = r_{-1}E_{+1} - r_{+1}E_{-1} \tag{2.17}$$

The transition elements can be calculated using the dot product from Eqn 2.17 in the basis $|\psi_t^{\pm}\rangle, |X\pm\rangle$. The results are

$$\langle\psi_t^{+}|\overrightarrow{r}.\overrightarrow{E}|X+\rangle = (-E_{-1} + \beta_{+}E_{+1}) \tag{2.18}$$

$$\langle\psi_t^{+}|\overrightarrow{r}.\overrightarrow{E}|X-\rangle = (E_{-1} - \beta_{+}E_{+1}) \tag{2.19}$$

$$\langle\psi_t^{-}|\overrightarrow{r}.\overrightarrow{E}|X-\rangle = (-E_{+1} + \beta_{-}E_{-1}) \tag{2.20}$$

$$\langle\psi_t^{-}|\overrightarrow{r}.\overrightarrow{E}|X+\rangle = (-E_{+1} + \beta_{-}E_{-1}) \tag{2.21}$$

By using the above results, we get

$$\langle T+|\overrightarrow{r}.\overrightarrow{E}|X+\rangle = \langle T-|\overrightarrow{r}.\overrightarrow{E}|X-\rangle = e^{-i\theta}(-E_{-1} + \beta_{+}E_{+1}) + e^{i\theta}(-E_{+1} + \beta_{-}E_{-1}) \tag{2.22}$$

$$\langle T+|\overrightarrow{r}.\overrightarrow{E}|X-\rangle = \langle T-|\overrightarrow{r}.\overrightarrow{E}|X+\rangle = e^{-i\theta}(E_{-1}-\beta_{+}E_{+1})+e^{i\theta}(-E_{+1}+\beta_{-}E_{-1}) \quad (2.23)$$

If there is no HLHM, i.e. $\theta = 0$ and $\beta = 0$, Equ. 1.22 and Equ. 2.23 are simplified to $E_{-1} + E_{+1} = iE_y$ and $E_{-1} - E_{+1} = E_x$, respectively, which agree with what we have in Fig. 3.4(e). In the presence of the HLHM, the trion four level model is still valid. The only effect induced by the HLHM is that the polarization axis rotates away from the $\overrightarrow{X}$ axis with an angle θ. The outer pair and inner pair transitions are still linearly polarized and orthogonal to each other. Therefore, in the theoretical designs for the charged QD experiment with the magnetic field on, the HLHM effect can be ignored. The experimental demonstration of the HLHM and the selection rules of a charged QD will be discussed in Chapter 5.

2.4.3 Chapter 2 Summary

In this chapter, the detailed sample structure and the general experimental setup were presented. The physical models of the neutral and charged QDs were also shown. The interaction of a charged QD with the external magnetic field was studied, which yielded the 4 level energy level structure of the trion state. The selection rules were also investigated with and without the presence of the HLHM.

References

[1] A. Zrenner, L. V. Butov, M. Hagn, G. Abstreiter, G. Bohm, and G. Weimann, Phys. Rev. Lett. **72**, 3382 (1994).

[2] D. Gammon, E. S. Snow, B. V. Shanabrook, D. S. Katzer, and D. Park, Phys. Rev. Lett. **76**, 3005 (1996).

[3] J. R. Guest *et al.*, Phys. Rev. B. **65**, 241310(R) (2002).

[4] T. H. Stievater*et al.*, Phys. Rev. Lett. **87**, 133603 (2001).

[5] H. Htoon *et al.*, Phys. Rev. Lett **88**, 087401 (2002).

[6] A. Zrenner *et al.*, Nature **418**, 612 (2002).

[7] Xiaoqin Li *et al.*, Science **301**, 809 (2003).

[8] Yanwen Wu, Xiaoqin Li, L. M. Duan, D. G. Steel, and D. Gammon, Phys. Rev. Lett. **96**, 087402 (2006).

[9] M. V. Dutt *et al.*, Phys. Rev. Lett. **94**, 227403 (2005).

[10] J. Berezovsky, M. H. Mikkelsen, N. G. Stoltz, L. A. Coldren, D. D. Awschalom, Science **320**,349 (2008)

[11] D. Leonard, M. Krishnamurthy, C. M. Reaves, S.P. DenBaars, P. Petroff, Appl. Phys. Lett. textbf63, 3203 (1993)

[12] J. Y. Marzin *et al.* Phys. Rev. Lett. 73, 716 (1994)

[13] R. J. Warburton *et al.*, Nature **405**, 926 (2000).

[14] Xiaodong Xu *et al.*, Science **317**, 929 (2007).

[15] A. Muller *et al.*, Phys. Rev. Lett. **99**, 187402 (2007).

[16] M. E. Ware *et al.*, Phys. Rev. Lett. **95**, 177403 (2005).

[17] H. Drexler, D. Leonard, W. Hansen, J. P. Kotthaus, and P. M. Petroff, Phys. Rev. Lett. **73**, 2252 (1994).

[18] J. M. Garcia *et al.*, Appl. Phys. Lett. **71**, 2014 (1997).

[19] Surama Malik, Christine Roberts, Ray Murray, Malcolm Pate, Appl. Phys. Lett. **71**, 1987 (1997);

[20] Z. R. Wasilewski, S. Fafard, J. P. McCaffrey, J. Cryst. Growth **201**, 1131 (1999).

[21] N. H. Bonadeo, Ph.D. thesis.

[22] G. Chen, Ph.D. thesis.

[23] Benito Alen *et al.*, Appl. Phys. Lett. **83**, 2235 (2003).

[24] M. Ediger et al., Phys. Rev. Lett. **98**, 036808 (2007).

[25] H.W. Van Kesteren et al, PRB 41 5283 (1990);

[26] M.J. Snelling et al, PRB 45 3922 (1992);

[27] M. Bayer et al, PRB 65 195315 (2002).

[28] A. V. Koudinov *et al.*, Phys. Rev. B **70**, 241305(R) (2004).

[29] E. L. Ivchenko and A. Yu. Kaminski, U. Rossler, Phys. Rev. B. **54**, 5852 (1996).

[30] D.N. Krizhanovskii et al, Phys. Rev. B 72, 161312 (2005)

[31] Y. Leger, L. Besombes, L. Maingault and H. Mariette, Phys. Rev. B 76, 045331 (2007).

CHAPTER 3

Coherent Optical Spectroscopy of a Single Neutral Exciton

3.1 The Optical Characterization of a Neutral Quantum Dot

The first step in characterization is to locate an exciton state. Self-assembled QDs have a large inhomogeneous broadening. The ground state exciton emission wavelength can vary from 920 nm to 1 μm, therefore, it is not efficient to perform CW absorption spectroscopy to look for the resonant excitation. Instead, we use Photoluminescence (PL) technique to perform a rough characterization at first. In the PL experiment, we use a HR-640 spectrometer with 600 l/mm grove density grating inside. The detector is nitrogen cooled CCD (Princeton instrument 1024). We use a laser to excite the sample above the wetting layer (860 nm for this sample) and detect the QD emission in the 925 to 955 nm window, which is the best working region for our Ti-Saphire laser in the near infrared regime. We map out the bias dependent PL intensity map as shown in Fig A.1(a) [1, 1]. The horizontal axis is the applied bias and the vertical axis is the emission energy. The discrete lines represent QD states. We can see that different states exist at different bias regime. The white oval highlights the exciton state we use to study in this Chapter. Figure A.1(b) shows an example of PL spectrum of the QD at a bias of -0.2 V. The green arrow points to the exciton state of interest. We notice that there is a huge background count which is possibly from the emission tail of the continuum. From the PL, we can estimate the linewidth of the exciton state to be roughly 30 μeV, which is limited by the resolution of the spectrometer and not an intrinsic linewidth of the exciton state.

After we found the target state, we measure the absorption of the state by a DC Stark shift modulation technique using large modulation (see Chapter 2). we fix the laser roughly where the emission energy is and scan the bias voltage to tune the QD transition through the resonance by DC Stark effect, which is equivalent to scanning the laser [3]. We can characterize the coefficient of the DC Stark effect by examining the peak position in the voltage spectrum corresponding for different excitation wavelengths. Figure A.1(c) illustrates such an examination. The horizontal axis is the peak position in the bias spectrum and the vertical axis is the laser excitation energy. The linear line fits the data very well, which indicates that the linear DC Stark effect dominates. We extract the Stark effect coefficient of 0.253 μeV/mv for the current setup. Thus, we can get the real physical information from the bias scanning spectrum by using the characterized DC Stark effect coefficient.

In order to demonstrate that this is a neutral exciton state, we perform polarization characterizations. It is known that due to the in plane anisotropy, the neutral exciton has two linearly polarized states [4], i.e. one is horizontally polarized and the other is vertically polarized. The top four curves in Fig. A.1(d) show the absorption spectra with different polarization excitation, where LCP, RCP, HP and VP represent left circular polarization, right circular polarization, horizontal polarization and vertical polarization, respectively. We can see that the HP (VP) polarized light only excites the corresponding polarized exciton states. Therefore, this is a neutral exciton state. The top two curves are excited with circular polarized light. Since circular polarized light is a linear combination of vertical and horizontal polarization, we observe both polarized exciton states. The light blue curve on top of the LCP data is a Lorentizan fitting, which yields a natural linewidth of 1.8 μeV (or 440 MHz). The fine structure splitting between the two polarized exciton states is about 15 μeV.

CW nonlinear differential transmission (DT) measurement has previously been performed on the interface fluctuation QD (IFQD) [5–7]. However, it has not been demonstrated in a single InAs SAQD due to the small signal to noise ratio. Besides the direct absorption data, here we are able to get nonlinear DT signal from this neutral exciton state. The data is shown in the bottom dark green curve of Fig.

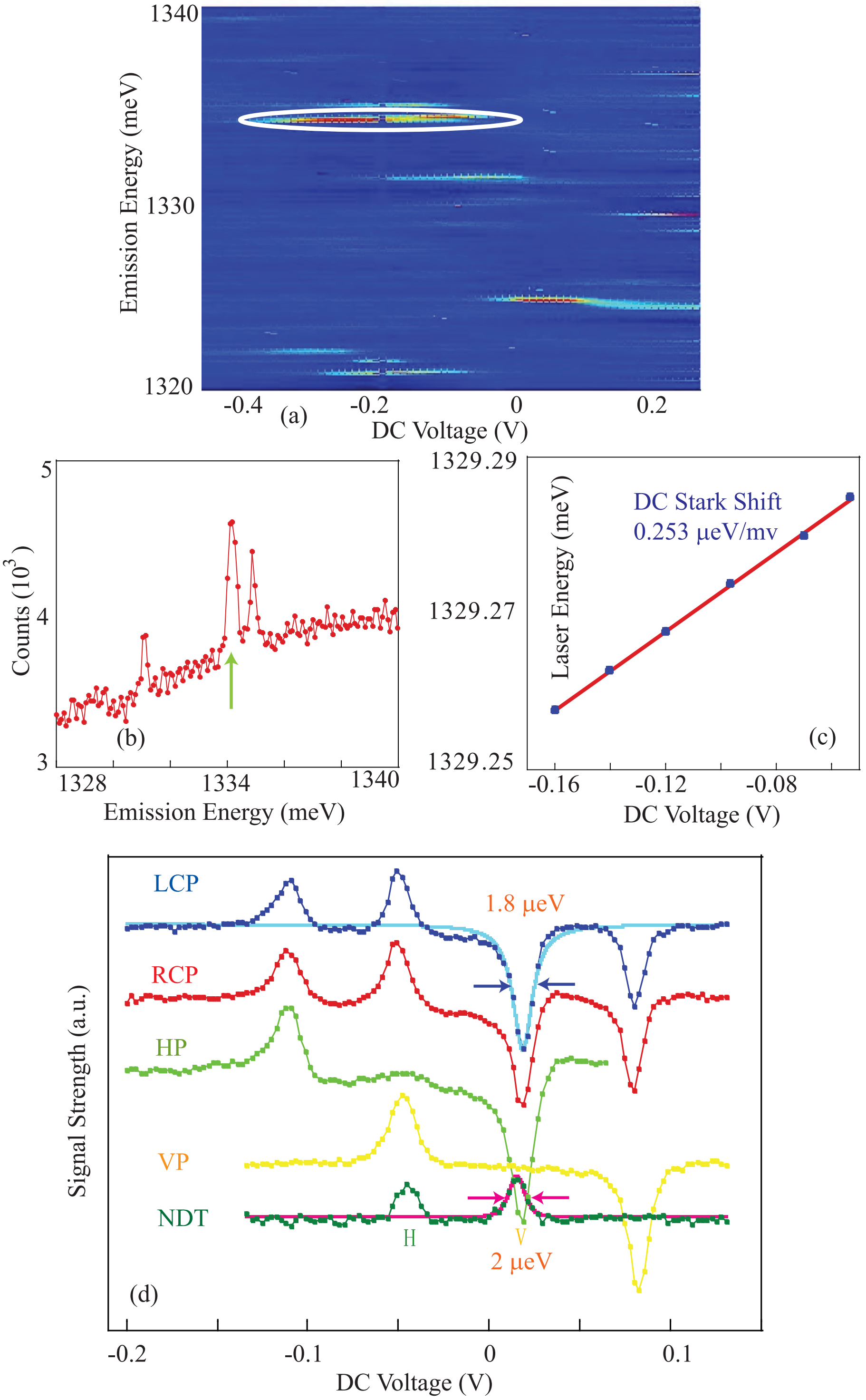

Figure 3.1: Optical Characterization of a Neutral Exciton. (a) Bias dependent PL intensity map. The white oval highlights the exciton state studied in this thesis. (b) A typical PL spectrum of the exciton state at an applied bias of -0.2 V. The green arrow points the exciton state. (c) Characterization of the DC Stark coefficient. (d) Top four curves: Polarization dependent absorption spectrum of an exciton state. Bottom curve: nonlinear DT responses of an exciton state.

A.1(d). For this data set, both pump and probe beams have equal power and are 45^o linearly polarized. Thus we observe the nonlinear responses from the two polarized exciton states in one scan. We can see that the spectral position of H (V) located exactly in the middle of two Lorentizan lineshapes in HP (VP) spectrum obtained by the DC stark shifted modulation. The red curve on top of the NDT data is the theoretical fitting with Lorentizan square function and yields a natural linewidth of 2 μeV (480MHz). This linewidth is comparable to the linear absorption result. After we identify a suitable neutral exciton state, we study the strong coupling of an neutral exciton state with laser radiations.

3.2 A neutral QD driven by a strong optical field

While strong optical excitation of a semiconductor creates a many body problem because of the extended nature of the exciton wave function [8], confinement of the wavefunction in quantum dots leads to strong energy level shifts between one exciton and two or more exciton states, enabling the system to be considered as a relatively simple few level problem. The strong field excitation regime of the transition from the ground state to an excited state such as the exciton, a Coulomb bound electron-hole pair, is then defined by $\Omega_R >> \gamma$ where the Rabi frequency $\Omega_R = \overrightarrow{\mu}.\overrightarrow{E}/\hbar$, γ/π is a transition line width (FWHM in Hz), $\overrightarrow{\mu}$ is the transition dipole moment and $\overrightarrow{E}$ is the amplitude of the optical electric field. For time scales less than $1/\gamma$, strong excitation leads to Rabi oscillations [9–11] in time. The effect of vacuum Rabi splitting (11) has also been observed in a single QD embedded in a nanocavity [26–28].

Under strong continuous wave (CW) narrowband resonant optical excitation of a simple atomic system, the fluorescence emission spectrum, which is a narrow emission line at low power (the emission width is the laser bandwidth) consists of three peaks referred to as the Mollow triplet [15], which has recently been demonstrated in a single neutral QD [16] and a single molecule with intense resonant pumping [17]. A simple picture of the origin of this emission pattern is understood from a dressed atom picture [18]. Figure 3.2(b) shows fully quantized atom-field states, when the driving field frequency ω is equal to the electronic frequency ω_o. In this limit, the "bare" states $|3, N-1>$ and $|2, N>$ are degenerate, where N labels the photon number of the driving field. The atom-field interaction lifts this degeneracy and produces "dressed" states $|\alpha(N-1)>$ and $|\beta(N-1)>$ having energy separation $\hbar\Omega_R$ as shown. The dressed states are linear combinations of the bare states. The dashed lines in the figure indicate a triplet of possible emission frequencies, occurring at ω and $\omega \pm \Omega_R$.

In absorption, the spectrum can be more complex. For the three level V system (Fig. 3.2(a)), where the strong field couples levels 2 and 3, theory predicts that the probe absorption from level 2 to level 1 is strongly modified from the usual simple Lorentzian seen in the absence of strong field excitation. The probe absorption splits into two resonances, known as the Autler-Townes (AT) splitting [19]. When the probe absorption on the strongly driven transition (between levels 2 and 3) is measured, the spectrum is much richer. New physics beyond that seen in the Mollow fluorescence triplet is observed [14, 17, 20–22] and arises from the coherent coupling between the two optical fields. When the Rabi frequency of the strong pump field is sufficiently large, the absorption spectrum shows gain without population inversion.

Since the neutral QD has two polarized exciton states, it forms a three level V system, which is excellent for the demonstration of AT splitting and Mollow absorption spectrum (MAS). Figure 3.2(c) shows the probe absorption spectra with different polarized light excitation. In this data set, we fix the gate voltage and scan the laser frequency. The lines on top of the data are Lorentizan fittings and match the data very well. In the following, first we are going to lay out the theoretical foundation of the strong coupling of the optical fields with a neutral exciton system. Then we will show the experimental results of AT splitting and MAS.

3.2.1 Optical bloch equations for a QD driven by a strong optical field

To analytically describe our experiments, we follow the approach used in [15, 25], describing the system with the optical Bloch equations $i\hbar\frac{d\rho}{dt} = [H, \rho] + Decay$, where

ρ and H are the density matrix and Hamiltonian of the light-coupled QD system, respectively. The Hamiltonian is given by $H = H_0 - \vec{\mu} \cdot \vec{E}$ where $\vec{E} = \vec{E}_0 + \vec{E}_1$. $\vec{E}_0$ is the strong pump field and $\vec{E}_1$ is the weak probe field. For calculations of the absorption spectrum, we can use the semiclassical approach where the fields are taken to be classical. H_0 is the diagonalized Hamiltonian for the quantum dot structure in the absence of external fields (Fig. 2(a)).

By solving the density matrix equations to all orders in the strong pump field and first order in the weak probe field, one finds that the absorption coefficient for the probe field is equal to [25]

$$\alpha_{AT} = \alpha_o Im \left\{ i \frac{4\left[\gamma_{13} - i\left(\delta' - \delta\right)\right]\rho_{22}^{(0)} - 2i\Omega_R \rho_{32}^{(0)}}{4\left(\gamma_{21} - i\delta'\right)\left[\gamma_{13} - i\left(\delta' - \delta\right)\right] + \Omega_R^2} \right\} \tag{3.1}$$

where α_o is a constant, $\delta = \omega_{32} - \omega$, $\delta' = \omega_{12} - \omega'$, ω' is the probe field frequency, $\gamma_{21} = \frac{\gamma_1}{2} + \Gamma_{21}$, $\gamma_{13} = \frac{(\gamma_1+\gamma_3)}{2} + \Gamma_{13}$, $\gamma_{23} = \frac{\gamma_3}{2} + \Gamma_{23}$, $\gamma_i$is the population decay rate for state i, Γ_{ij} is a dephasing rate, and

$$\rho_{22}^{(0)} = 1 - \frac{\gamma_{23}\Omega_R^2/\left(2\gamma_3\right)}{\gamma_{23}^2 + \delta^2 + \gamma_{23}\Omega_R^2/\gamma_3}$$

$$\rho_{32}^{(0)} = -\frac{i\Omega_R/2}{\gamma_{23} + i\delta} \frac{\gamma_{23}^2 + \delta^2}{\gamma_{23}^2 + \delta^2 + \gamma_{23}\Omega_R^2/\gamma_3}.$$

Equation (7.7) can be written in a rather simple form when $\Omega_R >> \gamma_i, \Gamma_{ij}$. In that limit the probe absorption profile separates into two peaks whose positions, relative strengths, and widths can be predicted simply in the dressed state model. The splitting of the absorption profile is shown by the green arrows in Fig. 1B. For $\delta = 0$, the two peaks are symmetric, separated in frequency by Ω_R and have FWHM of $\gamma_{13} + \gamma_{23}$.

We now ignore level 1 and consider the absorption of a weak probe field on the 2-3 transition that is simultaneously driven by a strong pump field. Once more, we solve the two-level optical Bloch equations to all orders of the strong pump field and to first order in the weak probe field. Taking the pump field to be on resonance we get [25]

$$\alpha_{MS} = \alpha_o Im\left\{\frac{i\gamma_3\left[2\delta'^2\gamma_{23} - 2\gamma_{23}^2\gamma_3 - i\delta'\left(2\gamma_{23}^2 + 2\gamma_{23}\gamma_3 - \Omega_R^2\right)\right]}{2\left(\gamma_{23}\gamma_3 + \Omega_R^2\right)\left(\gamma_{23} + i\delta'\right)\left[\delta'^2 - \gamma_{23}\gamma_3 - i\delta'\left(\gamma_{23} + \gamma_3\right) - \Omega_R^2\right]}\right\} \tag{3.2}$$

If the calculation were carried out using dressed states, one would surmise that the probe absorption spectrum consisted of three components, one centered at $\delta' = 0$ and two side bands centered at $\delta' = \pm\Omega_R$. If $\delta' \cong \pm\Omega_R$, Eq. (3.2) can be written as

$$\alpha_{MS} = \pm\alpha_o\frac{\gamma_3}{\Omega_R}\frac{\left(\delta' \mp \Omega_R\right)}{4\left(\delta' \mp \Omega_R\right)^2 + \left(\gamma_3 + \gamma_{23}\right)^2} \tag{3.3}$$

provided $\Omega_R >> \gamma_{23}$. Eq. (3.3) shows there are two dispersive line shapes as a function of the probe frequency centered at $\pm\Omega_R$ with their zero crossing at $\delta' = \pm\Omega_R$. When $\left|\delta'\right| > \Omega_R$, the probe experiences absorption. Strikingly, when $\left|\delta'\right| < \Omega_R$, the probe absorption is negative, i.e. the probe sees gain. This gain arises from a two-beam coupling of the strong pump and weak probe fields and occurs without a population inversion in any picture. The wings of the dispersive line shapes also provide nearly constant gain near$\delta' = 0$, but, exactly at $\delta' = 0$ the gain is canceled by a weak absorptive component. Explicitly, near $\delta' = 0$ one finds

$$\alpha_{MS} = -\frac{\alpha_o}{2}\left(\frac{\gamma_{23}}{\Omega_R}\right)^2\frac{\gamma_3}{\gamma_{23}}\left(\frac{\delta'^2/\gamma_{23}}{\delta'^2 + \gamma_{23}^2}\right) \tag{3.4}$$

The amplitude of the central component is $\frac{2(\gamma_{23}+\gamma_3)}{\Omega_R}$ times smaller than the height of the dispersive components.

3.2.2 The Demonstration Autler-Townes Splitting

To experimentally demonstrate the Autler-Townes effect [19], we use two frequency locked but independently tunable CW lasers with a mutual coherence bandwidth of a fewMHz. We set a horizontally polarized pump beam resonant with the H transition. A weak, vertically polarized probe beam then scans across transition V. The probe absorption spectra for different pump laser intensities are plotted in Fig. 3.3(a) with increasing pump intensity. The data are shifted vertically for clarity. In agreement with theory (solid lines) (7.7), the probe absorption splits into a doublet where each

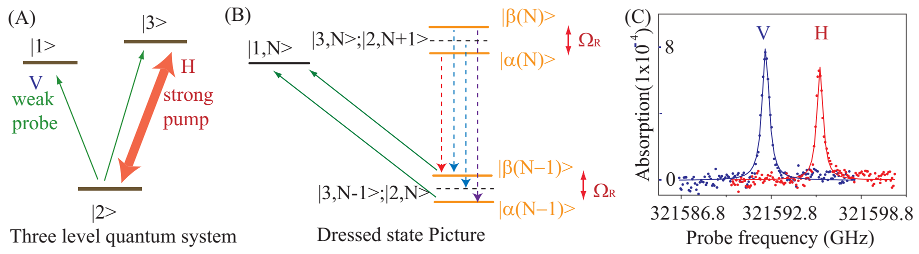

Figure 1

Figure 3.2: Dressed State Picture of a Neutral Exciton State (a) The energy level diagram of a single neutral QD. The absorption of the weak probe beam by scanning either transition V or H is modified by the strong pump beam which is near resonant with transition H. (b) The dressed state picture of the system shown in (A). The transitions between states |α,N> (|β,N>) and |1,N+1>, outside the energy range of the diagram, are not shown. If a weak beam probes transition 2-1 as shown by the green arrows, the absorption spectrum consists of a doublet. Ignoring the state|1>, the emission spectrum of transition 3-2 consists of three peaks (Mollow triplet): a peak centered at the electronic transitionω, and two Rabi side bands located at $\omega \pm \Omega_R$ (shown by the dashed lines). (c) Single beam, linear absorption profile of a single exciton state. The horizontally (vertically) polarized light only excites the corresponding linearly polarized exciton transition.

peak has equal strength. There is a small energy shift of the response relative to the low intensity excitation that is probably due to a small screening of the applied field by photo-excited charge in the diode. The shift saturates at a power between the lowest intensity curve and the next higher power spectrum. The pump laser is adjusted to follow the shift of the resonance.

The frequency separation between the absorption peaks shows a strong dependence on the pump intensity. We plot the measured splitting as a function of the square root of the pump intensity in the inset of Fig. 3.3(a). It clearly depends linearly on the pump field strength and goes to zero in the absence of the pump, as expected for the dependence of the Autler-Townes splitting on the Rabi frequency of the pump.

Figure 3.3(b) shows the probe absorption as a function of the pump detuning with a fixed pump intensity of $30I_0$ (the corresponding photon number per unit volume is approximately $1.4{\times}10^{10}/cm^3$), where $I_0 = 1.2W/cm^2$, corresponding to a Rabi frequency of approximately $\frac{\Omega_R}{2\pi} = 1.1\ GHz$. Again, the data are shifted for clarity, and the solid lines are the fitting of the data to the theory (7.7) and show good agreement. If the pump detuning is much larger than the transition linewidth, then optical field induced AC Stark effect can be observed. Though this is not focus of the current work, this AC stark effect in the quantum dot system has been demonstrated either by a strong pulse interacting with a neutral exciton system [26] or a strong CW beam interacting with a bi-exciton system [27].

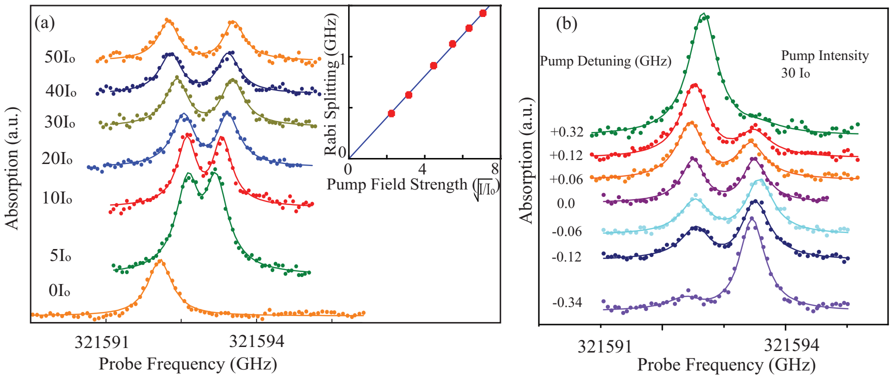

Figure 3.3: Demonstration of the Autler-Townes Splitting. Autler-Townes splitting using a single QD. A strong pump drives transition H and a weak probe scans across transition V. (a) Probe absorption spectra as a function of the pump intensity when the pump is on resonance. I_o equals $1.2W/cm^2$. The solid lines are theoretical fits to the data. The inset shows the AT splitting (Rabi splitting) as a function of the square root of the pump intensity. A linear fit (solid line) matches the data very well. (b) The probe absorption spectra as a function of the pump frequency detuning with fixed pump intensity. The lines are the theoretical fits to the data.

The AT splitting can provide a method to measure the dipole moment, as the Rabi frequency is a product of the transition dipole moment with the optical field. From the extracted Rabi splitting with the corresponding optical field strength, we can infer a transition dipole moment of about 30 Debye for this particular QD. The Einstein A coefficient (spontaneous emission rate) of a QD in a medium is given as

$$\gamma_{sp} = \frac{9n^5}{(2n^2 + n_{QD}^2)^2} \times \frac{\omega_0^3 \mu^2}{3\pi\varepsilon_0 \hbar c^3} = \frac{9n^5}{(2n^2 + n_{QD}^2)^2}\gamma_{spo}, \tag{3.5}$$

where n (n_{QD}) is the refractive index of the medium (QD), γ_{spo} is the spontaneous emission rate of a two-level quantum system in the vacuum [28, 29]. By taking $n = n_{QD} = 3.44$, inserting the experimental parameters and the extracted dipole moment into the equation, we obtain$\frac{\gamma_{sp}}{2\pi} = 190MHz$, which corresponds to a lifetime of about 840 ps. Assuming there is no other decay and no pure dephasing, this would lead to a natural linewidth expected in the low power absorption spectrum also equal to $\frac{\gamma_3}{2\pi} = 190\text{MHz}$, where γ_j is the decay rate of level j in Fig. 3.2(a). Compared to the extracted linewidth from the single beam, low power absorption data, which is about 500 MHz, γ_{sp} is about 2.5 times smaller. This discrepancy indicates that there is possibly a spectral wandering process which broadens the transition linewidth [24].

3.2.3 The demonstration of the optical Mollow absorption spectrum

In the MAS experiment, we set both pump and probe beams to be 45° linearly polarized and orthogonal to each other. The pump and probe beams coherently couple to the same transition and the pump field is tuned to resonance. We observe a relatively weak maximum centered at zero probe detuning and two Rabi side bands with dispersive lineshapes. The pump power dependence of the probe absorption spectra is shown in Fig. 3.4(a). The one beam absorption data is plotted at the bottom. The spectral shift of the data with the high power pump field is due to the excitation of the charge states in the buffer layer. The complex lineshape of the MAS depends strongly on the pump intensity. The splitting between the two side bands is plotted as a function of the square root of the pump intensity in Fig. 3.4(b), again showing that the splitting linearly depends on the pump field strength and is zero in the absence of the pump field.

The data confirms that the probe beam experiences optical gain in the pump-probe configuration for strong excitation. The data in Fig. 3A show that part of the probe absorption curve is below zero, which is the "gain" effect. Using the data corresponding to 15Io as an example, the absorption/gain ratio is about 0.066%/0.0024%=27.5. This gain is from the pump and probe beams coherently exchanging energy through the QD and corresponds to gain without inversion since there is no population inver-

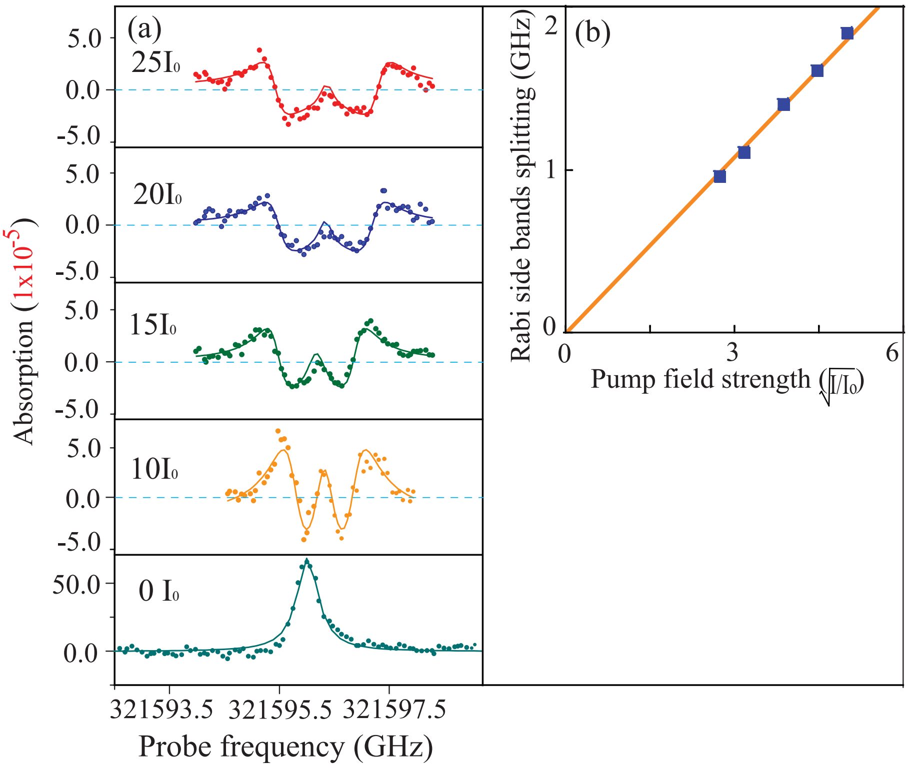

Figure 3.4: The Mollow Absorption Spectrum of a Neutral QD. Mollow absorption spectrum when the strong pump and weak probe beams couple to the same transition. (a) Measured probe absorption vs. pump field intensity when the pump is on resonance. The lines are the fits to the probe absorption function obtained by solving optical Bloch equations. The stocktickerMAS data show that the part of the absorption signal is “negative”. Using the data corresponding to 15Io as an example, the absorption/gain ratio is about 0.066%/0.0024%=27.5. (b) The splitting between the Rabi side bands vs. pump field strength. The solid line is the linear fit to the data.

sion either in the dressed or bare atom pictures.

Interesting features can also be observed when the pump beam is detuned from the QD transition. In this situation, gain effect can be demonstrated, but with Lorentizan lineshape sidebands and population inversion in the dressed state picture [18]. We are going to show the pump detuned MAS in the next chapter.

3.3 Chapter 3 Summary

In this chapter, we show the characterization and coherent optical spectroscopy of a single neutral SAQD. We present experimental results of the AT splitting and complex Mollow absorption spectrum using a single semiconductor QD [15]. We coherently control the probe absorption with a strong optical field, thus demonstrating that the single QD coupled with the strong pump can function as a modulator of the probe absorption [32]. In addition, the spectrum as a function of the probe frequency shows Rabi splitting and gain without population inversion. The results are in good agreement with the standard theory using the optical Bloch equations. Our work demonstrates that on long time scales, the discrete energy level spectrum of the dot is maintained even at the high field strengths needed for quantum logic operations (e.g., qubit rotations) and single photon devices, and that the system behaves similar to a trapped atom. The results suggest that it should now be possible to demonstrate numerous quantum level based applications, such as dressed state lasers [33], QD optical modulators [32], and quantum logic devices [34].

References

[1] M. E. Ware *et al.*, *Phys. Rev. Lett.* **95**, 177403 (2005).

[2] R. J. Warburton *et al.*, Nature **405**, 926 (2000).

[3] Benito Alen *et al.*, Appl. Phys. Lett. **83**, 2235 (2003).

[4] 26. D. Gammon, E. S. Snow, B. V. Shanabrook, D. S. Katzer, D. Park, *Phys. Rev. Lett* **76**, 3005 (1996).

[5] N. H. Bonadeo *et al.*, Phys. Rev. Lett. **81**, 2759 (1998).

[6] J.R.Guest *et al.*, Science **293**, 2224 (2001).

[7] Gang Chen *et al.*, Science **289**, 1906-1909 (2000).

[8] L. J. Sham, T. M. Rice, *Phys. Rev.* **144**, 708 (1966).

[9] T. H. Stievater*et al.*, Phys. Rev. Lett. **87**, 133603 (2001).

[10] H. Htoon *et al.*, Phys. Rev. Lett **88**, 087401 (2002).

[11] A. Zrenner *et al.*, Nature **418**, 612 (2002).

[12] J. P. Reithmaier *et al.*, *Nature* **432**, 197 (2004).

[13] T. Yoshie *et al.*, *Nature* **432**, 200 (2004).

[14] K. Hennessy *et al.*, *Nature* **445**, 896 (2007).

[15] B. R. Mollow, *Phys. Rev.* **188**, 1969 (1969).

[16] A. Muller *et al.*, Phys. Rev. Lett. **99**, 187402 (2007).

[17] G. Wrigge, I. Gerhardt, J. Hwang, G. Zumofen and V. Sandoghdar, Nature Phys. **4**, 60 (2008).

[18] J. Dupont-Roc, G. Grynberg, C. Cohen-Tannoudji, *Atom-Photon Interactions: Basic Processes and Applications* (John Wiley and Sons Inc, 1998).

[19] S. H. Autler, C. H. Townes, *Phys. Rev.* **100**, 703 (1955).

[20] E. V. Baklanov, V. P. Chebotaev, *Sov. Phys. JETP* **34**, 490 (1972).

[21] B. R. Mollow, *Phys. Rev. A.* **5**, 2217 (1972).

[22] S. Haroche, F. Hartmann, *Phys. Rev. A* **6**, 1280 (1972).

[23] F. Y. Wu, S. Ezekiel, M. Ducloy, B. R. Mollow, *Phys. Rev. Lett.* **38**, 1077 (1977).

[24] M. T. Gruneisen, K. R. MacDonald, R. W. Boyd, J. Opt. Soc. Am. B **5**, 123 (1988).

[25] P. Meystre, M. Sargent, *Elements of Quantum Optics* (Springer-Verlag, Heidelberg, 1998), chap. 9, [Third Edition].

[26] T. Unold *et al.*, Phys. Rev. Lett. **92**, 157401 (2004).

[27] Gregor Jundt, Lucio Robledo, Alexander Hogele, Stefan Falt, and Atac Imamoglu, Phys. Rev. Lett. **100**, 177401 (2008).

[28] J. R. Guest *et al.*, Phys. Rev. B. **65**, 241310(R) (2002).

[29] A. Thranhardt, C. Ell, G. Khitrova, H. M. Gibbs, *Phys. Rev. B.* **65**, 035327 (2002).

[30] A. Hogele *et al.*, *Phys. Rev. Lett.* **93**, 217401 (2004).

[31] Xiaodong Xu *et al.*, Science **317**, 929 (2007).

[32] S. G. Carter *et al.*, *Science* **310**, 651 (2005).

[33] N. Lu, P. R. Berman, *Phys. Rev. A.* **44**, 5965 (1991).

[34] D. Gammon, D. G. Steel, *Physics Today* **55**, 36 (2002).

CHAPTER 4

The Optical Mollow Absorption Spectrum of a Single Negatively Charged Quantum dot

Recently, an electron spin trapped inside a quantum dot has drawn intensive research interest due to its unique properties. It has been experimentally shown that the electron spin has long relaxation [3] and decoherence times [2, 6], which are critical features for quantum logic applications [4]. Much progress has been made in this direction, such as the electron spin state initialization [2,6] and optical generation and control of the electron spin coherence [6, 8, 9, 24].

One important task is to understand and control the physical properties of a singly-charged QD in the strong optical field regime, i.e. the light-matter interaction strength is much larger than the transition linewidth, under both resonant and nonresonant excitation. As we showed in the last chapter for an ideal two level atomic system, the strong coupling leads to interesting spectral features, such as Rabi side bands in the absorption and, strikingly, the amplification of a probe beam. These effects are known as the Mollow absorption spectrum (MAS).

Due to the unique atomic properties of the QD system, many body effects which dominate the nonlinear optical response in higher dimensional heterostructures are strongly suppressed. In the last chapter, we showed the Autler-Townes splitting and MAS in a neutral QD system. It is clear that a negatively charged quantum dot has similarities to a negative ion. However, the excited state of a dot is a many body system comprised of two electrons and a hole. The Fano interference effect, which arises from the coupling between a two-level system with a continuum [10], has been observed in a negatively charged QD [1, 6]. We are going to talk more about this observation of the Fano interference in the next chapter. The recent study of a single charged QD in the strong coupling regime does not exhibit the typical MAS [6,12,14]. All these indicate that interactions with a single charged QD could be more complex due to many body effects than the electron-hole system reported earlier in neutral dots [15,16]. Interestingly, the results in this chapter show that strong field excitation tuned near resonance in a negatively charged dot leads to changes in the absorption spectrum that are in excellent agreement with theory for a strongly driven two level system.

The chapter is organized as following. First we give the physical model of a trion state at zero magnetic field. Then we talk about the theoretical explanation of the MAS, especially the pump detuning conditions. Finally, we will present the experimental results and summarize this section.

4.1 The Physical Model of a Trion State at Zero Magnetic Field

We show the band structure of a single negatively charged QD in Fig. 7.1(a). Compared to a neutral QD, there is an excess electron in a negatively charged QD. The spin ground states of an electron are either spin up or spin down states in the lowest energy level of the conduction band. Since the neutral exciton state is an excited state, the electron spin states are favored over an exciton state as a qubit candidate. With the optical excitation, a trion state is generated with two electrons and one hole. Since the two electrons form a spin singlet state, the angular momentum of the trion states are determined by the hole spin. The electron spin ground states (trion states) are labeled as $\left|\pm\frac{1}{2}\right\rangle$ ($\left|\pm\frac{3}{2}\right\rangle$), where $\pm\frac{1}{2}$($\pm\frac{3}{2}$) denotes the angular momentum. The only dipole allowed transition is from the spin ground state $\left|\frac{1}{2}\right\rangle$ ($\left|-\frac{1}{2}\right\rangle$) to the trion state $\left|\frac{3}{2}\right\rangle$ ($\left|-\frac{3}{2}\right\rangle$) with σ^+ (σ^-) polarized light excitation. Since the spin flip Raman transitions are dipole forbidden, the trion system at zero magnetic field can be considered as a double two-level structure. Thus, we use the two-level optical Bloch equations to model the trion system. For simplicity, we labeled the electron spin ground state as state $|S\rangle$ and the excited state as $|T\rangle$, as shown in Fig 7.1(b).

4.2 Theory for the Trion Mollow

It is known that in a two-level system driven by a strong optical field, the absorption of the weak probe beam is significantly modified [6, 17, 18]. By solving the optical Bloch equations to all orders in the pump field and first order in the probe field, we obtain the absorption coefficient of the probe beam as [6]

$$\alpha = Im\left[\frac{\alpha_o \gamma_T A[i\gamma_T A^*(A^* + i\Delta) + \Delta(\frac{\Omega_R^2}{2} - \gamma B + i\,(B + i\Delta)\,\delta_1 + \delta_1^2)]}{\begin{array}{c}(\gamma_T^2 AA^* + i\Omega_R^2\gamma\Delta)(B^2 + \delta_1^2) + \gamma\Omega_R^4 B + \gamma_T(\Omega_R^2(\gamma + B)(\gamma B + \delta_1^2) \\ +i\gamma^2 B^2\Delta + i\delta_1^2\Delta(B^2 + \gamma^2 + \delta_1^2))\end{array}}\right], \tag{4.1}$$

where γ_T (γ) is the population (coherence) decay rate of the trion state, $\delta_1 = \omega_1 - \omega_o$ is the detuning of the pump frequency (ω_1) from the trion transition (ω_o), $\Delta = \omega_2 - \omega_1$ is the probe (ω_2) detuning from the pump, $A = \gamma + i\delta_1$, $B = \gamma + i\Delta$, α_o is a constant, $\Omega_R = \mu \cdot E_{\text{pump}}/\hbar$ is the Rabi frequency of the pump field, μ is the dipole moment matrix element and E_{pump} is the pump field strength.

When the strong pump is on resonance with the trion transition ($\delta_1 = 0$ and $\Omega_R >> \gamma$), the probe will show a complex Mollow absorption spectrum, which was discussed in detail in the last chapter, where a neutral exciton was studied with a strong resonant pump.

When the pump detuning is larger than the transition linewidth, the physics can be understood in the fully quantized dressed state picture. The uncoupled QD-field states (Fig. 7.1(c)) map into the dressed states (Fig. 7.1(d)) when the QD-field interaction is included. In Fig. 7.1(d), we assume the pump detuning δ_1 to be negative, $|S\rangle$ and $|T\rangle$ are the quantum dot states, and N is the photon number. Due to the light-matter interaction, one set of the dressed states can be written as [5]

$$|I(N)\rangle = c\,|S, N\rangle - s\,|T, N-1\rangle$$

$$|II(N)\rangle = s\,|S, N\rangle + c\,|T, N-1\rangle$$

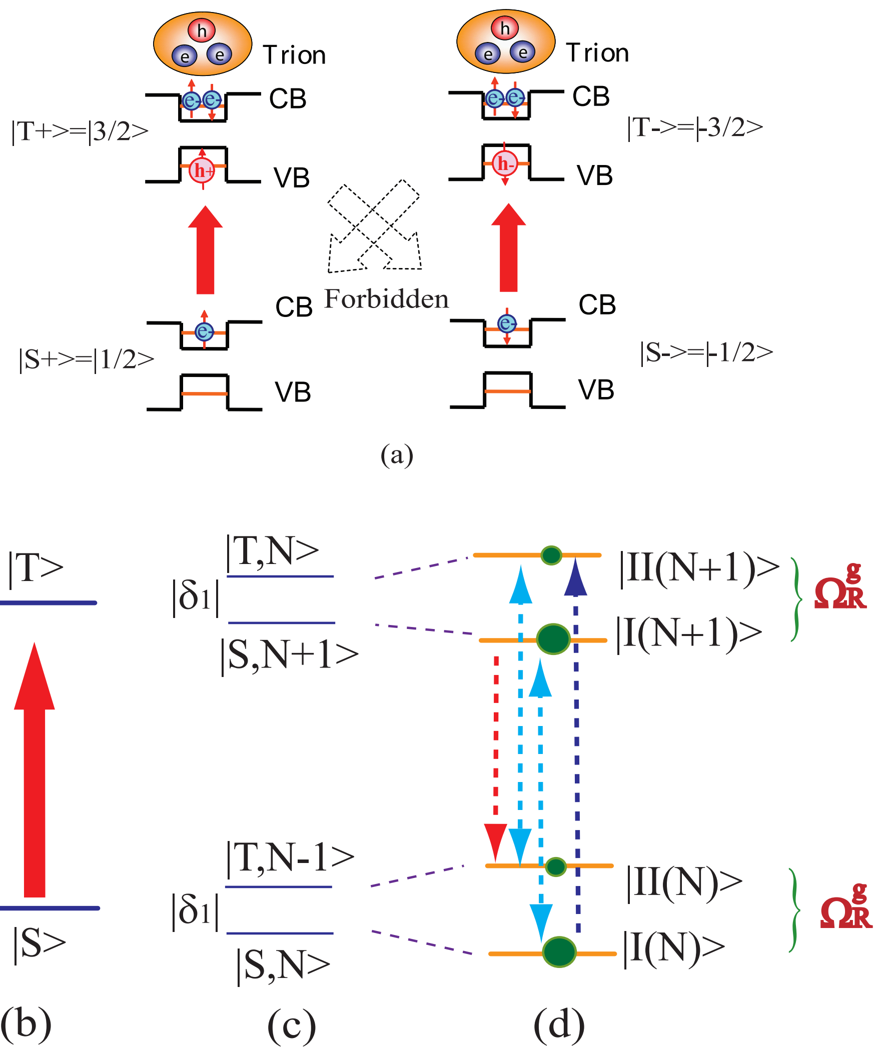

Figure 4.1: Band Structure and Energy Level Diagram of The Trion State (a) The band structure model of a single negatively charged QD in the absence of magnetic field. (b)The energy level diagram of a trion state at zero magnetic field. The absorption spectrum of the weak probe (green arrow) is modified by a strong pump field (red arrow). (c) The uncoupled atom-field states. (d) Dressed state picture of a two-level system driven by a strong optical field. The energy levels outside the picture are not shown. The energy splitting between the dressed states with the same photon number is $\hbar\Omega_R^g$, where Ω_R^g is the generalized Rabi frequency.

where $c = \sqrt{\frac{1}{2}\left(1 - \frac{\delta_1}{\Omega_R^g}\right)}$, $s = \sqrt{\frac{1}{2}\left(1 + \frac{\delta_1}{\Omega_R^g}\right)}$, and $\Omega_R^g = \sqrt{\Omega_R^2 + \delta_1^2}$ is the generalized Rabi frequency. The energy separation between the dressed states $|I(N)\rangle$ and $|II(N)\rangle$ is $\hbar\Omega_R^g$. As shown in Fig. 1(c), there are three transition frequencies: one centered at the pump frequency ω_1, and two Rabi side bands centered at frequency $\omega_1 \pm \Omega_R^g$.

Assuming $\Omega_R^g >> \gamma$ and using the secular approximation, i.e. ignoring the couplings between populations and coherence, the steady state solutions for the dressed state population are

$$\rho_{I,I} = \frac{c^4}{c^4 + s^4}, \rho_{II,II} = \frac{s^4}{c^4 + s^4}.$$

It is clear when $\delta_1 < 0$, the dressed state $|I(N)\rangle$ is more populated than the dressed state $|II(N)\rangle$. In Fig. 7.1(d), the size of the dots on states $|I(N)\rangle$ ($|I(N+1)\rangle$ and $|II(N)\rangle$ ($|II(N+1)\rangle$ indicates their population. Therefore, the transition centered at $\omega_1 + \Omega_R^g$ represents probe absorption (the purple dashed line in Fig. 7.1(d), and the transition centered at $\omega_1 - \Omega_R^g$ is probe gain due to the population inversion of the dressed states (the red dashed line in Fig. 7.1(d)). The gain process, in its simplest form, can also be considered as a three photon process, in which two pump photons are absorbed at frequency ω_1 and a third photon is emitted at frequency $\omega_1 - \Omega_R^g$ [20]. The light blue lines indicate transitions where the probe frequency is close to the pump frequency and the secular approximation fails. These can give rise to a dispersive lineshape [20, 21].

4.3 Trion Mollow Spectrum with a Strong Resonant Pumping

We first set the pump detuning δ_1 to zero and scan the probe frequency across the trion transition frequency ω_o. Figure B.1(a) shows the probe absorption lineshapes with various pump intensities. Instead of a Lorentzian absorption lineshape in the absence of the pump, as shown at the bottom of the Fig. B.1(a), the lineshape of the probe beam in the presence of a strong pump beam shows a complex structure. As we explained in the last chapter, a triplet-like absorption pattern appears with one weak central structure and two Rabi side bands.

The Rabi sidebands have dispersive lineshapes and zero crossings at $\pm\Omega_R$ provided

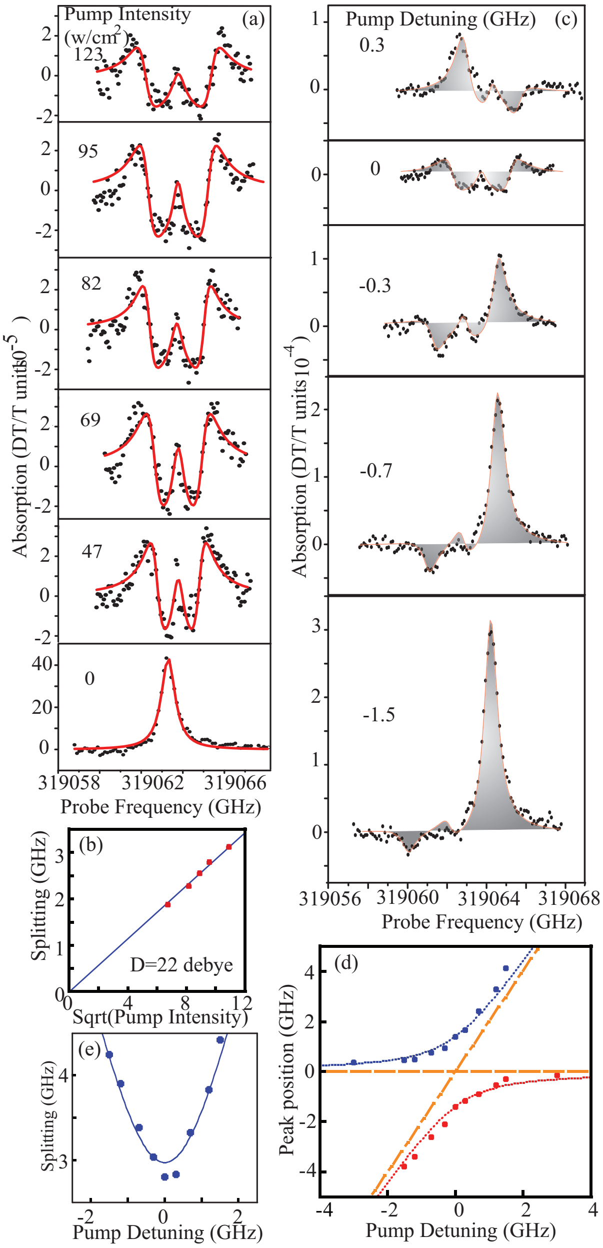

Figure 4.2: Trion Mollow Absorption Spectrum (a) Trion Mollow absorption spectrum as a function of the pump intensities with the resonant pumping. (b) The energy separation of the Rabi side bands as a function of square root of the pump intensity. (c) Trion Mollow absorption spectrum with various pump detuning with a fixed pump intensity of 95 W/cm^2. Two Rabi side bands are clearly observed, where one is the AC Stark shifted absorption peak and the other shows gain. (c) The spectral position of the Rabi side bands as a function of the pump detuning. We use the trion transition energy as the zero point. The anti crossing feature of the Rabi side bands is demonstrated as the pump is detuned from the red to the blue of the trion transition. (d) The energy separation of the Rabi side bands as a function of the pump detuning. The solid blue line is the fits by the formula $2\sqrt{\delta_1^2+\Omega_R^2}$.

$\Omega_R >> \gamma$. We extract the splitting of the Rabi side bands from the data and plot it as a function of the pump field strength in Fig. B.1(b). Since Ω_R is linearly proportional to E_{pump}, as expected, the extracted splitting depends linearly on the pump field strength and goes to zero in the absence of the pump. The observation of the Rabi side bands is a signature of the optical generation of single dot trion Rabi oscillations.

The negative part of the absorption lineshape demonstrates the gain of the probe beam, as shown by Fig. B.1(a). Since the pump is resonant with the trion transition, there is no population inversion in the steady state of the trion system in any picture. The gain effect comes from the coherent energy exchange between the pump and probe beams through the QD nonlinearity. We define the efficiency of the probe gain as the ratio of the amplitude of the negative absorption to the probe absorption in the absence of the strong pump. As an example, the probe gain efficiency corresponding to a pump intensity of 95 $watts/cm^2$ is 5.3 %. The earlier work by Kroner *et. al.* [12] did not observe the typical spectral features for a isolated two-level system, such as the dispersive side bands with optical gain effect, and they attribute this difference to possible effects of dephasing.

4.4 Trion Mollow Spectrum with a Detuned Pump

As we tune the pump laser frequency away from the trion transition, the dispersion-like lineshapes of the Rabi side bands evolve into three spectral features: one weak central structure with a dispersive lineshape and two Rabi side bands with Lorentzian lineshapes. Figure B.1(c) displays the probe absorption spectrum as a function of the pump detuning with a fixed pump intensity of 95 W/cm^2.

A distinct feature of the probe absorption spectrum is that one of the side bands shows purely negative “absorption”, which is the gain effect. Using the pump detuning at $-1.5\ GHz$ as an example (the bottom curve of Fig. B.1(c)), there is an absorption peak located at $\omega_1 + \Omega_R^g$. This is an AC stark shifted absorption peak. The side band centered at $\omega_1 - \Omega_R^g$ is negative, which signifies the amplification of the probe beam.

In lowest order perturbation theory, this reflects a three photon Raman gain effect: the QD absorbs two pump photons at frequency ω_1 and emits a photon at $\omega_1 - \Omega_R^g$. The frequency at which gain occurs can be tuned by adjusting the pump detuning. As expected, if the pump detuning is positive, the probe sees gain at $\omega_1 + \Omega_R^g$. The data with pump detuned $+0.3\ GHz$ is shown at the top of Fig. B.1(c). A gain peak is clearly observed for the positive detuning of the probe. It has been shown theoretically that the maximum gain occurs at the absolute value of the pump detuning $|\delta_1| = \Omega_R^g/3$ provided $\Omega_R^g >> \gamma$ [?]. For the pump detuning $-0.3\ GHz$, the data shows a probe gain of 9.7 %, which is much larger than under resonant pumping with the same intensity. When the probe frequency is nearly degenerate with the pump beam, there is also a small dispersive structure in the probe absorption spectrum, as shown in Fig. B.1(c)).

The solid lines in Fig. B.1(c) are theoretical fits of the data to Eq. (1). The fits yield $\gamma_T/2\pi$ and $\gamma/2\pi$ of (580 ± 90) MHz and (350 ± 35) MHz, respectively. Since γ_T is almost twice γ, the amount of pure dephasing in this QD is statistically insignificant compared with the error bars. These fits show that our results can be well reproduced by the optical Bloch equations and that the singly charged QD behaves like a single isolated atomic system.

Figure B.1(d) shows the spectral positions of the Rabi side bands as a function of the pump detuning. In the plot, we use the trion transition frequency ω_o as the zero energy point. Figure B.1(d) clearly illustrates the anti crossing behavior of the Rabi side bands. The separation between the two peaks at zero pump detuning represents the interaction strength between the light and QD, which is equal to the Rabi frequency. The dotted curves in the plot are the theoretical predictions of the peak positions as a function of the detuning, which is in good agreement with the measurements. The laser light induced transition energy shifts at the large pump detuning are a demonstration of the dynamic, or AC Stark effect.

We extracted the energy separation of the side bands from the data and plotted it as a function of the pump detuning in Fig. B.1(e). The solid blue line is a fit by the expression $2\sqrt{\Omega_R^2 + \delta_1^2}$ and gives $\Omega_R/2\pi = (1.5\pm0.1)\ GHz$. Since $\Omega_R = \mu \cdot E_{\text{pump}}/\hbar$, we infer a trion dipole moment of (25 ± 2) D. The trion dipole moment we calculated is similar to the reported neutral exciton dipole moment [15].

The Einstein A coefficient, or spontaneous emission rate, is [22]

$$\begin{aligned}\gamma_{\text{sp}} &= \frac{9n^5}{(2n^2+n_{\text{QD}}^2)^2}\frac{\omega_o^3\mu^2}{3\pi\varepsilon_o\hbar c^3} \\ &= \frac{9n^5}{(2n^2+n_{\text{QD}}^2)^2}\gamma_{\text{spo}}\end{aligned} \tag{4.2}$$

where γ_{spo} is the spontaneous emission rate in the vacuum, n and n_{QD} are the refractive index of the medium and the QD, respectively. By inserting the parameters into Eq. (4.2), we get a spontaneous emission rate of $2\pi \times 130$ MHz, which corresponds to a trion radiative lifetime of 1.2 ns. Assuming there is no pure dephasing in the QD, as we showed earlier, then the trion transition linewidth is about 130 MHz, which is smaller than what we extracted from our previous fits. Also, the low power single beam absorption data yields a transition linewidth of 600 MHz, which is much larger than what we calculated from the Einstein A coefficient. This discrepancy could come from the spectral diffusion process, which broadens the trion transition linewidth [15, 24].

4.5 Chapter 3 Summary

In summary, we have shown that an electron trapped inside a QD with its ground state and the excited two electron and one hole state behaves as an isolated quantum system even in the strong field limit by observing the optical Mollow absorption spectrum as well as the AC Stark effect. The behavior is well described by the solutions to the optical Bloch equations for a two-level system and show that the state of the electron can be switched at a rate of $2\pi\times1.6$ GHz with low power cw diode lasers.

References

[1] Miro Kroutvar *et al.*, Nature **432**, 81 (2004).

[2] J. R. Petta *et al.*, Science **309**,2180 (2005).

[3] A. Greilich *et al.*, Science **313**, 341 (2006).

[4] D. Gammon, D. G. Steel, Physics Today **55**, 36 (2002).

[5] Mete Atature *et al.*, Science **312**, 551 (2006).

[6] Xiaodong Xu *et al.*, Phys. Rev. Lett. **99**, 097401 (2007).

[7] M. V. Gurudev Dutt *et al.*, Phys. Rev. Lett. **94**, 227403 (2005).

[8] A. Greilich *et al.*, Science **317**, 1896 2007.

[9] J. Berezovsky, M. H. Mikkelsen, N. G. Stoltz, L. A. Coldren, D. D. Awschalom, Science **320**, 349(2008).

[10] U. Fano, Phys. Rev. **124**, 1866 (1961).

[11] M. Kroner *et al.*, Nature **415**, 311 (2008).

[12] M. Kroner *et al.*, Appl. Phys. Lett **92**, 031108 (2008).

[13] B. R. Mollow, Phys. Rev. A. **5**, 2217 (1972).

[14] F. Y. Wu, S. Ezekiel, M. Ducloy, B. R. Mollow, Phys. Rev. Lett. **38**, 1077 (1977);

[15] Xiaodong Xu *et al.*, Science **317**, 929 2007.

[16] A. Muller *et al.*, Phys. Rev. Lett. **99**, 187402 (2007).

[17] E. V. Baklanov, V. P. Chebotaev, Sov. Phys. JETP **34**, 490 (1972).

[18] S. Haroche, F.Hartmann, Phys. Rev. A **6**, 1280 (1972).

[19] J. Dupont-Roc, G. Grynberg, C. Cohen-Tannoudji, Atom-Photon Interactions: Basic Processes and Applications (John Wiley and Sons Inc, 1998).

[20] M. T. Gruneisen, K. R. MacDonald, R. W. Boyd, J. Opt. Soc. Am. B **5**, 123 (1988).

[21] G. Grynberg and C. Cohen-Tannoudji, Opt. Comm. **96**, 150 (1993); P. R. Berman and G. Khitrova, Opt. Comm. **179**, 19 (2000).

[22] A. Thranhardt, C. Ell, G. Khitrova, H. M. Gibbs, Phys. Rev. B. **65**, 035327 (2002); J. R. Guest et al., Phys. Rev. B. **65**, 241310(R) (2002).

[23] A. Hogele *et al.*, Phys. Rev. Lett. **93**, 217401 (2004).

CHAPTER 5

Fast Electron Spin State Preparation in a Single Negatively Charged Quantum dot

As discussed in Chapter 4, the use of electron spins in semiconductor quantum dots (QDs) as quantum bits (qubits) is being widely explored for quantum information and quantum computation (QIQC) [1–6]. A key element for QIQC is the initial quantum state preparation. QIQC requires not only qubits initialized in a known state for computation and gate operations, but also a continuous supply of low-entropy ancillary qubits for quantum error correction (QEC) [7, 8]. A fault-tolerant quantum computation requires about 10^4 quantum operations before the qubits lose their coherence [7, 8]. This requirement demands that the state initialization speed must be much faster than the quantum state decoherence rate.

The spin relaxation time (T1) of an electron spin trapped in a self-assembled In(Ga)As QD has been measured to be on the order of 20 ms [3], which sets an upper limit for the spin decoherence time in the absence of other interactions (*e.g.* phonon scattering, hyperfine interaction). The initialization of an electron spin state has been demonstrated recently in a singly-charged QD by applying magnetic fields in the Faraday geometry [2]. Although near unity fidelity is successfully achieved, the initialization rate is about $3 \times 10^5 s^{-1}$ [9], making it challenging for this scheme to satisfy the QEC requirement. A fast state initialization method with a high efficiency is essential for practical QEC processes.

In this chapter, we are going to present how to achieve fast spin state initialization in a singly charged QD. We will start with the characterization of the trion state at zero magnetic field, where the heavy and light hole mixing (HLHM) and nonlinear Fano effect are introduced. Then we will examine the theoretical and experimental results of the fast spin state initialization.

5.1 Polarization Dependent Study of a Singly Charged Quantum Dot at Zero Magnetic Field

In Chapter 4, the trion band structure model at zero magnetic field was illustrated. We learned there that the selection rules are either σ^+ or σ^- with degenerate transition energies, and there is no particular polarization axis for the QD. This statement is based on the assumption that there is no HLHM. This assumption is legitimate for the IFQD. However, it could fail for SAQDs due to the strong in-plane anisotropy [10–13]. When HLHM exists, the intermediate trion state is affected by the mixing, but not the electron spin ground state. The HLHM leads to a polarization axis ($\overrightarrow{\rho}$) of the QD which is intrinsic to the dot and the degree of polarization depends on the strength of the mixing between the heavy and light holes (see Chapter 2 for more details).

In the experiment, polarization dependent absorption spectroscopy is used to identify the HLHM effect. In previous reports, the HLHM effect has been observed in CdSe/ZnSe SAQDs [10, 12, 13] by polarization resolved PL spectroscopy. First we define the polarization of the light in the lab frame. The sample has a rectangular shape with the short axis parallel to the [110] direction and the long axis to the $[1\bar{1}0]$ direction, as shown in Fig. 7.1(a). The sample growth direction is along the [001] direction. Therefore, if the polarization of the light is parallel to the [110] ($[1\bar{1}0]$) direction, it is horizontally (vertically) polarized, as shown in the Fig. 7.1(a).

Figure 7.1(b) shows the normalized absorption signal strength as a function of the light polarizations, where H polarization is used as a zero degree point. A clear and moderate oscillation of the signal strength is observed as the polarization of the light is varied. The data can be fitted by the equation

$$Signal = 1 + \rho \times cos(\alpha - \theta) \tag{5.1}$$

where ρ is the degree of quantum dot polarization, α is the rotation angle of the

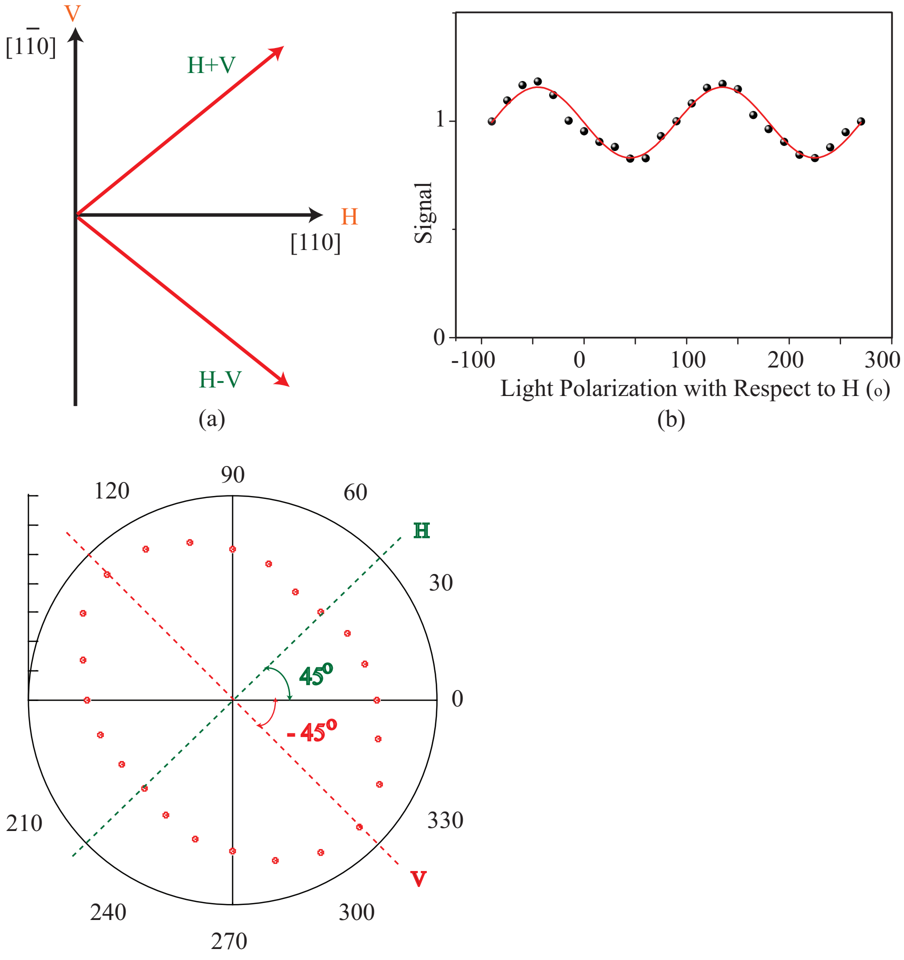

(a)

(b)

(c)

Figure 5.1: Signatures of Heavy-light Hole Mixing. Define the polarization of light in the lab frame. (b) The absorption signal strength as a function of rotation angle of a linear polarizer. The data are fitted by equation $Signal = 1 + \rho \times cos(\alpha - \theta)$. (c) The replot of data in (b) in the polar coordinates. Redefine the polarization of the laser light.

polarizer with respect to H polarized light, and θ is the angle of $\overrightarrow{\rho}$ with respect to H. In the fitting process, we limit $0 < \theta < 90°$. The dashed line on top of the data is the fit which yields $|\rho| = 0.16$ and $\theta = 45°$ for this particular quantum dot. The data in Fig. 7.1(b) are replotted in polar coordinates in Fig. 7.1(c) to clearly show that the QD is elliptically polarized. The long (short) axis is $-45°$ ($45°$) rotated away from the H axis. For simplicity, the short axis is defined as the polarization axis ($\overrightarrow{\rho}$) of the QD. From now on, the light polarized along (perpendicular to) $\vec{\rho}$ is referred to as horizontally (vertically) polarized, as shown in Fig. 7.1(c).

In a short summary, the HLHM in a charged QD is characterized by the polarization dependent absorption spectra. The HLHM effect leads to an intrinsic polarization axis of the QD. The direction of $\overrightarrow{\rho}$ and the degree of the polarization depend on the mixing strength of the HLHM.

5.2 Nonlinear Fano Interference Effect

The Fano interference effect is a classic example of a two level system coupled to a continuum and characterized by a factor q [14]. As shown in Fig. B.1(a), two discrete states $|0\rangle$ and $|1\rangle$ form a two level system and are coupled to each other with a strength of w. Both $|0\rangle$ and $|1\rangle$ also couple to the continuum states $|K\rangle$ with coupling strengths of u and v. The Fano q-factor is defined as

$$q = \frac{1}{\pi D} \frac{w}{uv} \tag{5.2}$$

where D is the density of the continuum states. This definition shows that when Fano q-factor is small (large), the Fano effect is strong (weak). The optical response of a two level system with Fano effect is described by the following formula

$$S(\omega) = \alpha \frac{((\omega - \omega_o) + q \times \gamma)^2}{(\omega - \omega_o)^2 + \gamma^2} \tag{5.3}$$

where γ is the decoherence rate between $|0\rangle$ and $|1\rangle$, and ω (ω_o) is the laser (atomic) frequency. The Fano effect has been observed in the atomic systems [15, 16]. Interestingly, we are able to observe a Fano interference effect in this charged QD. Furthermore, we show that we can control the Fano q-factor either with laser power, which is called a nonlinear Fano effect [17], or with the applied bias voltage across the sample.

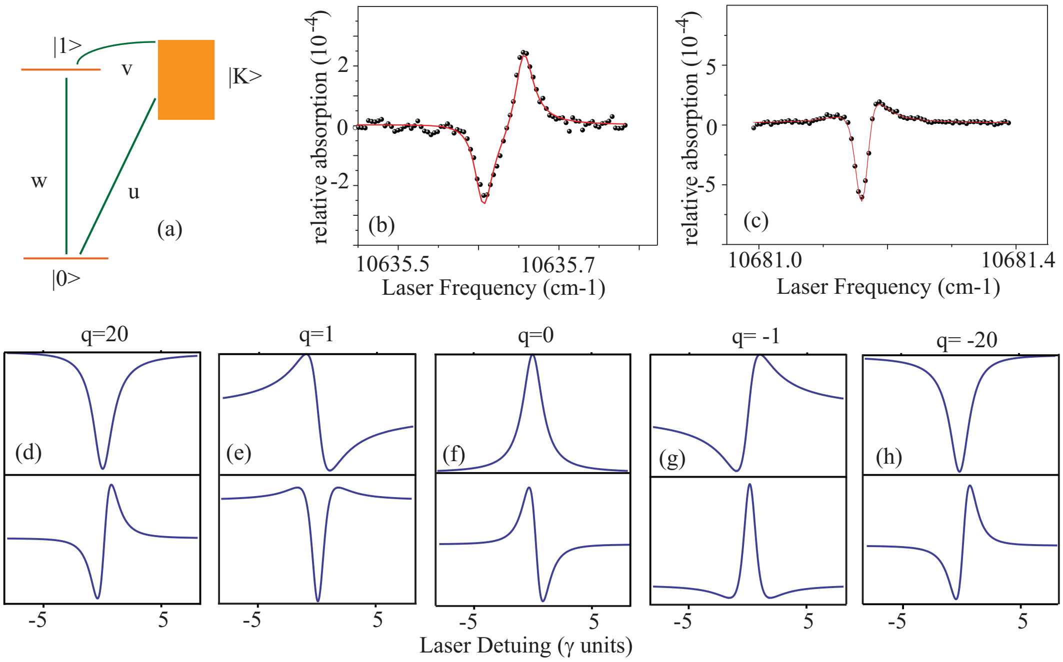

Figure 5.2: Signature of Fano Interference Lineshape (a) A two-level system coupled to a continuum. (b) The probe absorption spectrum of a non-Fano charged QD with a small DC stark shift modulation. (c) The probe absorption spectrum of a charged QD in the presence of Fano effect with a small DC stark shift modulation. (d-h) The theoretical plots of Fano interference lineshape with various q factors. In each figure, the top curves is the transmission spectrum and the bottom curve is the derivative of the top curve.

If the Fano effect does not exist, the absorption spectrum of a laser probing a single QD has a Lorentzian lineshape. Because of the voltage modulation technique, as we discussed in Chapter 2, the spectrum is either a Lorentizan lineshape for a large DC Stark shift modulation or a symmetric differential lineshape for a small modulation amplitude. Figure B.1(b) shows the probe absorption spectrum of the charged QD studied in Chapter 4 with a small modulation. A typical symmetric differential lineshape for a non-Fano QD is observed. However, Fig. B.1(c) shows the absorption spectrum with a small modulation of the charged QD used in this chapter, which shows a strong asymmetric differential lineshape caused by the Fano effect. Figure B.1(d-h) are the theoretical plots of Fano interference lineshape with various q factors. In each figure, the top curves is the transmission spectrum and the bottom curve is the derivative of the top curve. Ideally, a single QD is an isolated quantum system. However, due to the sample structure, a continuum could be formed in the barrier layer, which may couple to the QD states and lead to the Fano interference lineshape. A similar Fano effect in the QD system is also reported in Ref. [17] by an optical measurement and in [18] by a transport measurement.

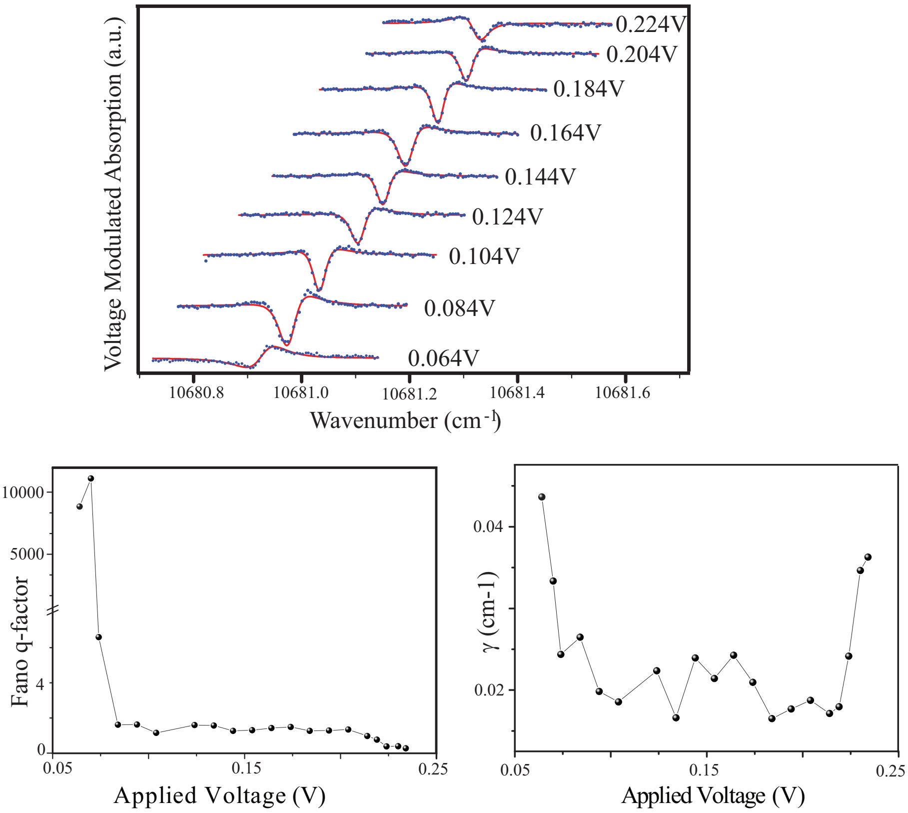

Figure 5.3: Bias Dependent Fano Effect (a) Bias dependent probe absorption spectra of a charged QD in the presence of the Fano effect. The lines on top of the data are theoretical fittings. (b) The extracted Fano q-factors and (c) trion decoherence rate γ as a function of the applied bias.

The Fano effect is examined as a function of the bias voltage first. The plots in Fig. 7.3(a) show the evolution of the lineshape as a function of the applied bias. As the bias voltage is tuned from low to high, the absorption lineshape evolves from symmetric to strongly asymmetric. The data are fitted by the follow equation

$$S\left(\omega,\omega_o+\kappa\right)-S\left(\omega,\omega_o-\kappa\right)=\frac{4\alpha\kappa\gamma\left(\gamma\delta-q^2\gamma\delta+q\left(\kappa^2+\gamma^2-\delta^2\right)\right)}{\kappa^4+2\kappa^2\left(\gamma^2-\delta^2\right)+\left(\gamma^2+\delta^2\right)^2},$$

where $\delta = (\omega - \omega_o)$ is the laser detuning and κ is half of the modulation amplitude. The red solid lines on top of the data are the fits. The q-factors are extracted from the fits and plotted in Fig. 7.3(b) as a function of the applied bias. The q factor starts as a large positive number at a low bias voltage, which means the absence of the Fano effect and falls to a finite positive number as we increase the bias. Therefore, the coupling of the QD with the continuum states can be controlled by varying the bias voltage. The bias dependent γ is also plotted in Fig. 7.3(c). The increase of γ at the edge of the trion plateau is caused by co-tunneling induced linewidth broadening [19]. At the edge of the trion plateau, the electron in the dot is not stable and tunnels back and forth between the back contact and the QD with a considerable rate, which leads to the increase of γ.

The Fano interference effect as a function of the excitation laser power was also investigated. Fig. 5.4(a) shows the absorption spectra by varying the laser power at a bias voltage of 0.14 V. It shows that the lineshape changes from somewhat symmetric to strongly asymmetric as we increase the laser power, which indicates that the coupling of the QD system to the continuum states gets stronger as we increase the laser power. The observed nonlinear Fano effect agrees with the report in Ref [17]. The lines on top of the data are theoretical fits. The extracted q-factors are plotted as a function of the excitation power in Fig. 5.4(b), which shows a “saturation” type behavior. The q-factor approaches a constant as the power increases. The line on top of the data is a guide to the eye.

Figure 5.4(c) shows the extracted γ as a function of the laser power. The increase of the transition linewidth as the laser power increases is known as the power broadening effect [20], which will be discussed in the next section. The data are fitted with the power broadening function $\gamma_o\sqrt{1 + I/I_s}$, which yields $\gamma_o = 0.015cm^{-1}$ (or 450 MHz) and the saturation intensity $I_s = 4.7I_o$, where $I_o = 1W/cm^2$. The signal strength is also checked as a function of the laser power and the data are plotted in Fig. 5.4(e), which also shows the saturation effects. The fit of the data yields the saturation intensity of $4.2I_o$, comparable to the number we got from the fit of γ.

The peak position shifts as the laser power increases, as shown in Fig. 5.4(a).

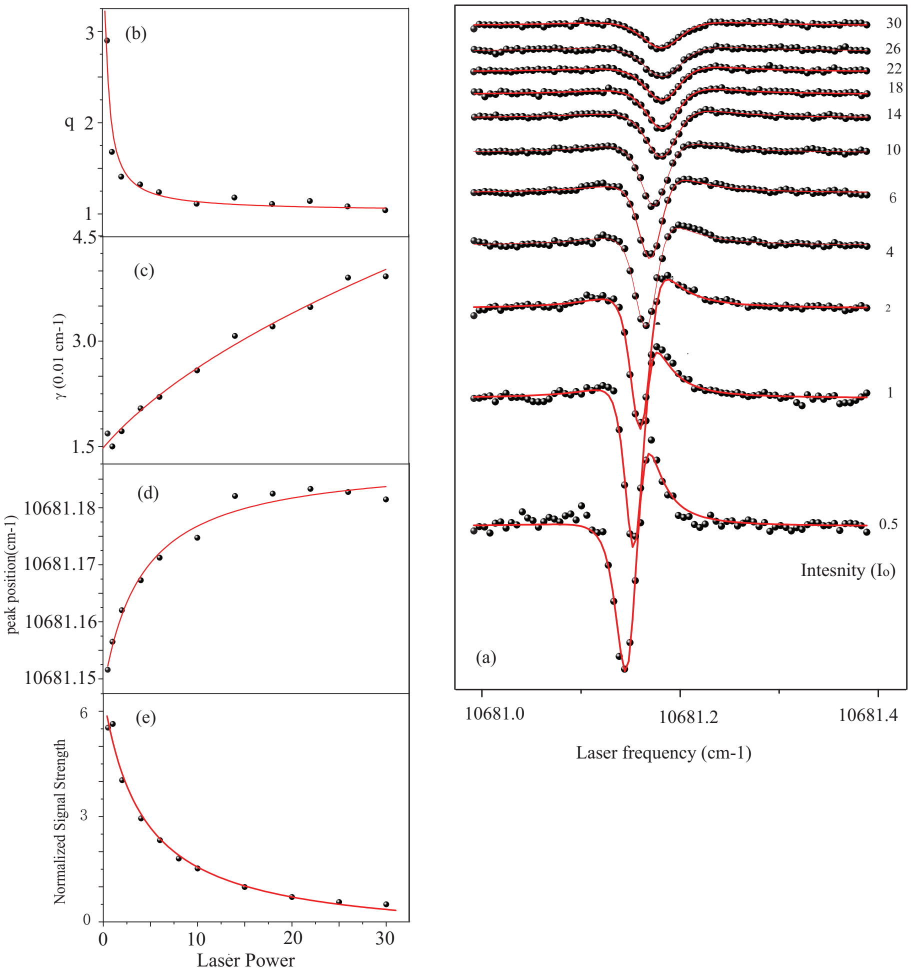

Figure 5.4: Laser Power Dependent Fano Effect. (a) Laser power dependent VM absorption spectra. The extracted (b) Fano q-factor, (c) γ, (d) peak position, and (e) signal strength as a function of laser power.

This trend is displayed in Fig. 5.4(d), which shows the saturation effect. The data are fitted with a saturation function and yields a saturation intensity of 4.1 I_o. This power induced frequency shift could arise from the excitation of carriers in the buffer layer, as discussed in Chapter 4.

In a short summary, the Fano interference effects are observed in a single charged QD system by the optical absorption measurement. It is demonstrated that the coupling strength between the QD states and the nearby continuum can be controlled by both bias voltage and laser excitation power.

5.3 Fast Spin State Initialization

The ultimate limit on the optical pumping rate in the Faraday geometry is the fact that the spin flip Raman transition is ideally dipole forbidden. In order to implement a fast spin state initialization, the dark transitions have to become bright, since the optical pumping rate depends on the spin flip Raman scattering process. This can be realized by applying a magnetic field perpendicular to the sample growth direction [001]. As discussed in Chapter 2, the B field induces off diagonal terms in the Hamiltonian that couple both electron and hole states. The coupling leads to linearly polarized transitions from the spin ground states to the trion states. Figure 5.6(b) shows the corresponding four level trion model, where $|x\pm\rangle$ ($|t\pm\rangle$)are the spin (trion) eigenstates in the magnetic field. The Zeeman splitting of the electron spin (trion) states is $|g_{e\perp}\mu_B B_x|$ ($|g_{h\perp}\mu_B B_x|$), where $g_{e\perp}$ ($g_{h\perp}$) is the electron (hole) spin in-plane g factor, μ_B is Bohr magneton, and B_x is the applied magnetic field. The four linearly polarized transitions are labeled as V1, H1, H2, and V2, where $\overrightarrow{V1}||\overrightarrow{V2} \perp \vec{\rho}$ and $\overrightarrow{H1}||\overrightarrow{H2}||\ \vec{\rho}$.

In the following, the system is modeled with the optical Bloch equations, followed by the derivations of the analytical formulas for the optical pumping rate and the fidelity of the spin state initialization. The experimental results will be discussed afterwards.

5.3.1 Theoretical Calculations of Fast Spin State Initialization

In the optical pumping scheme, the pump laser is set to be on resonance with one trion transition. Hence, the four level model can be reduced to a three level Lambda system, as shown by Fig. 5.5, where 1 and 3 denote the spin ground states, 2 represents the trion state, $\Gamma_{ij}(\gamma_{ij})$ is the decay (decoherence) rate from state $i \rightarrow j$, and $E(\omega)$ is the pump laser, which only interacts with transition $1 \rightarrow 2$. The Hamiltonian of the system can be written as

$$H = \begin{pmatrix} 0 & X_{12} & 0 \\ X_{21} & \omega_{21} & 0 \\ 0 & 0 & \omega_{31} \end{pmatrix},$$

where X_{ij} is the interaction term between the light and quantum dot transition. The density matrix equation can be derived from [20]

$$i\frac{d\rho}{dt} = [H, \rho] + Decay$$

.

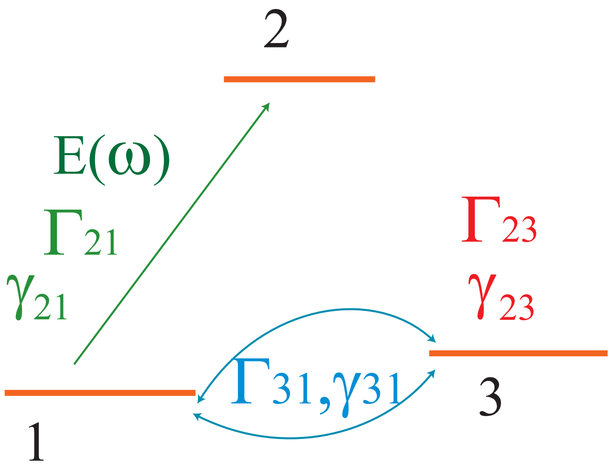

Figure 5.5: Schematic of A Three Level Lambda System

From the above formula, the rate equation for spin state 1 is derived as

$$\dot{n_1} = \Gamma_{21}\, n_2 + \Gamma_{31}(n_3 - n_1) + \frac{2\left|X_{21}\right|^2 \gamma_{21}}{\gamma_{21}^2 + (\omega_{21} - \Omega_1)^2}(n_2 - n_1) \tag{5.4}$$

where n_i is the population of state i. Solving the rate equation, we get

$$n_2 - n_1 = -\frac{\Gamma_2\Gamma_{31}}{(3A + 2\Gamma_{21})\Gamma_{31} + \Gamma_{23}(A + 2\Gamma_{31})}, \tag{5.5}$$

where

$$A = \frac{2\left|X\right|^2\gamma_{21}}{\gamma_{21}^2 + (\omega_{21} - \Omega_1)^2} \tag{5.6}$$

In the equation, X is half of the Rabi frequency Ω.

Therefore, the absorption of the pump beam is

$$Im[\rho_{21}] = \alpha\frac{\gamma_{21}^2}{(1 + I/I_s)\gamma_{21}^2 + (\omega_{21} - \Omega_1)^2},$$

where

$$I_s = \frac{\hbar^2\Gamma_2\Gamma_{31}\gamma_{21}}{(3\Gamma_{31} + \Gamma_{23})\mu_{21}^2}$$

is the saturation intensity for a three level Lambda system. One should note that if I is much smaller than I_s, then the transition linewidth is $2\gamma_{21}$. However, if I is comparable or larger than I_s, then the transition linewidth is $2\sqrt{(1 + I/I_s)}\gamma_{21}$, which is known as power broadening.

Assuming the spin relaxation rate $\Gamma_{31} \ll \Gamma_{23}$, the saturation intensity for a three level Lambda system has the following formula

$$I_s = \frac{\hbar^2\Gamma_2\Gamma_{31}\gamma_{21}}{\Gamma_{23}\mu_{21}^2} = I_s^{two} \times \frac{\Gamma_{31}}{\Gamma_{23}},$$

where

$$I_s^{two} = \frac{\hbar^2\Gamma_2\gamma_{21}}{\mu_{21}^2}$$

is the saturation intensity for a two level system. Hence, it is shown that the saturation intensity of a three level system is a factor of $\frac{\Gamma_{31}}{\Gamma_{23}}$ smaller than two level system. If the spin relaxation rate is on the order of ms^{-1} and trion relaxation rate Γ_{23} is on the order of ns^{-1}, then the former is a factor of 10^6 smaller. It indicates that since the trion transition is easily saturated, we are likely to achieve optical pumping effect in a charged QD system.

Now we examine how quickly the electron spin state can be initialized, i.e. in what time scale the system can reach the steady state. By writing out the explicit density matrix equations from Eqn 5.3.1, we can see that there are only three independent variables, which can be rewritten as a vector [21]

$$\overrightarrow{V} = (n_1, n_3, Im[\rho_{12}])'$$

The density matrix equations can be written as

$$\frac{d\overrightarrow{V}}{dt} = \widehat{A}\overrightarrow{V} + \overrightarrow{B}$$

where

$$\begin{aligned} \widehat{A} &= \begin{pmatrix} -\Gamma_{31} - \Gamma_{21} & \Gamma_{31} - \Gamma_{21} & 2X \\ \Gamma_{31} - \Gamma_{23} & -\Gamma_{31} - \Gamma_{23} & 0 \\ 2X & X & -\gamma_{21} \end{pmatrix} \\ \overrightarrow{B} &= (\Gamma_{21}, \Gamma_{23}, X)' \end{aligned}$$

The solution of $\overrightarrow{V}$ is proportional to $e^{\overrightarrow{A}t}$. The eigen value of $\overrightarrow{A}$ equals

$$\begin{aligned} \lambda = \frac{\Gamma_{23}}{6b\kappa^{1/3}}(3^{2/3} + 2 \times 3^{2/3}b + 3^{2/3}b^2 - 16 \times 3^{2/3}r^2 \\ - 3\kappa^{1/3} - 3b\kappa^{1/3} + 3^{1/3}\kappa^{2/3}), \end{aligned} \tag{5.7}$$

$$\kappa = 72r^2 + \frac{1}{3}[46656r^4 - 27(1 + 2b + b^2 - 16r^2)^3]^{1/2}, \tag{5.8}$$

where $r = \frac{\Omega}{\Gamma_{21}}$ and the branching ratio b is $\frac{\Gamma_{23}}{\Gamma_{21}}$. Therefore, the characteristic time for the system is $-1/\lambda$, i.e. the optical pumping rate is $-\lambda$. If we take $b = 1$ and $r >> 1$, the optical pumping rate is $\Gamma_{23}/2$ [21].

In the above, the optical pumping rate is derived by assuming a three level Lambda system. However, a 4 level trion model has to be adopted to derive the initialization fidelity. The reason is that the outer pair of transitions of the trion model have the same selection rules (see Fig. 5.6(b)). When the pump laser is on resonance with one of the transitions, it will be off resonantly coupled to the other transition. This bi-directional pumping effect will slightly reduce the optical pumping efficiency. The detailed procedure for deriving the optical pumping efficiency can be found in the Appendix (A). The basic idea is to use the rate equation approximation. Assuming the laser is pumping the transition from 1 to 2 and solving the rate equations, we can get

$$n_1 = (\Omega^2 + \Gamma^2)/(4\Omega^2 + 2\Gamma^2 + \Delta^2)$$

where we take all excited state decay rates as Γ, Δ is the detuning of the laser to the transition V2 and equivalent to the sum of the electron and hole Zeeman splitting. Then the ideal optical pumping efficiency equals $(1 - n_1)$. In principle, the spin preparation efficiency can be improved by increasing the magnetic field.

5.3.2 Experimental Results

In this section, the experimental results of the fast spin state initialization are discussed. Figure 5.6(a) shows the VM absorption map as a function of the applied bias at a magnetic field of 0.88 T along the [110] axis. The laser field is linearly polarized and 45° to the polarization axis ($\vec{\rho}$) of the quantum dot. The difference in the range of the applied bias between PL and VM maps arises from the local electric field effect, which depends on the excitation wavelength [19]. In bias region II, the optical pumping rate is larger than the spin relaxation rate. Fast spin cooling is demonstrated, where the absorption of the laser beam is strongly suppressed by optical pumping. In region I, the co-tunneling (the tunneling of the electron between the quantum dot and the Fermi sea [2,22]) induced spin relaxation rate is comparable or larger than the optical pumping rate, so the depletion of the spin ground state is not achieved. Thus, the strong suppression of the absorption disappears in region I and a quartet transition pattern appears. The physics of the two bias regions is discussed below along with the bias dependent g factor associated with transitions H1 and H2.

We first start with the bias region I of Fig. 5.6(a). As mentioned earlier, when a magnetic field is applied along the [110] axis, it induces off diagonal terms in the Hamiltonian that couple both electron and hole states. The coupling leads to linearly

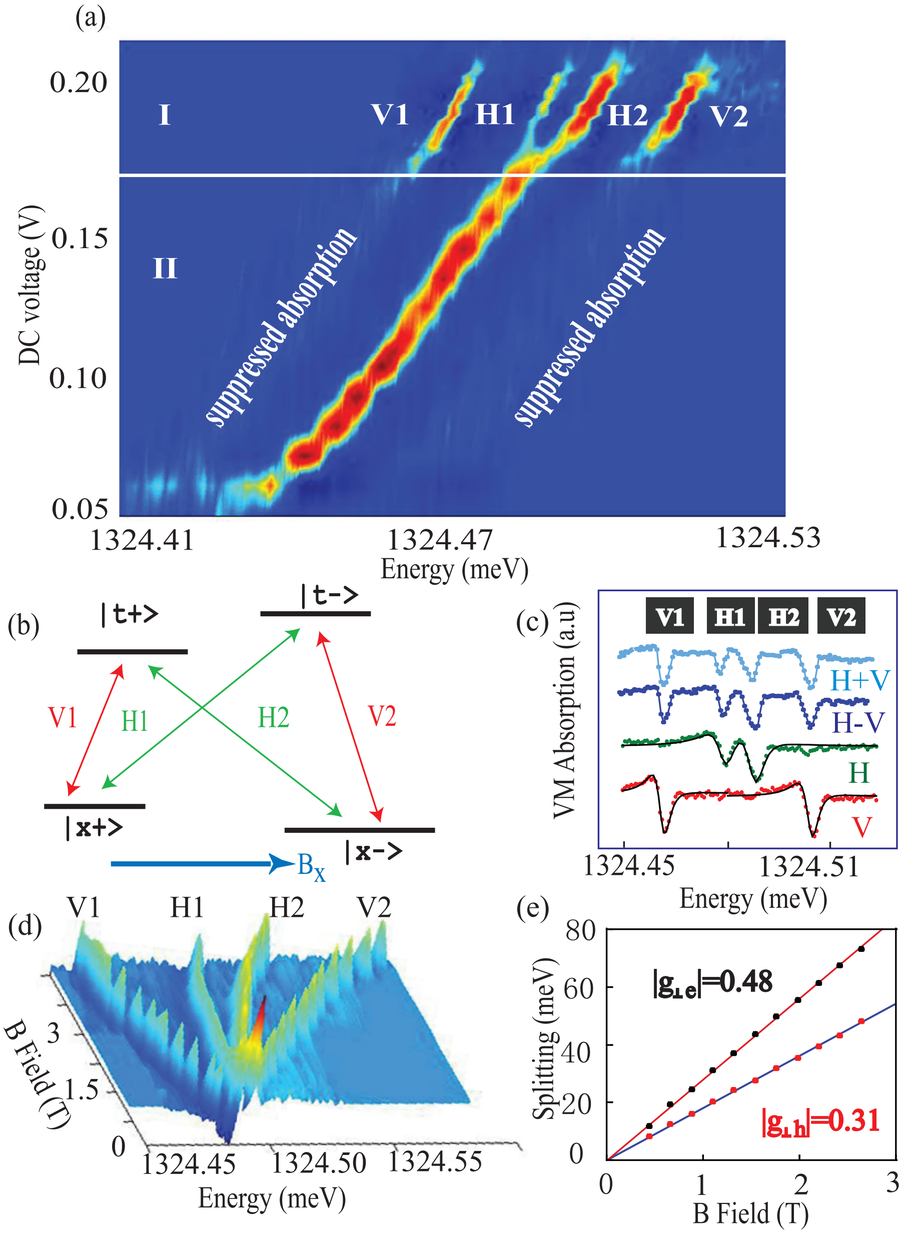

Figure 5.6: Demonstration of Optical Pumping Effect. (a) Bias dependent VM absorption map of a singly-charged SAQD at a magnetic field of 0.88 T. The laser is 45^o polarized. Voltage Region I shows all four trion transitions. Spin state preparation is achieved in Voltage range II. (b) Energy level diagram of a trion. The gate voltage is set at 0.19V for plots (c), (d), and (e). (c) Polarization dependent VM spectra of a singly-charged QD at magnetic fields $0.88T$. The black curves are the fittings. (d) 3d plot of the trion evolution with various magnetic fields. The laser is 45^o polarized. The data are inverted for clarity. (e) The electron (black dots) and hole (orange dots) Zeeman splitting as a function of the magnetic fields.

polarized transitions from the spin ground states to the trion states. Figure 5.6(c) shows the polarization study of the trion state at gate voltage 0.19 V. The lines on top of the data are the fits. A quartet transition pattern is excited with 45° linearly polarized light. When the light is vertically (horizontally) polarized, the optical field only excites the outer (inner) two transitions of the quartet. Thus, the inner and outer transitions are strictly linearly polarized and orthogonal to each other, which inhibits spontaneously generated coherence (SGC) [24]. The observation of the quartet demonstrates that under a transverse magnetic field all four trion transitions are optically allowed and obey well defined polarization selection rules, which agree with what have been discussed about the selection rules in the presence of HLHM in Chapter 2.

The evolution of the trion states as a function of the magnetic field is illustrated with the fan diagram in Fig. 5.6(d). The trion states start with a single peak at zero magnetic field and split into four lines at finite magnetic fields. The energy difference between transitions V1 and H1 (H2) corresponds to the hole (electron) Zeeman splitting. The electron and hole Zeeman splitting are plotted in Fig. 5.6(e) as a function of the applied magnetic fields. The linear fittings yield values for $|g_{e\perp}|$ and $|g_{h\perp}|$ of 0.48 and 0.31, respectively. Although the absolute signs of $|g_{e\perp}|$ and $|g_{h\perp}|$ are not identified experimentally, we are able to tell that $|g_{e\perp}|$ and $|g_{h\perp}|$ have the same sign.

In region II of Fig. 5.6(a), spin relaxation is inhibited. When the laser beam is resonant with transition V1, as shown in Fig. 5.6(a), the electron spin in the $|x+\rangle$ state will be excited to the trion state $|t+\rangle$ and then relax equally to the two spin ground states as suggested by the comparable absorption strengths and linewidths. That is to say, because the spin flip resonant Raman scattering process is now allowed in the Voigt profile, the optical induced spin flip process is dramatically "sped up", ensuring a fast spin cooling. Since the electron spin in the ground state has a much slower relaxation rate than the trion spontaneous decay rate, the electron spin will be optically pumped into the $|x-\rangle$ spin state within a few radiative cycles. The signature of optical pumping is that transition V1 becomes transparent to the laser beam. The preparation of $|x+\rangle$ works in a similar way. This is clearly demonstrated in bias range II of Fig. 5.6(a). When the laser is on resonance with V1(V2), the absorption is strongly suppressed and the transition becomes transparent. Thus, the polarized spin states can be selectively prepared in either the $|x-\rangle$ or $|x+\rangle$ spin state.

The mechanism of the spin state preparation can also be explained in terms of saturation spectroscopy, as we discussed in the previous section. The rate equation calculation for a three level lambda system gives the saturation intensity for a trion transition as $I_{SAT} \simeq I_{SAT_o} \times \frac{\Gamma_s}{\Gamma}$, where I_{SAT_o} is the trion saturation intensity at zero magnetic field, Γ_s is the spin relaxation rate, and Γ is the trion spontaneous decay rate. The spin relaxation time $\frac{1}{\Gamma_s}$ has been reported to be on the order of tens of milliseconds [3]. It is much longer than the trion decay time $\frac{1}{\Gamma}$, which is about a few hundred picoseconds [22]. Therefore, in the presence of the transverse magnetic fields, the saturation intensity I_{SAT} of the trion system could be about 6 to 7 orders of magnitude weaker than I_{SAT_o}. Thus, the trion transition is easily saturated and becomes transparent to the optical beam.

The data in the transition region from I to II in Fig. 5.6(a) shows the signature of a bias dependent electron g factor, which leads to transitions H1 and H2 evolving from two well-resolved lines in region I into a central absorption peak in region II. Since transitions H1 and H2 are nearly degenerate in region II, when the laser is on resonance with transition H1, it is also nearly resonant with H2. Therefore, the optical pumping effect is partially canceled by the bi-directional pumping induced by the same optical field. Hence, the optical pumping effect is suppressed and results in the central absorption peak. The origin of this behavior remains under investigation, but it is likely that the strong bias dependence is more complex than the bias dependent g-factors reported earlier in quantum wells [25] and for holes in QDs [26]. Fortunately, the behavior does not impact the main conclusion of the work.

In order to prove that the laser beam leads to nearly complete spin polarization and prepares the spin state as $|x-\rangle$ ($|x+\rangle$) by pumping transition V1 (V2), a polarization inversion beam (PIB) is tuned to be on resonance with transition V2 (V1). As shown in Fig. 5.7(a,b), while the PIB is tuned to be on resonance with transition V1, it repolarizes the spin ground states prepared by pumping transition V2 (i.e. redistributes the population between the spin ground states). This leads to the recovery of the absorption peaks at transitions V2 and H2. Fig. 5.7(c) and (d) show that transitions V1 and H1 can also be recovered by tuning the PIB to be on resonance with transition V2. Considering that the spin cooling process prepares a low-entropy polarized spin state, depending on the intensity of the PIB, the effect of the PIB is to increase the entropy of the system by generating a mixed spin ground state at low intensity or to reverse the spin polarization at high intensity.

The excited state decay rate is 2π times the absorption linewidth in the absence of pure dephasing or spectral wandering. Nearly degenerate differential transmission (NDT) is particularly sensitive to these latter two effects [27,28]. We have performed NDT on the trion state (data shown in the next section), and while the data are complicated by the effect of the Fano interference, they show no evidence of either significant pure dephasing or spectral wandering.

The optical pumping rate is analyzed by the method described in the theory section [21]. Using the lineshape data in Fig. 5.7, a linewidth of order 1.2 GHz (1.5 GHz) is extracted. In the absence of pure dephasing or spectral wandering, corresponds to Γ_{t+x+} (Γ_{t+x-}) of $7.5 \times 10^9 s^{-1}$ ($9.4 \times 10^9 s^{-1}$). In the spin state preparation experiment, the Rabi frequency of the pump beam approximately equals Γ_{t+x+}. Thus, by inserting $b = 1.25$ and $r = 1$ into Eqn 5.7, we infer an optical pumping rate of order $4 \times 10^9\ s^{-1}$. The optical pumping rate inferred from the measured linewidth may be an upper limit if the linewidth is broadened by the spectral diffusion process [24]. The hole coupling to the continuum states might also result in uncertainty in the radiative lifetime (at most a factor of 3). Even including this uncertainty, the optical pumping speed is increased by a few orders of magnitude due to the magnetic field induced state mixing. Using a more conservative trion relaxation rate of $1 \times 10^9\ s^{-1}$ reported by Ref [31], our scheme infers an spin state initialization rate of order $5 \times 10^8\ s^{-1}$.

Figure 5.7(f) simulates the population evolution of spin state $|x-\rangle$ when the laser is on resonance with transition V1. Since the electron spin Zeeman splitting is about $24\ \mu eV$ at 0.88T, which is much smaller than the thermal coupling energy at $5\ K$, the

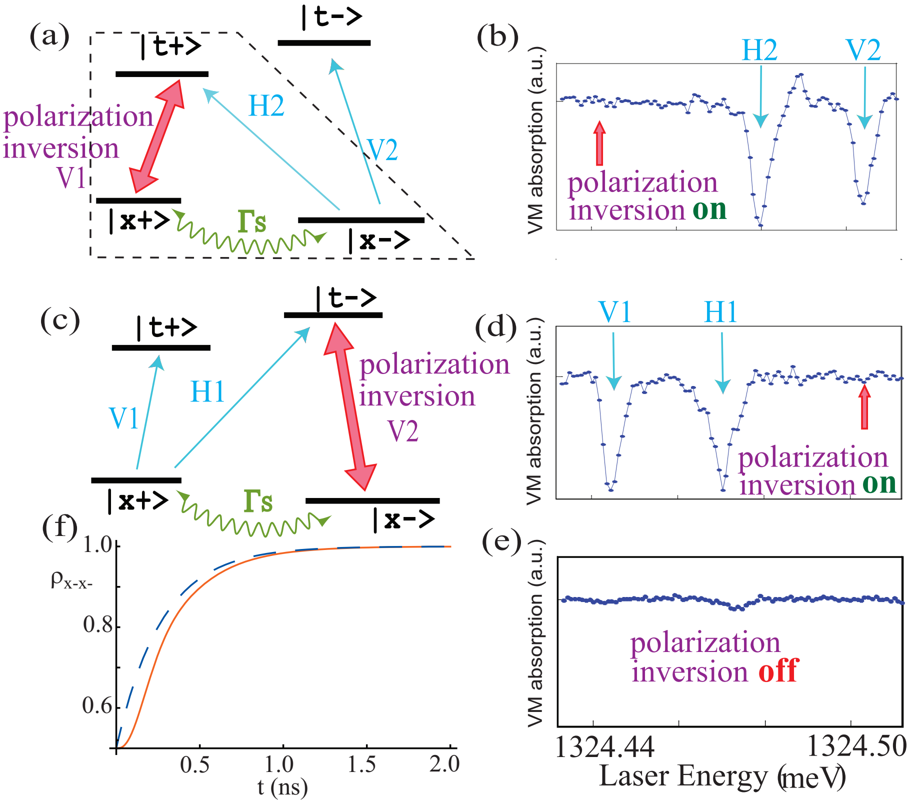

Figure 5.7: Confirmation of Optical Pumping Effect. Demonstration of the spin state preparation in |x+> (|x->) state at magnetic field 1.32 T and gate voltage 0.12 V. The scanning laser is 45^o polarized and the PIB is vertically polarized. (a) and (b) ((c) and (d)) The PIB is resonant with the transition V1 (V2) while probing the transitions H2 and V2 (H1 and V1). (e) One beam absorption spectrum of the trion state in the absence of the PIB. The absorption of transitions V1 and V2 are strongly suppressed due to the optical pumping effect. Since the degeneracy of transitions H1 and H2 are lifted by increasing the magnetic field to 1.32 T, the central peak is also suppressed. f The evolution of the population in $|X-\rangle$ state under the optical pumping condition. Dashed (solid) line is the analytical (numerical) result.

initial spin population for the simulation is taken to be equally distributed between the spin ground states. The parameters for the simulation are extracted from the experimental data. The simulation shows that the state preparation efficiency is near unity when the evolution time is about 2 ns.

The Voigt profile introduces a limitation to the optical pumping efficiency [21]. As we discussed in the theoretical section, this arises from the fact that transitions V1 and V2 have the same polarization selection rules. When the laser is resonant with transition V1(V2), transition V2(V1) will be off-resonantly coupled, which causes a small amount of the spin population to be pumped back. As mentioned above, this type of off-resonant coupling is responsible for the central absorption peak in Fig. 5(a). At a magnetic field of 0.88T, a spin state preparation efficiency of (98.9±0.4)% is achieved experimentally, where the error comes from the measurement noise. Assuming the spin state is prepared in $|x-\rangle$ state, the preparation efficiency is defined as $1 - \rho_{x+x+}/(\rho_{x+x+} + \rho_{x-x-})$. The spin temperature can be calculated by assuming Maxwell-Boltzmann distribution, which corresponds to a spin temperature of 0.06 K [2, 29]. This demonstrates laser cooling of an electron spin from 5 K (the experimental temperature) to 0.06 K in a singly-charged QD. To reach the same efficiency at 5K by thermal equilibration, the applied magnetic field would need to be 69 T and the initialization would be much slower.

5.4 Nonlinear Differential Transmission Measurement of the Optical Pumping Effect

In the previous discussion, the optical pumping was confirmed by recovering of the absorption with a depolarizing beam. In this section, we are going to show a direct proof that the recovered spin population comes from the other spin state by nonlinear differential transmission (NDT) technique [30]. As shown in Fig. 5.8(a), the idea is that the pump and probe beams are chopped at ω_1 and ω_2, respectively, and the nonlinear signal are homodyne detected at frequency $|\omega_1 - \omega_2|$ by a phase sensitive lock-in amplifier.

The pump and probe beams can be frequency degenerate or non-degenerate [27]. Figure 5.8(b) shows the degenerate NDT spectrum of the trion state at zero magnetic field. Due to the Fano effect, as we discussed in the earlier section of this chapter, the spectrum has a differential lineshape instead of Lorentizan lineshape. The line on top the data is a guide to the eye. For comparison, the inset is an absorption spectrum taken by the VM modulation technique, which shows the typical absorption lineshape in the presence of the Fano effect. We also checked the non-degenerated NDT signal. Two examples are plotted in Fig. 5.8(c,d) with different pump detunings. The arrows indicate the pump position and the data are shifted for clarification. A positive signal means reduced absorption of the probe beam induced by the presence of the pump beam. For comparison, the theoretical plots with (bottom inset) and without (top inset) pure dephasing are shown in Fig. 5.8(c,d). Although the lineshape is distorted by the Fano effect, the data clearly shows that there is no "Prussian helmet" profile [27], which confirms that there is no significant pure dephasing process in the QDs [20]. This single charged QD behaves as a homogeneously broadened system. This supports our previous assumption for calculating the optical pumping speed of the charged QD system.

With the magnetic field turned on to 1.32T, a pump beam is set to be on resonance with transition V2, as shown in Fig. 5.9(a). The spin population is transferred from the $|X-\rangle$ to the $|X+\rangle$ state with an amplitude modulation at a frequency of ω_1, which is probed by a weak probe beam at transition V1. Since only the signal with frequency components $|\omega_1 - \omega_2|$ will be picked up by the lock-in, this guarantees two points: (i) the spin population in the $|X+\rangle$ state is indeed from $|X-\rangle$ state; (ii) the probe beam does read out the target spin state $|X+\rangle$. In the other words, the NDT experiment demonstrates the writing and reading process of an initial quantum state, which is very important for QIQC. We have to point out that since the spin in the $|x+\rangle$ state will be driven by the probe beam to the trion state and will then relax to the $|x-\rangle$ state through trion spontaneous emission, the reading efficiency is low in our scheme.

Figure 5.9(a,b) displays the data from pumping on resonance with transition V2

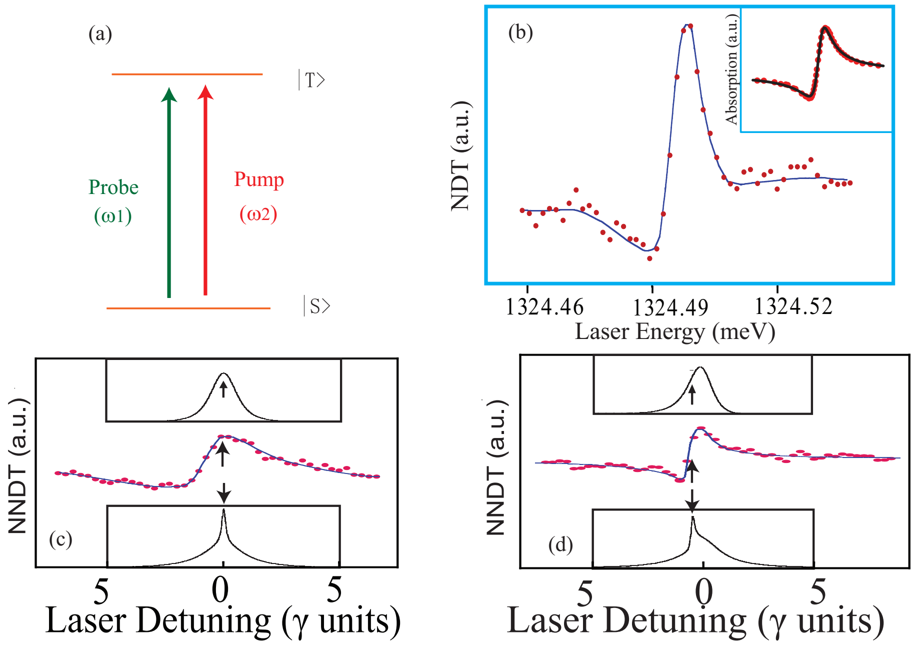

Figure 5.8: NDT Spectrum in the Absence of Magnetic Fields. Plots of coherent NDT signal of a single charged QD at zero magnetic field. (a) Pump and probe beams on a two level transition. (b) The degenerated NDT signal. Inset: an absorption spectrum. (c) and (d) show the non-degenerated NDT spectra. Arrows indicates the pumping position. Lines are guides to the eye. Inset: top (bottom) curve is the calculated spectrum without (with) pure dephasing.

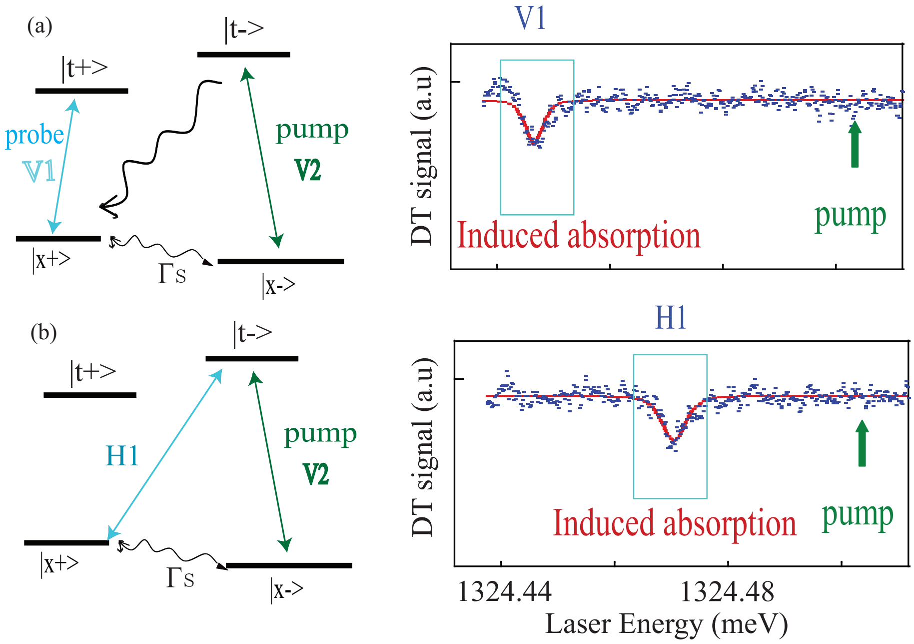

Figure 5.9: NDT Spectrum of a Trion State in The Presence of a Magnetic Field. (a) and (b) display the NDT signal at 1.32 T magnetic fields. With the pump beam on resonant with V2 transition, induced absorption signal is observed while probing the transition V1 and H1. The lines are lorentzian square fits.

and probing the $|X+\rangle$ state. The negative signal means the induced absorption of the probe beam, which is due to the increased spin population at $|X+\rangle$ by the pump beam moving the electron spin from $|X-\rangle$. Transition V1 and H1 can be selectively probed by the polarization selection rules. The Lorentzian square fits yield a trion transition linewidth of 1.6 GHz and 2.1 GHz for the transition V1 and H1, respectively. Although the numbers here are a little bit larger than the ones from the VM absorption spectrum, the ratio between V1 and H1 is about 1.3, which is similar with the absorption measurement.

5.5 Chapter 5 Summary

In this chapter, the fast spin state preparation was demonstrated by a optical pumping technique. The heavy and light hole mixing effect was characterized. The Fano interference effect was observed in this charged QD, which can be controlled by the applied bias and laser power. The NDT experiment was performed on a singly charged QD and the homodyne detected four-wave mixing signal was detected either with and without a magnetic field.

References

[1] D. Loss and D. P. DiVincenzo, Phys. Rev. A **57**, 120 (1998).

[2] Mete Atature *et al.*, Science **312**, 551 (2006).

[3] Miro Kroutvar *et al.*, Nature **432**, 81 (2004).

[4] A. S. Bracker *et al.*, Phys. Rev. Lett. **94**, 047402 (2005).

[5] J. G. Tischler *et al.*, Phys. Rev. B **66**, 081310(R) (2002).

[6] A. Greilich *et al.*, Science **313**, 341 (2006).

[7] D. P. DiVincenzo, Fortschr. Phys. **48**, 771 (2000).

[8] J. Preskill, Proc. R. Soc. Lond. A **454**, 385 (1998).

[9] This is calculated by the numbers provided in Ref [2].

[10] A. V. Koudinov *et al.*, Phys. Rev. B **70**, 241305(R) (2004).

[11] E. L. Ivchenko and A. Yu. Kaminski, U. Rossler, Phys. Rev. B. **54**, 5852 (1996).

[12] D.N. Krizhanovskii et al, Phys. Rev. B 72, 161312 (2005)

[13] Y. Leger, L. Besombes, L. Maingault and H. Mariette, Phys. Rev. B 76, 045331 (2007).

[14] U. Fano, Phys. Rev. **124**, 1866 (1961).

[15] R. P. Madden, K. Codling, Phys. Rev. Lett. **10**, 516 (1963).

[16] H. Schmidt, K. L. Campman, A. C. Gossard, A. Imamoglu, Appl. Phys. Lett. **70**, 3455 (1997).

[17] M. Kroner *et al.*, Nature **415**, 311 (2008).

[18] A. C. Johnson, C.M. Marcus, M. P. Hanson, and A.C. Gossard, Phys. Rev. Lett. **93**, 106803 (2004).

[19] S. Seidl *et al.*, Phys. Rev. B. **72**, 195339 (2005).

[20] P. Meystre, M. Sargent, Elements of Quantum Optics (Springer-Verlag, Heidelberg, 1998), chap. 9, [Third Edition].

[21] C. Emary *et al.*, Phys. Rev. Lett. **98**, 047401 (2007).

[22] J. M. Smith *et al.*, Phys. Rev. Lett. **94**, 197402 (2005).

[23] M. V. G. Dutt *et al.*, Phys. Rev. Lett. **94**, 227403 (2005).

[24] A. Hogele *et al.*, Phys. Rev. Lett. 93, 217401 (2004).

[25] G. Salis *et al.*, Nature **414**, 619 (2001).

[26] M. F. Doty *et al.*, Phys. Rev. Lett. **97**, 197202(2006).

[27] N. H. Bonadeo *et al.*, Phys. Rev. Lett. **81**, 2759 (1998).

[28] H. Wang *et al.*, Phys. Rev. Lett. **65**, 1255 (1990).

[29] A. Hogele *et al.*, Appl. Phys. Lett. **86**, 221905 (2005).

[30] J. Shah, Ultrafast Processes in Semiconductors and Semiconductor Nanostructures (Springer, Berlin, 1996).

[31] W. Langbein *et al.*, Phys. Rev. B **70**, 033301 (2004).

CHAPTER 6

Coherent Population Trapping of an Electron Spin in a Single Quantum Dot

When two radiation fields drive coupled transitions in a three-level lambda system, a steady-state coherent superposition of the ground states can be formed that is totally decoupled from the applied fields, a process that is referred to as coherent population trapping (CPT) [1]. Recently, CPT has been observed in an ensemble of donor bound spins in GaAs [2] and in single nitrogen vacancy centers in diamond [3] by using a fluorescence technique. A critical condition for realizing CPT is to have a pair of stable ground states with a relatively long coherence time compared to the excited state decay time. An electron spin trapped inside a single QD is a system that meets this requirement and constitutes an excellent opportunity for the realization of CPT. The demonstration of CPT shows the existence of the dark state which is important for various physical phenomena, such as electromagnetically induced transparency (EIT) [7, 8] and slow light [9]. The dark state also has applications in quantum information storage [10] and quantum repeaters [11, 12].

On the path towards all optical driven quantum computation, we need to have the ability to manipulate an electron spin and to generate and control the electron spin coherence [13]. In the time domain, evidence of spin manipulation includes the demonstration of spin Rabi oscillations [11, 12], which has not been achieved by optical methods. The coherence between the spin ground states can be generated by a pair of Raman pulses and manifests itself as quantum beats [4–6, 22]. In the frequency domain, electron spin coherence can also be generated by means of coherent population trapping (CPT) [1].

Another critical element for quantum information science is the initial quantum state preparation [14]. We have demonstrated an electron spin state initialization in Chapter 5. However, the limitation is that only two possible initial qubit states can be prepared, either spin up or spin down. CPT is a process that generates an arbitrary coherent superposition of electron spin ground states, whose probability amplitudes can be controlled by varying the ratio of Rabi frequencies between the driving and probe optical fields. Therefore, we can prepare an arbitrary initial qubit state by using the CPT technique. In this scheme, the initialization rate is limited by the excited state decay rate. In this particular system, the initialization rate is on the order of $10^9 s^{-1}$ [15].

In the following, we first gain insight about CPT and derive the formula for the probe absorption under the CPT condition. The experimental results are presented afterwards.

6.1 Theoretical Calculation of CPT

The schematic of a three-level lambda system is shown in Fig. 7.1(a), where Γ_{ij} (γ_{ij}) is the trion population decay (dipole dephasing) rate, Γ_s (γ_s) is the electron spin relaxation (decoherence) rate, $\Omega_i = \frac{\mu_i \times E_i}{\hbar}$ is the Rabi frequency, μ_i is the transition dipole moment, and E_i is the optical field strength. For simplicity, we assume Γ_s, $\gamma_s \ll \Gamma_{ij}$, γ_{ij}, Ω_i. The strong pump beam is nearly resonant with the transition from the $|X-\rangle$ to the $|T-\rangle$ state and a weak probe scans across the transition from the $|X+\rangle$ to the $|T-\rangle$ state. The Hamiltonian of the system is written as

$$H = \hbar \begin{pmatrix} -\omega_{21} & X_{12}e^{i\omega_1 t} & 0 \\ X_{21}e^{-i\omega_1 t} & 0 & X_{23}e^{-i\omega_2 t} \\ 0 & X_{32}e^{i\omega_2 t} & -\omega_{23} \end{pmatrix}, \tag{6.1}$$

where $X_{12} = X_{21} = X_1 = \Omega_1/2$ and $X_{23} = X_{32} = X_2 = \Omega_2/2$. The rotating wave approximation is used to abtain the above Hamiltonian.

In order to get some insight into the generation of the dark state, all decay pa-

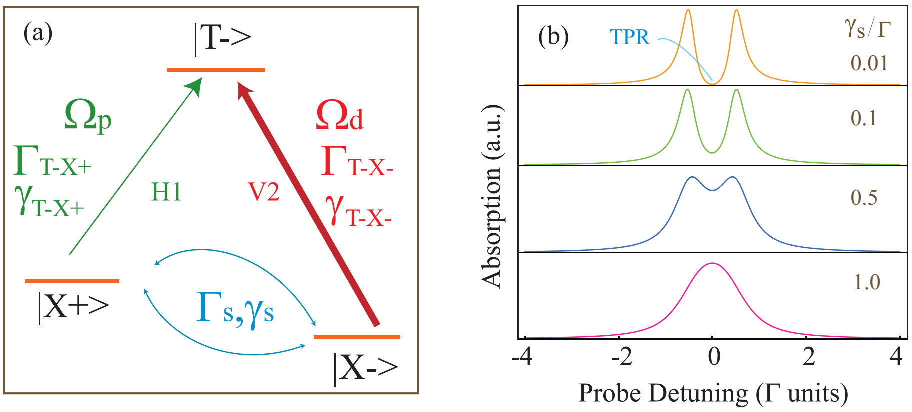

Figure 6.1: Theoretical Plots of CPT Effect. (a) The energy level diagram of a three level Lambda system. A strong pump is on resonance with transition V2 and a weak beam probes transition H1. (d) The theoretical plots of the probe absorption spectrum as a function of the ground state decoherence rate. The CPT is generated when two lasers match the two-photon Raman resonance condition (TPR).

rameters are ignored first. A vector

$$\vec{V} = (C_1, C_2, C_3)' \tag{6.2}$$

is used to describe the system, where C_i is the state amplitude. In this vector model, the system can be written as

$$|\psi\rangle = C_1|1\rangle + C_2|2\rangle + C_3|3\rangle. \tag{6.3}$$

From $-i\hbar\vec{V}/dt = H.\vec{V}$, the time dependent equations for the amplitudes are

$$\dot{C}_1 = -i\left(C_2 e^{i\omega_1 t} X_1 - C_1\omega_{21}\right) \tag{6.4}$$

$$\dot{C}_2 = -i\left(C_1 e^{-i\omega_1 t} X_1 + C_3 e^{i\omega_2 t} X_2\right) \tag{6.5}$$

$$\dot{C}_3 = -i\left(C_2 e^{-i\omega_1 t} X_2 - C_3\omega_{23}\right) \tag{6.6}$$

.

It's convenient to write the amplitude C_i in the field interaction picture. We substitute

$$C_1 = \widetilde{C}_1 e^{i\omega_1 t},\ C_2 = \widetilde{C}_2,\ C_3 = \widetilde{C}_3 e^{i\omega_3 t} \tag{6.7}$$

into the above equation and obtain

$$\begin{aligned}
\dot{\widetilde{C}}_1 &= -i\left(\widetilde{C}_2 X_1 + \widetilde{C}_1 \delta_1\right) && (6.8)\\
\dot{\widetilde{C}}_2 &= -i\left(\widetilde{C}_1 X_1 + \widetilde{C}_3 X_2\right) && (6.9)\\
\dot{\widetilde{C}}_3 &= -i\left(\widetilde{C}_2 X_2 + \widetilde{C}_3 \delta_2\right) && (6.10)
\end{aligned}$$

The above equations lead to

$$X_2\dot{\widetilde{C}}_1 - X_1\dot{\widetilde{C}}_3 = -i(X_2\widetilde{C}_1\delta_1 - X_1\widetilde{C}_3\delta_2) \tag{6.11}$$

Under the condition of $\delta_1 = \delta_2 = \delta$, then equation 6.11 can be simplified to

$$X_2\dot{\widetilde{C}}_1 - X_1\dot{\widetilde{C}}_3 = -i(X_2\widetilde{C}_1 - X_1\widetilde{C}_3)\delta \tag{6.12}$$

A new state $|D\rangle = X_2|1\rangle - X_1|3\rangle$ is defined with an amplitude of $D = X_2\widetilde{C}_1 - X_1\widetilde{C}_3$. Equation 6.12 can be rewritten as

$$\dot{D} = -iD\delta. \tag{6.13}$$

It is clear that state $|D\rangle$ is not excited by the optical fields, and is therefore known as the dark state. If there is no relaxation of the ground states, then this dark state is the steady state for the three level Lambda system. From the quantum computing point of view, the dark state is an initialized qubit state. The probability amplitudes of the ground states in this superposition state can be controlled by varying the ratio of the pump and probe Rabi frequencies.

In the following, this system is considered in the presence of relaxation. The analytical formula for the probe absorption can be derived by solving the optical Bloch equations. The general form is unwieldy, however, a relatively simple form can be achieved in the weak probe field limit. By solving the optical Bloch equations to the lowest order of the probe beam with the approximation $\Gamma_s = 0$, the formula for the probe beam absorption is

$$\alpha_{T-X+} = \frac{\gamma_{T-X+}\left(X_2^2\gamma_s + \gamma_{T-X+}\left(\gamma_s^2 + (\delta_1-\delta_2)^2\right)\right)}{X_2^4 + \left(\gamma_{T-X+}^2 + \delta_1^2\right)\left(\gamma_s^2 + (\delta_1-\delta_2)^2\right) + 2X_2^2\left(\gamma_{21}\gamma_s + \delta_1\left(-\delta_1+\delta_2\right)\right)} \tag{6.14}$$

Under the condition of two-photon Raman resonance, i.e $\delta_1 = \delta_2$, equation 6.14 is simplified to

$$\alpha_{T-X+} = \frac{\gamma_{T-X+}\left(X_2^2\gamma_s + \gamma_{T-X+}\gamma_s^2\right)}{X_2^4 + \left(\gamma_{T-X+}^2 + \delta_1^2\right)\gamma_s^2 + 2X_2^2\gamma_{21}\gamma_s} \tag{6.15}$$

It is shown that the strength of the probe beam absorption is proportional to the ground state decoherence rate γ_s. If there is no decoherence between the ground states, then the transition is transparent to the probe beam, i.e there is no absorption for the probe beam. The generation of the dark state is the central physics behind EIT. Figure 7.1(b) shows the theoretical plots of the probe absorption spectrum by varying the ground state decoherence rate. In this plot, the Rabi frequency of the pump equals the trion decay rate Γ. It clearly shows that under the two-photon Raman resonance condition, the absorption decreases as γ_s decreases. When $\gamma_s = \Gamma$, the dip caused by the CPT disappears.

6.2 Experimental Results Demonstrating CPT

In order to get a clean lineshape, the particular QD used in this experiment is the same as the one discussed in Chapter 4. Figure B.1(a) shows the energy level structure for the lowest lying states of a negatively charged QD at zero magnetic field, as talked about in Chapters 4 and 5. Since the spin flip Raman transitions are dipole forbidden, the trion system at zero magnetic field can be considered as a double two-level structure, not adequate for the realization of CPT.

It has been shown in Chapters 2 and 5 that if a magnetic field is applied in the Voigt geometry ($\overrightarrow{X}$ axis), i.e. perpendicular to the sample growth direction ($\overrightarrow{Z}$ axis), a four level trion system is created, as shown in Fig. B.1(b). The new electron spin eigenstates $|X\pm\rangle$ can be excited to either trion states $|T\pm\rangle$ with linearly polarized light [15]. Hence, the forbidden Raman transitions at zero magnetic field are turned on when the magnetic field is applied along the $\overrightarrow{X}$ axis. As shown by Fig. B.1(b), we choose $|X\pm\rangle$ and $|T-\rangle$ to form a three-level lambda system.

First the QD is characterized with a single beam voltage modulation absorption experiment [15, 18]. The gate voltage is set at the edge of the trion charge plateau,

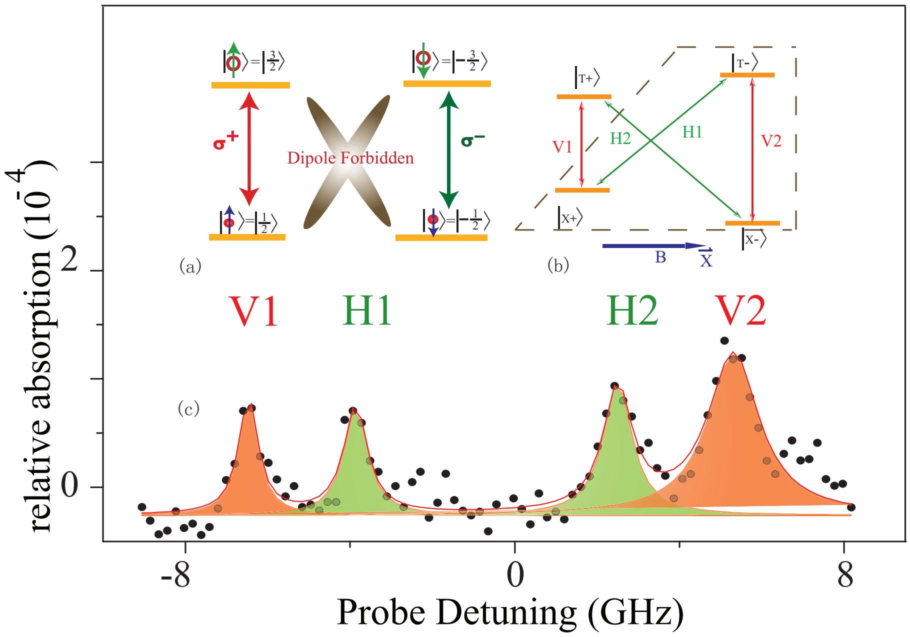

Figure 6.2: Quartet Transition Pattern of A Trion State. Trion energy level diagrams (a) without and (b) with magnetic field applied in the Voigt geometry. V (H) means the transition is vertically (horizontally) polarized. At zero magnetic field, the spin flip Raman transitions are dipole forbidden. By applying a magnetic field in the Voigt geometry, the dark transitions become bright. A three-level lambda system is formed by these levels enclosed in the dashed line box. (c) Single beam absorption spectrum of the trion state at a magnetic field of 1.32 T with 45° linearly polarized light excitation. A quartet transition patterned is observed as the gate voltage is set in the non optical pumping region.

where the optical pumping of the electron spin effect is suppressed [15, 16]. Figure B.1(c) shows the quartet transition pattern of the trion state using 45° linearly polarized light to excite the transitions at a magnetic field of 1.32T. The observation of the four transition lines confirms that all four trion transitions are turned on and have similar transition strengths [15]. The four transitions are labeled as $V1$, $H1$, $H2$, and $V2$. The energy difference between $V2$ and $H1(H2)$ is the electron (hole) spin Zeeman splitting. The Zeeman splitting as a function of the magnetic field has been studied and yields the electron and hole in plane g factors of 0.49 and 0.13, respectively, which are similar to the g factors measured for the other trion state in Chapter 5.

The gate voltage is then set to where the co-tunneling induced spin flip process is suppressed [28]. Figure 3(a) shows a single beam absorption spectrum by scanning the laser across transition H1 at a magnetic field of 2.64 T. An almost flat line is observed for the probe absorption spectrum reflecting the absence of the absorption due to optical pumping [15, 16]. The optical pumping induced saturation of the absorption shows that the spin relaxation rate is much slower than the trion relaxation rate. Hence, the spin ground states can be considered as meta-stable states compared to the short lived trion states.

To understand the experimental conditions for the measurements, we consider the interaction scheme shown in Fig. 7.1(a). A strong optical field (the driving field) is tuned on resonance with transition $V2$ and a weak optical field (the probe) is scanned across transition $H1$. When the probe laser is resonant with transition $H1$, the two-photon Raman resonance condition is reached. As seen in Fig. 7.3(g), a clear dip in the probe absorption spectrum is observed for $\Omega_d/2\pi = 0.83$ GHz. This observation demonstrates both the generation of CPT of an electron spin and the Raman coherence between the spin ground states. For this particular set of data, the applied magnetic field is 2.64 T, corresponding to an electron Zeeman splitting of 75.4 μeV (18.2 GHz).

The observation of CPT can be understood from the point of view of optical pumping. When the driving and probe lasers are on the two-photon Raman resonance, a coherent dark state is created that is decoupled from the applied optical fields and can be represented as $|\mathrm{D}\rangle = \frac{\Omega_\mathrm{d}|\mathrm{X}+\rangle - \Omega_\mathrm{p}|\mathrm{X}-\rangle}{\sqrt{\Omega_\mathrm{d}^2+\Omega_\mathrm{p}^2}}$. Part of the population is excited from the electron spin ground state to the trion state and relaxes spontaneously into the dark state. Since the dark state is not "seen" by the optical fields, the total population is eventually trapped there within a few radiative cycles of the trion state. In CPT, the coherence between the spin ground states is created by the coherent optical fields. Therefore, the whole process is an optical pumping process, whose rate is ultimately limited by the excited state decay rate, with the transfer of the mutual coherence between the optical fields to the electron spin coherence.

An arbitrary initial state for the quantum computation can be prepared by varying the ratio of the Rabi frequencies between the driving and probe fields. Ultimately, if Ω_d is set to be zero, the initialized spin state will be $|X-\rangle$. This is the fast spin state preparation effect as discussed in Chapter 5 and Ref [15]. The difference is that when Ω_d is zero, there is no coherence involved in the state initialization and the preparation efficiency is determined by the electron spin relaxation rate. In the initialization of the arbitrary coherent superposition state, we generate an electron spin coherence by the optical fields, and the state preparation efficiency is limited by the electron spin decoherence rate.

The linewidth of the dip in the probe absorption spectrum is ultimately limited by the electron spin decoherence rate. In the experiment, the smallest Ω_d applied is 0.56 GHz, which is about half of the trion transition linewidth, but still much larger than γ_s. Hence, the linewidth of the dip is broadened by the laser power. When Ω_d is strong, it will dress the spin ground state $|X-\rangle$ and the trion state $|T-\rangle$. In the case where Ω_d is larger than the trion transition linewidth, the absorption spectrum of the probe beam will split into two peaks when scanning across transition $H1$, which are known as Autler-Townes (AT) doublets [29], and has been demonstrated in a neutral QD [23, 30]. The spectral features of the probe absorption spectrum in our experiment are a combination of the AT splitting and the CPT quantum interference effect [7], where the spectral positions of the side bands can be determined by the AT splitting and the central feature in the absorption spectrum is due to the CPT effect,

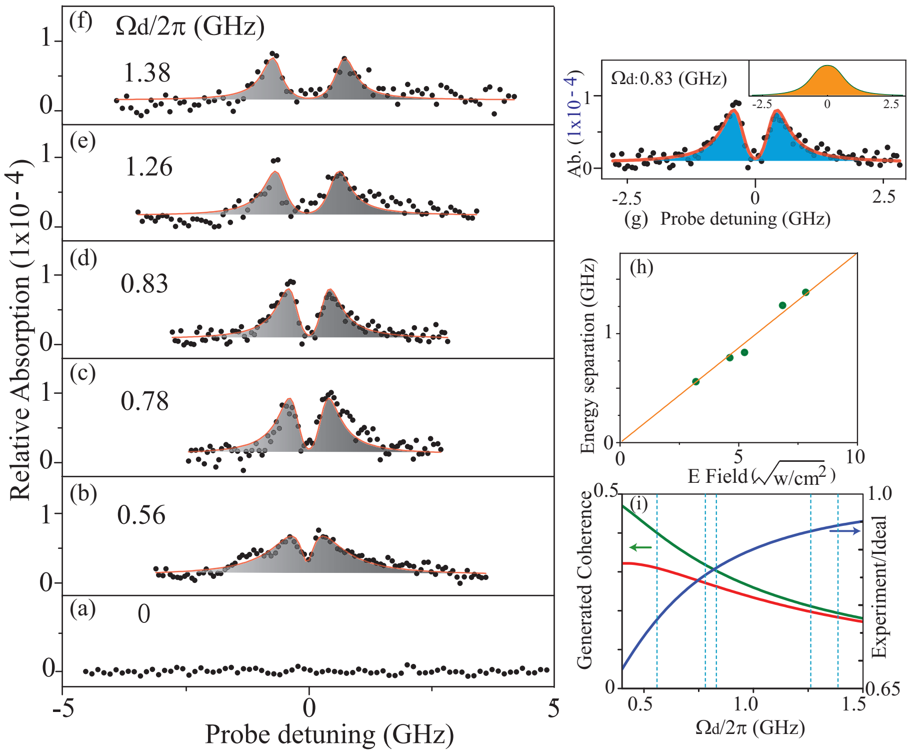

Figure 6.3: Demonstration of CPT. The experimental evidence of the CPT of an electron spin The gate voltage is set in the optical pumping region and the applied magnetic field is 2.64 T. (a) The probe absorption spectrum across transition H1 in the absence of the driving field. (b-f) Probe absorption spectra with various driving field Rabi frequencies. The driving field is set to be resonant with the transition from $|X-\rangle$ to $|T-\rangle$. The red solid lines are the theoretical fits by solving the optical Bloch equations. A pronounced dip is observed in the probe absorption due to generation of the dark state. (g) An example of the probe absorption spectrum and shows the generation of the CPT. The inset is a theoretical plot with large electron spin decoherence rate, which does not show the dip in the spectrum. (h) The energy separation of the AT doublets as a function of driving field strength. (b) Theoretical curves of the creation of the electron spin coherence in a single charged quantum dot. Red line: experimentally generated electron spin Raman coherence ρ_{X+X-} inferred from the optical Bloch equations calculation by using the experimental parameters. The calculation is done under the experimental condition that the driving and probe fields are resonant with transition V2 and H1, respectively. Green line: the calculated maximum electron spin Raman coherence in the absence of the electron spin dephasing. Blue line: the ratio of the experimentally generated coherence to the ideal case.

not a simple summation of the tails of the AT Lorentzian lineshapes.

The probe absorption spectra with various driving field strengths and fixed probe Rabi frequencies are illustrated in Fig. 7.3(b-f). The energy separation of the two peaks is increased by increasing the driving field intensity. As Ω_d becomes larger than the trion transition linewidth, two AT peaks with Lorentzian lineshapes appear in the probe absorption spectrum, as shown by Fig. 7.3(e, f). Figure 7.3(h) displays the energy separation of the AT splitting peaks as a function of the driving field strength. A linear regression fits the data and extends to zero in the absence of the driving field, which indicates that the splitting is dominated by Ω_d. The red solid lines on top of the data shown in Fig. 2(b-f) are the theoretical fits obtained by solving the optical Bloch equations to all orders in the driving field and to first order in the probe. Assuming that γ_s is a few orders of magnitude larger than Γ_s (as we show below), $\gamma_{T-X+}/2\pi$, and $\gamma_s/2\pi$ are found to be $(0.54 \pm 0.1)GHz$, and $(40 \pm 12)MHz$, respectively. The value of $40MHz$ corresponds to the electron spin decoherence time T_2^* $(1/\gamma_s)$ of $4\,ns$. Although an electron spin trapped inside a single QD is studied, the electron spin T_2^* extracted from the data is not the intrinsic electron spin decoherence time due to the hyperfine interaction between the electron spin and the neighboring nuclear ensemble [26, 27, 32, 34, 35]. The intrinsic T2 can be measured by spin echo techniques [11] or mode locking of the spin coherence [5]. The hyperfine interaction between an electron spin and the lattice nuclei will be discussed in detail in the next chapter.

The generation of the dark state is accompanied by the excitation of the electron spin coherence, which corresponds to the density matrix element ρ_{x+x-}. The parameters extracted from the fits are inserted into the optical Bloch equations and obtain the value of the coherence between the spin ground states, which are represented by the red line in Fig. 7.3(i). The green line in Fig. 7.3(i) represents the theoretical values for the coherence in the absence of spin decoherence, given by $\frac{\Omega_d\Omega_p}{\Omega_d^2+\Omega_p^2}$. The blue line represents the ratio of the experimentally generated coherence to the ideal case. The light blue dashed lines indicate the applied Ω_d in the experiment. At the maximally applied Rabi frequency of 1.38 GHz, we infer that 94% of the optimal coherence is generated in our system.

6.3 Chapter 6 Summary

In this chapter, coherent population trapping of a single electron spin in a QD is demonstrated as a dark state dip in the probe absorption spectrum. The generation of the CPT accompanies the creation of the spin ground states coherence. This CPT technique can be a viable technique to achieve arbitrary qubit state initialization. Furthermore, the results presented in this chapter could lead to experiments such as EIT, slow light, and quantum information storage in charged QD systems.

References

[1] H. R. Gray, R. M. Whitley, C. R. Jr. Stroud, Opt. Lett **3**, 218 (1978).

[2] Kai-Mei C. Fu, C. Santori, C. Stanley, M. C. Holland, Y. Yamamoto, Phys. Rev. Lett. **95**, 187405 (2005).

[3] C. Santori,*et. al.* , Phys. Rev. Lett. **97**, 247401 (2006).

[4] S. E. Harris, Phys. Today **50**, 36 (1997).

[5] , K. J. Boller, A. Imamoglu,, S. E. Harris, Phys. Rev. Lett. **66**, 2593 (1991).

[6] L. V. Hau, S. E. Harris, Z. Dutton, C. H. Behroozi, Nature **397**, 594 (1999).

[7] C. Liu, Z. Dutton, C. H. Behroozi, L. V. Hau, Nature **409**, 490 (2001).

[8] L. M. Duan, M. D. Lukin, J. I. Cirac, P. Zoller, Nature **414**, 413 (2001).

[9] H. J. Briegel, W. Duer, J. I. Cirac, P. Zoller, Phys. Rev. Lett. **81**, 5932 (1998).

[10] D. Loss, D. P. DiVincenzo, Phys. Rev. A **57**, 120 (1998).

[11] J. R. Petta et al., Science **309**, 2180 (2005).

[12] F. H. L. Koppens, *et al.* nature **442**, 767 (2006).

[13] M. V. G. Dutt, *et al.*, Phys. Rev. Lett. **94**, 227403 (2005).

[14] A. Greilich *et al.* , Science **313**, 341 (2006).

[15] M. H. Mikkelsen, J. Berezovsky,, G. N. Stoltz, L. A. Coldren, D. D. Awschalom, Nature Physics **3**, 770 (2007).

[16] A. Greilich *et al.*, Science **317**, 1896 2007.

[17] D. P. DiVincenzo, Fortschr. phys. **48**, 771 (2000).

[18] X. Xu *et al.* , Phys. Rev. Lett. **99**, 097401 (2007).

[19] B. Alen *et al.*, Appl. Phys. Lett. **83**, 2235 (2003).

[20] J. M. Smith *et al.*, Phys. Rev. Lett. **94**, 197402 (2005).

[21] M. Atature *et al.*, Science **312**, 551 (2006).

[22] S. H. Autler, C. H. Townes, Phys. Rev. **100**, 703 (1955).

[23] H. Kamada, H. Gotoh, J. Temmyo, T. Takagahara, H. Ando, Phys. Rev. Lett. **87**, 246401 (2001).

[24] X. Xu *et al.*, Science **317**, 929 (2007).

[25] A. V. Khaetskii, D. Loss, L. Glazman, Phys. Rev. Lett. **88**, 186802(2002).

[26] W. A. Coish, D. Loss, Phys. Rev. B **70**, 195340 (2004).

[27] A. C. Johnson *et. al.*, Nature **435**, 925 (2005).

[28] A. S. Bracker *et al.*, Phys. Rev. Lett. **94**, 047402 (2005).

[29] W. Yao, R. B. Liu, L. J. Sham, Phys. Rev. Lett. **98**, 077602 (2007).

CHAPTER 7

Optically Controlled Locking of The Nuclear Field via Coherent Dark State Spectroscopy

A single spin trapped inside a quantum dot (QD) has been playing a central role in quantum computation (QC) and spintronics applications in recent research [1–9]. In these III-V materials, a single spin is coupled to the lattice nuclear spins. The spin resonance and spin coherence are inevitably affected by the hyperfine interaction [5, 10], while the dynamics of the spin can also actively affect the nuclear environment. Understanding and controlling the hyperfine interaction between a single spin and the lattice nuclei in such a system is critical from the point of view of both QC and fundamental physics [6,11–16]. Recent efforts have been made to enhance the electron spin decoherence time (T2*) by suppressing the nuclear spin fluctuations in electronic gate confined double dot systems [14] and in an ensemble of self-assembled QDs [6].

The coherent manipulation of a single spin is essential for all optically driven QC. It is a critical challenge to be able to coherently manipulate a single electron spin while probing and eventually controlling the nuclear spin environment. Coherent population trapping (CPT), which is the central physics behind electromagnetically induced transparency (EIT) [17], is a process to generate coherence between spin ground states of an electron and represents a manipulation of electron spin in the frequency domain. The generation of this coherent dark state requires the satisfaction of a two-photon Raman resonance (TPR) condition, i.e. the energy difference of two CW lasers exactly match the electron spin Zeeman splitting. Because absorption of the probe laser by trion excitation increases abruptly with detuning from the TPR condition, the dark state generated by the CPT process is very sensitive to the effects of the Overhauser field on the TPR and can be used as a direct probe of the nuclear spin environment [18].

This chapter is organized as follows. The basic theory of the hyperfine interaction is discussed first. The experimental results of the dynamical nuclear spin polarization (DNP) effect are then presented. The theoretical explanation of the experimental observations is shown afterwards. The suppression of the nuclear spin fluctuations is discussed at the end of this chapter.

7.1 Basic Concepts of the Hyperfine Interaction of a Spin with Nuclei

In this section, I will give a brief review of the basic concepts of the hyperfine interaction with respect to the QD system. The hyperfine interaction induced electron spin dephasing is also discussed briefly.

The general form of the hyperfine interaction of an electron/hole with nuclei is described as [19]

$$H_f = 2\mu_B\gamma_N\hbar\sum_j \frac{I_j \cdot L}{r^3} + \left(\frac{(3S\cdot\vec{r})\,(I_j\cdot\vec{r}) - S\;r^2}{r^5}\right) + \frac{8}{3}S\cdot I_j\delta\left(r_j\right) \tag{7.1}$$

where μ_B is the Bohr magneton, γ_N is the nuclear spin gyromagnetic ratio, L is the orbital momentum of the electron, I_j is the j_{th} nuclear spin, r_j is the relative position between the electron/hole and the j_{th} nuclear spin, and S is the electron/hole spin. The first term shows the hyperfine interaction from the motion of the electron/hole spin, which is known as the chemical shift and is usually observed in molecules. The second term is the hyperfine interaction from the dipole-dipole interaction. Obviously, there is no dipole-dipole interaction for the S wave function. In QDs, the ground state electron spin has an S like wave function. Hence, the dipole-dipole interaction can be ignored for the electron spin. On the other hand, the hole spin has p like wave function. Thus the hole spin can interact with the nuclear spins through the dipole interaction. The third term is the isotropic Fermi contact hyperfine interaction, which depends on the wave function overlap between the electron/hole spin and nuclear spins. Since the electron spin in the QDs has a S wave function, the hyperfine interaction between the electron spin and nuclear spins is dominated by the Fermi contact interaction, but not for the hole spin because of its P wave function.

The Fermi contact hyperfine interaction term can be rewritten as

$$H = \frac{\nu_o}{2} \sum_j A_j |\Psi(r_j = 0)|^2 (I_z^j S_z + (I_+^j S_- + I_-^j S_+)/2) \tag{7.2}$$

where $I_\pm^j$ ($S_\pm$) are the nuclear (electron) spin raising and lowering operators, A_j is the isotropic hyperfine constant, ν_o is the InAs unit cell containing 8 nuclei, and $\Psi(r_j = 0)$ is the electron wave function at the j_{th} nuclear spin. In the above equation, $I_z^j S_z$ is the static part which affects the energies of the electron spin, known as the Overhauser field, and the nuclei, known as the Knight field. The dynamics of Knight field in a single charged QD has recently been studied [20]. The Overhauser field can be written as [10]

$$B_N = \frac{\nu_o}{8 g_e \mu_B} \sum_j A_j |\Psi(r_j = 0)|^2 I_z^j, \tag{7.3}$$

. If there is no external magnetic field, the nuclear spins are randomly oriented. The average of B_N on a long time scale will be zero. However, since the electrons spin precession much faster in the hyperfine field of nuclear spins than the precession of nuclear spins in the hyperfine field of the electron spin, the electron spin sees a "frozen fluctuation" of nuclear fields B_N [10]. Since the direction and magnitude of B_N randomly distribute, B_N has a dispersion of [10]

$$\Delta_N^2 = \frac{16}{3 N_L (g_e \mu_b)^2} \sum_j I_j (I_j + 1) A_j^2 \tag{7.4}$$

where Δ_N is the dispersion of Overhauser field and N_L is the number of nuclei interacting with the nuclear spin. Δ_N limits the electron spin decoherence time T2* for a time ensemble measurement. The electron spin decoherence rate γ_s (1/T2*) can be calculated given by [10]

$$\gamma_s = \sqrt{\frac{16}{3 \hbar^2 N_L} \sum_j I_j (I_j + 1) A_j^2} \tag{7.5}$$

For GaAs QDs, the hyperfine constant A is about 90 μev and N_L is on the order of 10^6. Equation 7.5 gives an electron spin T2* in GaAs QDs on the order of 10 ns [21,24].

Self-assembled QDs are much smaller QDs than interface fluctuation or gate-confined GaAs QDs. Using the dot studied in this thesis as an example, the QD is 3nm in height and 15 nm in the base diameter [23]. The number of nuclei in a QD is estimated to be 2.5×10^4. Taking $I_{In} = 9/2$, $I_{As} = 3/2$, $A_{in} = 56\mu ev$, and $A_{As} = 47\mu ev$ [24], Eqn. 7.5 gives an electron spin T2* of around 400 ps. The origin of the short T2* in the SAQD is the strong confinement of the electron spin wave function. The Fermi-contact interaction between an electron spin and a nuclear spin is proportional to the electron spin wave function on that particular nuclear spin. Therefore, the strong wave function confinement in the self assembled QD leads to strong hyperfine interaction, which causes the large inhomogeneous broadening of the Overhauser field and short T2*. One would think that a high degree of polarization of nuclear spins would be required for suppressing the nuclear spin fluctuations. However, if we consider a particle inside a three dimensionally confined box, from quantum mechanics, we learn that the ground state (S wave function) has maximum amplitudes in the center of the box and minimum in the edge. Therefore, it is expected that the Fermi-contact hyperfine interaction depends strongly on a small portion of the nuclear spins, which strongly overlap (hyperfine coupling) with the electron spin. This portion of nuclear spin is scaled as $\frac{1}{\sqrt{N_L}}$, which indicates that only less than 1% of the total nuclear spins need to be polarized to suppress the nuclear spin fluctuations [14]. This effect is known as the Zamboni effect [25].

In Eqn 7.2, $(I^j_+ S_- + I^j_- S_+)/2$ is the dynamic part, which corresponds to the momentum transfer between the electron and nuclear spins, i.e a flip of the electron spin associated with a flip of a nuclear spin. The built up nuclear spin polarization through the dynamical process will affect the electron spin Zeeman energy through the Overhauser field. At relatively high magnetic fields, the electron spin Zeeman splitting is a few orders of magnitude larger than the Zeeman splitting of a nuclear spin. The energy conservation could be satisfied by phonons. However, the coupling efficiency with the phonon can be very low, and the dynamic process is usually suppressed at high magnetic fields.

Since the hole spin in the QD has a P type wave function, it does not interact with the nuclear spins through the isotropic Fermi contact hyperfine interaction. It has been taken for granted that there is no significant hyperfine interaction between the hole spin and nuclear spins in the QDs. Therefore, the positively charged QD is proposed for quantum computing applications since the hole spin is expected to immune to the hyperfine interaction. However, there is a fact that the hole spin can interact with nuclear spins through dipolar interaction. Recently, two papers have looked into this problem and have shown the hole spin dephasing mechanism due to the hyperfine interaction [26, 27] in positively charged QDs.

In our experiment, we show that even in a negatively charged QD, the hole spin can dominate the dynamic nuclear spin polarization at high magnetic fields through the dipole-dipole interaction, which arises from the properties of the excited trion state determined by the hole spin. This hole-spin assisted DNP process can lead to the suppression of nuclear spin fluctuations, evident by the enhanced electron spin T2*. In the following, we will present the experimental observation of the hole spin-assisted DNP. The theoretical explanation of the data will be presented afterwards.

7.2 Experimental Results of the Nuclear Self-Focusing Effect

The experiment is performed on a single negatively charged QD embedded in a Schottky diode structure at a temperature of 5 K [28, 29]. We set the bias voltage across the sample to charge only one electron into the QD. By applying an external magnetic field perpendicular to the sample growth direction, we generate a four level trion system, where a three level Lambda system can be selectively isolated, as shown in the dash box of Fig. 7.1(a). $|X\pm\rangle$ ($|T\pm\rangle$) are the electron (hole) spin Zeeman sublevels [29]. Two continuous wave (CW) lasers are used in the pump-probe experiment. As shown in Fig. 7.1(a), a strong pump beam (red arrow) is horizontally polarized and fixed to be nearly resonant with transition H1. The weak probe beam (green arrow) is vertically polarized. Since the polarization axis of the QD rotates about 20^o away from the lab frame due to the heavy and light hole mixing [30], the probe beam can pick up both V2 and H2 transitions in a single scan.

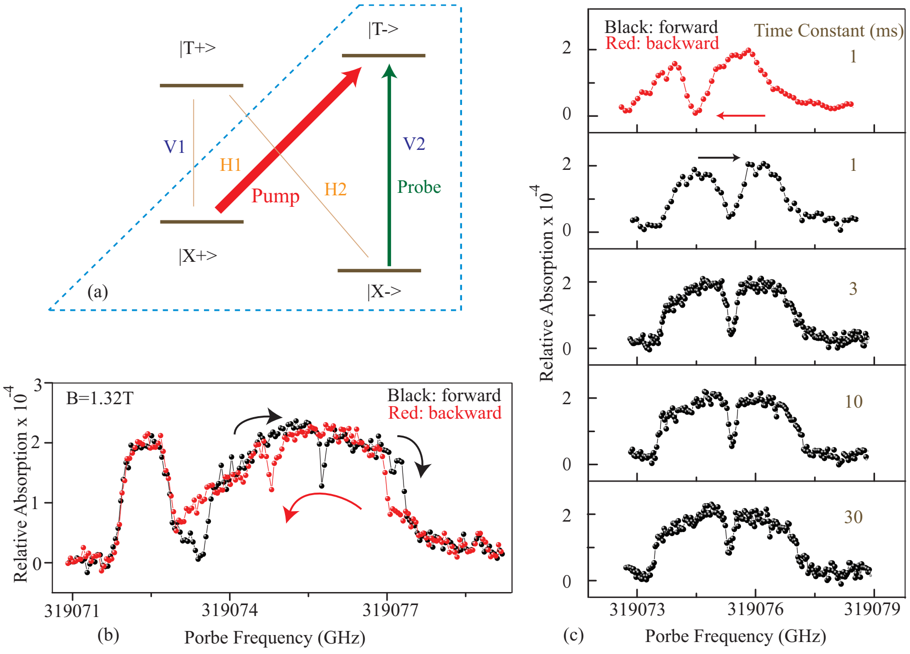

Figure 7.1: The Observation of Hysteresis Effect. (a) The schematic of a trion energy level diagram with a magnetic field applied in the Voigt geometry. Due to the heavy-light hole mixing, the out pair (inner pair) of transitions rotates about 20^o away from the vertical (horizontal) polarization in the lab frame. The dashed box isolates the selected three-level Lambda system. A strong pump beam is near resonant with transition H1 and a weak beam probes transition V2. A dark state is formed when both lasers match the two-photon Raman resonance. (b) The probe absorption spectrum at an external magnetic field 1.32T. The black (red) curve represents the probe absorption spectrum of the forward (backward) scan. (c) The probe absorption spectrum as a function of the laser scan rate, indicated by the Lock-in time constant. The top red curve is the backward scan with a 1 ms Lock-in time constant.

Figure 7.1(b) shows the probe absorption spectrum at a magnetic field of 1.32 T. In this data set, each data point is integrated with a one second lock-in time constant. The narrow peak on the left and the broad peak on the right correspond to transitions H2 and V2, respectively. We define the forward (backward) scan by sweeping the probe laser from low (high) frequency to high (low) frequency. The black (red) curve in Fig. 7.1(b) is the probe absorption spectrum obtained by scanning the laser forward (backward). We focus on the optical response from transition V2, where the sharp dip in the spectrum is due to the generation of the dark state when both lasers match TPR [31].

Ideally, the overall lineshape of transition V2 should be Lorentzian like with a dark state dip, as shown in Fig. 7.3(a). However, the spectrum clearly shows a broadened lineshape with a round top and sharp edges, far from Lorentzian. The width and the strength of the observed dip (the dark state) are also narrower and shallower than what are expected. More remarkably, the spectra of forward and backward scans do not completely overlap. The spectral position of the dark state in the backward scan is shifted from the forward one, which indicates a change of TPR when the scan direction is switched. We also observe hysteresis on the sharp edges of the V2 absorption peak between the forward and backward scans, similar to the hysteresis effect in the DC transport characteristics observed in GaAs heterostructures due to DNP in the quantum Hall regime [32]. As the external magnetic field is unchanged in the forward and backward scans, the above observations indicate that we optically create and probe the DNP in this charged QD system, where the nuclear spin configuration can be controlled by the scan direction of the optical field.

We study the characteristics of the dark state as a function of laser scan rate. As a part of our measurement method, an increase of the laser scan rate is accompanied by a decrease of the lock-in time constant. The data in Fig. 7.1(c) clearly show that the dark state becomes more pronounced concomitant with a broader dip width as we increase the laser scan rate. Under faster scans, the edge hysteresis and the spectrum shift of the dark state also become less pronounced, and the observed lineshape is closer to the standard EIT spectrum in a Lambda level scheme (see Fig.

3A), showing that the anomalous spectral features are due to a dynamic shift of the spectral resonances on a timescale as slow as seconds.

The dynamics of the nuclear spin configuration are further explored by fixing both lasers and recording the optical response as a function of time. The data shown in Fig. B.1 are taken at a magnetic field of 2.64 T. Figure 2A shows the probe absorption spectra with forward (black) and backward (red) scans. We observe a stronger hysteresis effect but a weaker dark state resonance than at 1.32 T, which could be ascribed to a decrease of the relaxation rate of the nuclear spin polarization caused by increasing the magnetic field. For simplicity, we name the two hysteresis states 1 and 2 in Fig. B.1(a).

To show switching between hysteresis states 1 and 2, we first scan the laser backward and stop the laser right before the sharp rising edge of the trion peak, as shown by the green curve in Fig. 2C. We continue to record the absorption signal as a function of time with the laser parked. As seen in Fig. B.1(b), the signal level remains unchanged at first, which means the system stays in hysteresis state 1. After some time, we observe a sharp jump of the signal, up to a signal level consistent with hysteresis state 2, where it remains. This jump is a signature of the switching of the nuclear spin configuration. The time delay between parking the laser and this switching between hysteresis states can be controlled by the laser parking position. If the laser is parked closer to the sharp edge, the switching between the hysteresis states happens faster. However, if the laser is parked far away from the sharp edge, the system will stay in hysteresis state 1 and never jump to hysteresis 2. Finally, we scan the probe laser forward and map out hysteresis state 2. The blue curve in Fig. B.1(d) shows the partial forward scan spectrum which agrees with the full forward scan pretty well.

The dynamics of the nuclear spin are also examined by monitoring the dark state. In the following, we detune the pump to emphasize the dark state. After a full forward scan to locate the dark state position, as shown by the black curve in Fig. 2E, we take a partial forward scan to prepare the initial nuclear spin configuration and stop the laser right before where the dark state is formed, shown in the red curve in Fig.

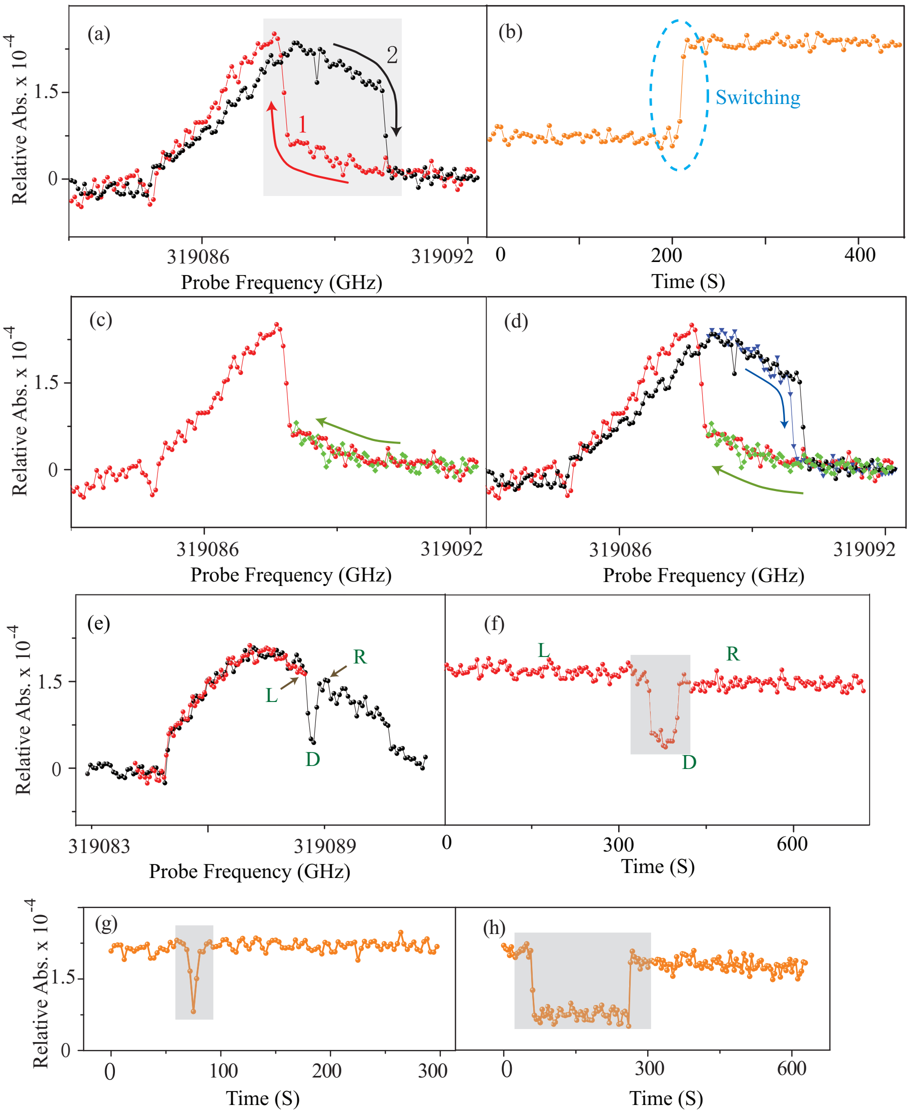

Figure 7.2: The Dynamics of Nuclear Spin Configuration. Data are taken at a magnetic field of 2.64 T. (a) Black (red) curve represents a full forward (backward) scan. (b) Green curve is a partial forward scan. Immediately after stopping the laser right before the rising edge of the trion absorption, (c) the probe absorption signal is taken as a function of time. The switching between hysteresis states 1 and 2 is observed. (d) Blue curve is the partial forward scan taken after the switching of the hysteresis states, which agrees with the full forward scan pretty well. The fine differences are explained in the theoretical discussion part of the text. (e) After we locate the dark state by a full forward scan (black curve), we take a partial forward scan (red curve) to prepare the nuclear spin configuration. L, D and R denote three system statues. Immediately after parking the laser right before where the dark state is formed, (f) we take the absorption signal as a function of the time. The system starts from statues L, switches to D, and finishes at status R, which indicates a dynamic evolution of the nuclear spin configuration. (g) and (h) show the dark state is a meta-stable state.

B.1(e). Immediately following that, we measure the absorption signal as a function of time, as shown in Fig. B.1(f). The system starts in status L, evidenced by the signal level, and jumps into status D after some time. This observation indicates that the Overhauser field shifts the electron spin Zeeman energy to match the two-photon resonance condition through the DNP process. The switching from status L to D happens very fast and we could not resolve the time scale. In experiments we noticed that the system can stay in the dark state on a time scale from a few seconds to 3 minutes. A few examples are shown in Fig. B.1(f-h). Since any change in the two-photon resonance will destroy the dark state, the system staying in the dark state indicates that the nuclear spin configuration is "quasi-frozen" for this time scale. Figure B.1(f) shows an example where status D lasts about 40s and then switches to status R.

7.3 Theoretical Explanation of the Hole Spin-Assisted Nuclei Self-Focusing Effect [33]

In order to fully understand the experimental observations, we gain insight into the hyperfine interaction by the realization that instead of the electron spin, it is the hyperfine interaction between the heavy hole spin of the trion and lattice nuclei which accounts for the experimental observations. In a single charged QD, the properties of the trion state are determined by the spin of the heavy hole, which is in the P state. The hyperfine interaction between the heavy-hole spin and nuclear spin is strongly anisotropic [26, 27]. Strictly speaking, the nuclei not only interact with the fraction of the hole in the same primitive unit cell ("on-site" interaction), but also with the probability density localized at more distant unit cells (long-ranged interactions). Nevertheless, it has been shown that the long-range part only leads to corrections on the order of 1% relative to the on-site interaction, and hence can be neglected [26,27]. We use 1/2 pseudo-spin $\boldsymbol{S}_h$ to denote the heavy hole subspace.

For a small quantum dot, heavy-light hole mixing is a non-negligible effect. The two "heavy hole" states after mixing are $|S_h^z = \frac{1}{2}\rangle \equiv \left|J_z = \frac{3}{2}\right\rangle - \eta \left|J_z = -\frac{1}{2}\right\rangle$ and

$\left|S_h^z = -\frac{1}{2}\right\rangle \equiv \left|J_z = -\frac{3}{2}\right\rangle - \eta \left|J_z = \frac{1}{2}\right\rangle$ where $\hat{z}$ is assumed to be the growth direction. The amount of mixing can be identified using polarization dependent absorption spectroscopy [30], as shown in Chpater 5. For the SAQD used in the experiment, $\eta \sim 0.2$ (refer to Eqn 1.9 in Chapter 2). Assuming the hole envelope function $f_h(\mathbf{R}_k)$ varies slowly on the length scale of a primitive cell, one finds the hyperfine interaction between the heavy hole spin and the nuclear spins [26, 27]

$$H_{h-n} = \sum_k A_{h,k}\left[S_h^z I_k^z + O(\eta)\left(S_h^y I_k^y + S_h^x I_k^x\right) + O\left(\eta^2\right)\left(S_h^x I_k^z + S_h^y I_k^z\right)\right] \tag{7.6}$$

where $A_{h,k} \equiv \mathcal{A}_{h,\alpha_k}\left|f_h(\mathbf{R}_k)\right|^2 \frac{c_0^3}{4}$. We have $A_{h,k} \sim \frac{2}{N}\mathcal{A}_{h,\alpha_k}$, similar to the electron case. For In and As, experiments and calculations lead to the estimation $\mathcal{A}_h \sim 0.1 - 0.2\mathcal{A}_e$ [26, 27]

Unlike the electron, the heavy hole spin couples to the nuclear spins through the anisotropic hyperfine interaction, which results in a significantly different dynamic polarization effect on the nuclear spins. In a magnetic field applied in the $\hat{x}$ direction, we define the nuclear spin raising and lowering operators $I_k^\pm = I_k^y \pm i I_k^z$. For the electron, the terms that flips the nuclear spin eigenstates in the field direction are $S_e^\mp I_k^\pm$ which always involve the simultaneous flip of the electron spin eigenstate. For the hole, we have unique terms like $S_h^x I_k^\pm$, which flip the nuclear spin eigenstates without changing the hole spin. This type of process is of direct relevance for the dynamics of the nuclear Overhauser shift observed in this experiment. If the magnetic field is entirely in the $x - y$ plane, such processes arise from the $O(\eta^2)\left(S_h^x I_k^z + S_h^y I_k^z\right)$ term in Eq. (7.6). If the magnetic field has some out-of-plane components, such processes can also arise from the $S_h^z I_k^z$ term in Eq. (7.6).

In particular, we focus on the non-collinear hyperfine coupling term $S_h^x I_k^z$. This interaction operator can flip a nuclear spin without flipping the hole spin, costing only the nuclear Zeeman energy $\hbar\omega_N \sim 0.01$ GHz/Tesla [34, 35]. Therefore, this process stands out from the various DNP interactions since the small energy cost can be directly compensated by the homogeneous broadening of the trion state ~ 0.4 GHz, while the processes by other collinear terms have to involve phonon emission/absorption to compensate for the energy cost of flipping the hole or electron spin.

In contrast, for the electron spin states, the term that can flip a nuclear spin eigenstate is $S_e^{\mp}I_k^{\pm}$. The spin state of the electron has to be simultaneously flipped with that of the electron, which costs the energy of the electron Zeeman energy $\hbar\omega_e$. This energy (about $\sim$ 7 GHz/T) can only be compensated by the emission or absorption of phonons. Although the hyperfine interaction is stronger for the electron, the efficiency of DNP by electron interaction may be significantly limited due to the weak coupling to the phonon bath.

Terms such as $S_h^z I_k^z$ and $S_h^y I_k^y$ in the trion-nuclear hyperfine interaction can also flip the nuclear spin with a simultaneous flip of the hole spin. But similarly, their roles in DNP can be diminished by the fact that phonon processes are necessary to compensate for the energy cost of flipping the hole spin. Below we focus on the role of the $S_h^x I_k^{\pm}$ terms.

From Fermi's Golden rule, we find the nuclear spin flip rates are proportional to $\rho_{t,i}\rho_{t,f}$, where $\rho_{t,i}$ ($\rho_{t,f}$) is the trion population before (after) a nuclear spin flip. The rates for the nuclear spin to flip up and down are different, since they have different effects on the electron Zeeman splitting and hence create different trion populations $\rho_{t,f}$. Since $\rho_{t,i}$ is the same for a particular flipping process, it is clear that the one resulting in a larger $\rho_{t,f}$ always wins, i.e. the DNP process tends to maximize trion excitation. The net DNP rate is proportional to $\rho_t \frac{\partial \rho_t}{\partial \delta}$, where δ is probe laser detuning from the trion frequency. Figure 7.3(b) plots the calculated $\rho_t \frac{\partial \rho_t}{\partial \delta}$ as a function of the laser frequency without the DNP effect. We can see that the net DNP rate goes to zero at the maxima of the trion population (also the position of strongest absorption), located at $\pm\delta_s$. In our theory, a positive DNP rate pulls trion transition V2 (i.e. it shifts the entire spectrum) to the red while a negative DNP rate pushes trion transition V2 to the blue. This creates a restoring force around the absorption maxima, such that when the laser is slightly detuned from the position of strongest absorption, the Overhauser field acts to adjust the Zeeman splitting to maximize the trion excitation. Thus, as the laser scans, the system actively self-focuses into its stable configuration by tuning the electron spin Zeeman splitting through the DNP

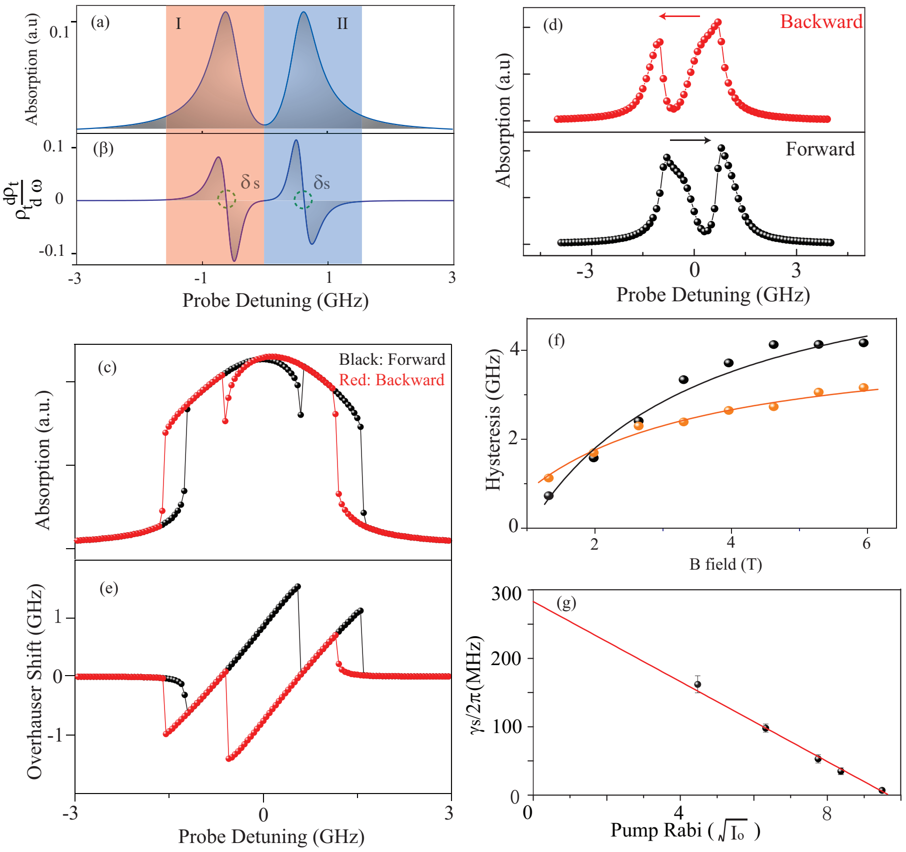

Figure 7.3: The Self-Focusing of Nuclei With the Narrowing the Inhomogeneous Broadening of the Overhauser Field. The calculated (a) probe absorption spectrum and (b) $\rho_t \frac{\partial \rho_t}{\partial \omega}$ by solving the three-level Lambda system with pump on resonance in the absence of DNP. Figure (b) shows the Overhauser field acting as a restoring force. Numerical simulation results including the self-focusing of the nuclei effects for (c) slow scan and (d) fast scan corresponding to a magnetic field of 1.32 T. (e) is the calculated Overhauser shift corresponding to the slow scan. The positive (negative) Overhauser-shift shifts the probe absorption spectrum to the blue (red). (f) The hysteresis (black dots) and the detuning of the dark state (orange dots) caused by the DNP effect as a function of the magnetic field, which shows a saturation effect. Lines on top of the data are guides to the eye. (g) The extracted $\gamma_s/2\pi$ from the dark state data as a function of square root of the pump intensities, where $I_o = 2W/cm^2$.

process.

We can use this self-focusing mechanism to further explain our experimental observations. When the laser scans forward and approaches the first trion population maximum, the scan and "pull" directions are anti-parallel. The DNP effect "pulls" the trion resonance into the oncoming laser, leading to a fast, sharp rise of the absorption signal. As the laser keeps stepping forward, the DNP will "push" the trion transition to follow the laser frequency in order to maintain the stable configuration, which leads to the round top in the spectrum and pushes the two-photon resonance to the blue. However, intrinsic nuclear spin relaxation eventually wins out and depolarizes the nuclear spins, which shifts the spectrum opposite to the DNP direction. This brings the system quickly into the dark state and leads to the sharp edge. Parking the laser in or near this dark state configuration leads to the observations shown in Fig. B.1(f-h), which confirms that the dark state is metastable and the trion absorption maximum is indeed the stable configuration for DNP. If the laser continues to scan, the system again self-focuses quickly into its stable configuration in region II, leading to another round top, until, once more, nuclear spin relaxation wins over.

The features of the backward scan can also be understood in the same way as the forward scan. As the probe laser moves into region II, the laser scan direction is antiparallel to the DNP "push" direction, leading to a sharp increase in absorption. An interesting feature we should point out is that there is no dip observed in the partial forward scan in Fig. B.1(d) (blue line) compared to the full forward scan (black line). This is a signature that the system jumps from the low absorption hysteresis state 1 into the stability region II. Since region II is already on the blue side of the dark state, there is no dark state formed during the partial forward scan. We can also expect that spectra of the partial (blue line) and full (black line) forward scans should be shifted from each other by a small amount, seen in Fig. B.1(d). The spectral shifts between partial and full forward scans can be controlled by adjusting the relative spectral positions between the dark state and the sharp rise of the backward scan, which is controlled by the pump detuning.

The dynamics of the Overhauser shift $\Delta \equiv \omega_e - \omega_{e,0}$ (where $\omega_{e,0}$is the Zeeman splitting by the external field only) are described by the equation:

$$\frac{d\Delta}{dt} = -\gamma_n \Delta + \alpha \rho_t \frac{\partial \rho_t}{\partial \delta} \tag{7.7}$$

where γ_n is the nuclear spin relaxation rate, $\alpha \sim O\left(\eta^4\right) \mathrm{A}_h^2 \mathrm{A}_e^2 \gamma_t^{-1} N^{-3}$, η is the amount of heavy-light hole mixing, $\mathrm{A}_h (\mathrm{A}_e)$ is the hyperfine constant for hole-nuclear (electron-nuclear) coupling, γ_t is the trion homogeneous broadening, and N is the number of nuclear spins in the quantum dot [28]. ρ_t as a function of δ is calculated using the optical Bloch equations.

We numerically simulate the self-focusing process by including DNP in the optical Bloch equations. Figure 7.3(c) ((d)) shows an example of the simulation result for slow (fast) scans at magnetic field of 1.32T. We can see that the numerical simulations qualitatively reproduce many features of the experimental observations, including the edge hysteresis, the shape and spectral detuning of the dark state dip, the round and broadened top of the absorption peak in the slow scan. The evolution of the Overhauser shifts as a function of the probe frequency and scan direction are plotted in Fig. 7.3(e), which clearly show the origins of all the spectral features. A best fit to the fast scan data is produced with parameters $\gamma_n = \frac{2.5}{2\pi}$ Hz; $\alpha = 35$ MHz^3, while a best fit to the slow scan data is obtained with $\gamma_n = \frac{1.5}{2\pi}$ Hz; $\alpha = 3.2$ MHz^3. These values of α correspond to hole-nuclear hyperfine constant $\mathrm{A}_h \approx 16\ \mu$eV and $\mathrm{A}_h \approx 5\ \mu$eV respectively, in reasonable agreement with the estimation given in Ref [26, 27]

7.4 Suppression of the Nuclear Spin Fluctuations

We also examine the hysteresis effect and the detuning of the dark state by varying the magnetic fields up to 6 T. The hysteresis is quantified by the separation between the rising edge of the backward scan and the falling edge of the forward scan. Figure 7.3(f) plots the hysteresis (black dots) and the separation of the dark states (orange dots) as a function of the magnetic fields. The hysteresis and the detuning increase first and saturate at high magnetic fields. Since the magnitudes of the hysteresis and the dark state shift reflect the nuclear field established by DNP, larger hysteresis and dark state shifts could correspond to smaller nuclear spin relaxation rates. The above field dependent observations may indicate that the nuclear spin relaxation rate in the charged QD system decreases with increasing magnetic fields and saturates at high fields, consistent with the observations in other systems [19].

The self-focusing effect can lead to the suppression of the nuclear spin fluctuations, which enhances the electron spin T2*. Once the system has switched to a configuration of maximum trion excitation, the electron spin Zeeman energy and hence the nuclear field are only determined and controlled by the instantaneous laser frequency, regardless of the initial nuclear spin configuration before the scan starts. In this regime, DNP can actively work to maximize the trion population and any nuclear spin fluctuations which shift the Zeeman resonance are canceled out through feedback via the DNP mechanism. Therefore, the self-focusing process narrows the inhomogeneous broadening of the Overhauser field and enhances the electron spin decoherence time T2*.

The narrowing effect on the inhomogeneous broadening is verified from the CPT spectroscopy which provides frequency domain information on the electron spin T2*. From the fast scan data, we can extract the electron spin decoherence rate of $\gamma_s/2\pi \approx$ 50 MHz. In contrast, for our dot (∼3 nm in height and ∼15 nm in base diameter [23]), the spin inhomogeneous broadening due to a thermally distributed nuclear environment is estimated to be 360 MHz [10], much larger than the 50 MHz extracted from our fast scan CPT data. We attribute this discrepancy to the suppression of the nuclear spin fluctuations caused by the self-focusing effect.

Furthermore, we find that the narrowing of inhomogeneous broadening of the spin coherence becomes more significant with increasing pump power. The extracted spin inhomogeneous broadening is plotted in Fig. 7.3(g) as a function of the square root of the laser intensities. Surprisingly, a linear line fits the data. We extrapolate $\gamma_s/2\pi$ of 290 MHz in the absence of the DNP by extrapolating the line to zero pump power, which reasonably agrees with the theoretical prediction. For the highest applied pump power, we find $\gamma_s/2\pi = (7 \pm 3)$ MHz, which corresponds to a 40 times enhancement of the spin T2* time and is limited by the current experimental configuration. We expect the narrowing effect to be more significant under higher pump powers. We further anticipate a spin quantum beats experiment to confirm this enhancement of spin T2* from direct time domain measurement.

References

[1] D. Loss, D. P. DiVincenzo, Physical Review A **57**, 120 (1998).

[2] D.Gammon, D. G. Steel, Physics Today **55**, 36 (2002).

[3] M. Kroutvar et al., Nature **432**, 81 (2004).

[4] A. S. Bracker et al., Phys. Rev. Lett **94**, 047402 (2005).

[5] J.R. Petta et al., Science **309**, 2180 (2005).

[6] A. Greilich et al., Science **317**, 1896 (2007).

[7] J. Berezovsky, M. H. Mikkelsen, N. G. Stoltz, L. A. Coldren, D. D. Awschalom, Science **320**, 349 (2008).

[8] B. D. Gerardot et al., Nature **451**, 441 (2008).

[9] L. Robledo et al., Science **320**, 772 (2008).

[10] I. A. Merkulov, A. L. Efros, M. Rosen, Phys. Rev. B **65**, 205309 (2002).

[11] F. H. L. Koppens et al., Science **309**, 1346 (2005).

[12] B. Eble et al., Phys. Rev. B **74**, 081306 (2006).

[13] A. I. Tartakovskii et al., Phys. Rev. Lett. **98**, 026806 (2007).

[14] D. J. Reilly et al., Science **321**, 817 (2008).

[15] J. Baugh, Y. Kitamura, K. Ono, S. Tarucha, Phys. Rev. Lett. **99**, 096804 (2007).

[16] P. Maletinsky, C. W. Lai, A. Badolato, A. Imamoglu, Phys. Rev. B **75**, 035409 (2007).

[17] S. E. Harris, Physics Today **50**, 36 (1997).

[18] D. Stepanenko, G. Burkard, G. Giedke, A. Imamoglu, Phys. Rev. Lett. **96**, 136401 (2006).

[19] A. Abragam, The Principles of Nuclear Magnetism. (Oxford, Claredon Press, 1973).

[20] C.W. Lai, P. Maletinsky, A. Badolato, and A. Imamoglu, Phys. Rev. Lett **96**, 167403(2006).

[21] A. C. Johnson *et. al.*, Nature **435**, 925 (2005).

[22] M.V. G. Dutt *et al.*, Phys. Rev. Lett. **94**, 227403 (2005).

[23] M. Scheibner et al., Nat Phys **4**, 291 (2008).

[24] D. Paget et al., Phys. Rev. B **15**, 5780 (1977).

[25] G. Ramon, X. Hu, Phys. Rev. B **75**, 161301(R) (2007).

[26] B. Eble et al., arXiv:0807.0968v1 (2008).

[27] J. Fischer, W. A. Coish, D. V. Bulaev, D. Loss, arXiv:0807.0386v1 (2008).

[28] M. E. Ware et al., Phys. Rev. Lett. **95**, 177403 (2005).

[29] X. D. Xu et al., Phys. Rev. Lett. **99**, 097401 (2007).

[30] . A. V. Koudinov, I. A. Akimov, Y. G. Kusrayev, F. Henneberger, Phys. Rev. B **70**, 241305 (2004).

[31] X. Xu *et al.*, Nature Physics **4**, 692 (2008).

[32] K. R. Wald, L. P. Kouwenhoven, P. L. McEuen, N. C. van der Vaart, C. T. Foxon, Phys. Rev. Lett. **73**, 1011 (1994).

[33] Theory is originally worked out by W. Yao and L. J. Sham.

[34] J. M. Kikkawa, D. D. Awschalom, Science **287**, 473 (2000).

[35] D. Gammon et al., Science **277**, 85 (1997).

CHAPTER 8

Summary and Future Direction

In this chapter, I will summarize the work in this thesis and look into the experiments and research directions for the near future.

8.1 Thesis Summary

This thesis focused on the coherent optical spectroscopy of a single InAs SAQD. The QD is embedded in a Schottky diode structure, which gives us the ability to actively control the number of electrons in the QD by adjusting the bias across the sample [1]. We started with photoluminescence characterization of a single QD and show the charging effects [2]. The SAQD has a very strong lateral confinement, therefore, it behaves like a single atom in many ways [3, 4]. When a strong laser interacts with an atomic transition, the atomic states will be dressed by the laser photons [5]. We first demonstrated the dressed QD states by the optical Mollow absorption spectrum [3, 6]. In this experiment, we utilized the V system formed by two polarized neutral exciton states. The Autler-Townes splitting was demonstrated when pump and probe beams couple different transitions [7], while the optical Mollow absorption spectrum was shown if the pump and probe beams were on the same transition. Gain without inversion was also demonstrated by observing the negative absorption of the probe beam. This gain effect results from the coherent energy exchange between the pump and probe beams through the QD nonlinearity. This work shows that the QD state is well isolated from the solid state environment and behaves like a single atom even in the high optical field strength limit. In systems with weaker confinement or higher dimensionality, we have seen the transition from simple atomic behavior to complex many body behavior, which is not good for quantum devices. In the experiment, we found we could achieve ultrafast operation of the dot state using a relatively inexpensive CW diode laser rather than the more expensive but common time domain pulsed laser, achieving Rabi oscillation of up to 1.4 GHz. These results, which are published in Science 319, 929 (2007), may dramatically change how researchers can imagine achieving optically driven quantum computing based on QDs systems using commercial telecommunications technology.

In the next step, we studied a single charged QD driven by a strong optical field and also observe the optical Mollow absorption spectrum. When the strong pump was on resonance with the trion transition, a triplet appeared in the probe absorption spectrum with a weak center peak and two Rabi side bands with dispersive lineshapes. As the pump beam was detuned from the trion transition, three spectral features were observed: a weak dispersive lineshape centered at the driving field frequency flanked by an AC Stark shifted absorption peak and a Raman gain side band. The observation of the typical features of a two level atomic system demonstrated that the manybody system of 2 electrons and 1 hole follow the predictions of the atomic theory first developed by Mollow for a strongly driven 2 level system.

The spin state initialization experiment in Chapter 5 demonstrated that a solid state qubit can be initialized at a rate much faster than its decoherence rate [8]. A single electron spin has been proposed as a good qubit candidate for quantum information and quantum computation (QIQC) where the qubit replaces the bit (used in a classical computer). One of the key requirements of the QIQC is qubit preparation. QIQC requires not only qubits to be initialized in a known state for computation and gate operations, but also a continuous supply of low-entropy ancillary qubits for quantum error correction [9]. Fault tolerant QIQC requires about 10^4 operations before the qubit looses its coherence. In our work, we demonstrated a fast electron spin state initialization by applying a magnetic field perpendicular to the sample growth direction. This so called spin cooling technique is the same as the optical pumping effect in atomic systems. The experimental results are an important step towards the realization of the fault tolerant QIQC in the solid state QD system, and is reported in Phys. Rev. Lett. 99, 097401 (2007).

The coherent population trapping of an electron spin was demonstrated in a singly-charged quantum dot in Chapter 6. Coherent population trapping (CPT), resulting from the coherent superposition of two ground states coupled by coherent optical fields to an intermediate state, is the basis for electromagnetically induced transparency [10]. By applying a magnetic field in the Voigt geometry, we created a three-level lambda system, formed by two Zeeman sublevels of an electron spin and an intermediate trion state [8]. As we tuned the driving and probe fields to the two-photon Raman resonance, we observe a pronounced dip in the probe absorption spectrum, indicating the CPT of the electron spin. An arbitrary superposition of the electron spin states can be prepared by varying the ratio of the Rabi frequencies between the driving and probe fields. The experimental results, published in Nature Physics 4, 692 (2008) show that spin based semiconductor quantum dot systems have the potential to be used for EIT, slow light [11], and quantum information storage applications [12].

By using the CPT technique developed in Chapter 6, we demonstrated the preparation, subsequent probe and control of the Overhauser field in a single charged QD. With a finite magnetic field and fixed pump laser frequency, we can control the nuclear spin configuration by simply switching the scan direction of the probe laser. The dynamic nuclear spin polarization (DNP) manifested itself both in a laser scan direction dependent hysteresis effect and the frequency detuning of the dark state. We also observe the switching of the nuclear spin configuration by fixing the laser frequencies and monitoring the coherent optical response as a function of time. Our data indicate a narrowing of the inhomogeneous broadening of the Overhauser field evident by the enhancement of the electron spin T2*. The self-focusing of nuclei into its stable configuration through the hole spin-assisted DNP process can well explain all the experimental observations. Both experimental results and theoretical development can lead to a valuable understanding and possibly arbitrary control of the hyperfine interaction while coherently manipulating a single spin in such hyperfine interaction mediated solid state nano-structures.

8.2 Future Directions

Based on the experimental achievements in this thesis, I will discuss a few possible experiments which could be performed either immediately or in the near future in this section.

8.2.1 Hyperfine Interaction of a Single Spin With Nuclei

Since QDs have a three dimensional confinement, the wave function of a electron spin inside a QD is strongly localized. Thus, the primary spin relaxation mechanism in the bulk semiconductor, the coupling of the spin and orbital momentum, is strongly suppressed [13]. However, the strongly localized wave function enhances the hyperfine coupling between the electron spin and lattice nuclei, which leads to electron spin decoherence [14–16]. Although the intrinsic electron spin T2 can be measured by the spin echo technique [17], this technique is not convenient in the real quantum computing application of spins. One would like to fully utilize the intrinsic T2 by simple techniques without any complicated coherence recovery process during the manipulation of spins, which can be achieved by the suppression of the nuclear spin fluctuations before operating on the spins. Although there are many proposals about suppressing the nuclear spin fluctuations in QDs [18–20], only two experiments towards this goal have been performed. One is on a gate-confined double dot system using a transport measurement [21], and the other is on an ensemble of SAQDs using an optical measurement [22].

In the optical measurement, the electron spin precession frequencies are focused into a few modes assisted by the Overhauser field, where the modes are determined by a designed pulse protocol [22]. In this way, the fluctuation of the nuclear spins is suppressed. Due to the long lifetime of the nuclear spins, the electron spin coherence can be imprinted into the nuclei spins and stored for a few minutes in the dark. A better scheme is realized in the transport measurement [21]. In that experiment, no complex pulse sequence is used. The nuclear spin fluctuations are suppressed by a cyclic evolution of the two-spin states, although the physical origin of the suppression is not clear yet. The basic experimental process is that the electron spins, which are in a singlet state, are adiabatically brought into a spin triplet state, and then immediately non-adiabatically pumped back to the initial spin singlet state. Therefore, angular momentum is transferred between the electron and nuclear spins in this one cycle. The cyclic process is done at a 4 MHz rate and the maximum nuclear spin polarization achieved in the experiment is about 1%, which leads to a 70 times increase of the electron spin T2*.

In our experiment, we would like to optically manipulate a single spin in a single QD. An ideal way to extend spin T2* is to suppress the nuclear spin fluctuations before the manipulation of the spin. The early proposal for suppressing the nuclear spin fluctuations is to initialize the nuclear spin polarization $>$ 99% [13]. Such a high degree of polarization of the nuclear spins is very difficult to achieve [23]. In our case, we could use the the self-focusing process developed in chapter 7 to suppress the nuclear spin fluctuations. The proposed experimental procedure is as follows. First we can use two CW lasers to suppress the nuclear spin fluctuations. As discussed in chapter 7, a strong pump is fixed to be nearly resonant with one trion transition and a weak probe scans across the other trion transition in a three-level Lambda system. After the strong absorption peak is located, which is the most stable configuration of the nuclei, the probe laser is fixed at this particular frequency. Since the nuclear spin has a long lifetime, after narrowing the inhomogeneous broadening of the Overhauser field, we could block both CW lasers and do time domain operations. After the pulse operations, the nuclear spin configuration is re-initialized by unblocking both CW lasers. Therefore, in each run, we illuminate the QD with both CW lasers for a second, and then manipulate the electron spin with pulse lasers. Longer lasting spin quantum beats would be direct experimental evidence of the suppression of nuclear spin fluctuations. The electron spin T2* is also expected to be bigger as the laser power is increased.

Anther method to suppress the nuclear spin configuration is proposed based on coherent population trapping in Ref [25]. When the pump and probe lasers match the two-photon resonances in a three level lambda system, the spin ground states form a dark state. Therefore, the emission from the excited trion state will be greatly reduced. Due to the fluctuation of the Overhauser field, the two photon resonance condition is destroyed and, thus, the emission of the trion state increases. In this scheme, the change of the emission of the trion state can be used to as a feedback signal to re-adjust the laser frequencies. Once the change of trion emission is detected, the lasers are adjusted to new positions to minimize the emission. In this dynamic feedback process, the nuclear spin fluctuation can be suppressed. The numerical simulation in Ref. [25] shows a factor of 100 enhancement of T2*. However, since we observe the self-focusing effect of the nuclei in the CPT process, the impact of the self-focusing mechanism on this scheme is not clear.

8.2.2 A Singly Charged Quantum Dot in a Nano-Cavity

Cavity quantum electrodynamics experiments in semiconductor nano-cavities by using QDs as artificial atoms have been emerging quickly in the past few years. Vacuum Rabi splitting has recently been demonstrated in Ref [26–28]. The controlled transmission, reflection, and phase of light by a QD embedded in a photonic crystal (PC) Nano-cavity are also realized [29, 30]. Recently, there has also been a report on a single QD in a PC Nano-cavity as a single photon transistor [31]. There are many proposals on quantum networks based on the QD coupled cavity system. Many experiments have been done in the area of cavity QED with atomic ensembles, such as entanglement distribution between two remote nodes [32] and mapping photonic entanglement into and out of the atomic states [33]. One common feature for these experiments is that a three-level Lambda system is used. We know that a singly charged quantum dot can form a three-level Lambda system with the applied magnetic field in the Voigt geometry. Further more, current progress of QD cavity QED is on neutral QDs. Therefore, it will be interesting and important to study a single charged QD embedded in a cavity.

Ideally, we would like to embed the QD in a nanocavity with a very high Q and very small mode volume, which leads to small cavity damping and strong coupling to the QD. We also require bias control of the quantum dot, so that the charging state can be controlled using the applied voltage. While the bias control is critical, it is a technical challenge to build a diode structure into the cavity since the Q factor will be significantly decreased. Recently, there was a talk on a charged QD in a micro-cavity [34]. The switching of the polarization of light was demonstrated. However, the cavity in that work had a very large mode volume in order to build a diode structure. These technical issues must be solved before charged QD nano-cavity systems can be applied to solve real world problems. Nerveless, there is rich physics in a charged QD embedded in the nanocavity system that has yet to but needs to be explored .

In summary, this thesis has reviewed many new results in area of coherent optical control and spectroscopy of single electron doped quantum dots. The results demonstrate the important achievement of many milestones identified to build an optically driven quantum dot based quantum computer as well as revealing new and exciting physics regarding nuclear coupling that may open the door to even more novel ideas.

References

[1] M. Kroner *et al.*, Nature **415**, 311 (2008).

[2] M. E. Ware *et al.*, Phys. Rev. Lett. **95**, 177403 (2005).

[3] X. Xu *et. al.* , Science **317**, 929 (2007).

[4] A. Muller *et al.*, Phys. Rev. Lett. **99**, 187402 (2007).

[5] J. Dupont-Roc, G. Grynberg, C. Cohen-Tannoudji, Atom-Photon Interactions: Basic Processes and Applications (John Wiley and Sons Inc, 1998).

[6] B. R. Mollow, Phys. Rev. A. **5**, 2217 (1972).

[7] S. H. Autler, C. H. Townes, *Phys. Rev.* **100**, 703 (1955).

[8] X. Xu, *et. al.* , *Phys. Rev. Lett.* **99**, 097401 (2007).

[9] D. P. DiVincenzo, *Fortschr. phys.* **48**, 771 (2000).

[10] S.E. Harris, *Physics Today* **50** (**??**), 36 (1997).

[11] L. V. Hau, S. E. Harris, Z. Dutton, C. H. Behroozi, *Nature* **397**, 594 (1999).

[12] C. Liu, Z. Dutton, C. H. Behroozi, L. V. Hau, *Nature* **409**, 490 (2001).

[13] G. Burkard, D. Loss, D. P. DiVincenzo, *Phys. Rev. B* 59, 2070 (1999).

[14] A. V. Khaetskii, D. Loss, L. Glazman, *Phys. Rev. Lett.* **88**, 186802(2002).

[15] W. A. Coish, D. Loss, *Phys. Rev. B* **70**, 195340 (2004).

[16] A. C. Johnson *et al.*, *Nature* **435**, 925 (2005).

[17] J. R. Petta *et al.*, *Science* **309**, 2180 (2005).

[18] A. Imamoglu, E. Knill, P. Zoller, *Phys. Rev. Lett.* **91**, 017402 (2003).

[19] D. Klauser, W. A. Coish, D. Loss, *Phys. Rev. B* **73**, 205302 (2006).

[20] G. Giedke, J. M. Taylor, D. DAlessandro, M. D. Lukin, A. Imamoglu, *Phys. Rev. A* **74**, 032316 (2006).

[21] D. J. Reilly et al., *Science* **321**, 817 (2008).

[22] A. Greilich *et al.*, Science **317**, 1896 2007.

[23] A. S. Bracker *et al.*, *Phys. Rev. Lett.* **94**, 047402 (2005).

[24] M. V. G. Dutt, *et al.*, *Phys. Rev. Lett.* **94**, 227403 (2005).

[25] D. Stepanenko, G. Burkard, G. Giedke, A. Imamoglu, *Phys. Rev. Lett.* **96**, 136401 (2006).

[26] J. P. Reithmaier *et al.*, *Nature* **432**, 197 (2004).

[27] T. Yoshie *et al.*, *Nature* **432**, 200 (2004).

[28] K. Hennessy *et al.*, *Nature* **445**, 896 (2007).

[29] D. Englund *et al.*, *Nature* **450**, 857 (2007).

[30] I. Fushman *et al.*, *Science* **320**, 769 (2007).

[31] A. Faraon *et al.*, arXiv:0804.2740.

[32] C. Chou *et al. Science* **316**, 1316 (2007).

[33] K. S. Choi, H. Deng, J. Laurat, H. J. Kimble, *Nature* **452**, 67 (2007).

[34] M. Rakher *et al.* J24.00013 APS March Meeting (2008).

APPENDICES

APPENDIX A

Derivation of Spin State Preparation Efficiency

In appendix A, we will derive the optical pumping efficiency for the scheme presented in Chapter 5. Considering a four-level trion system shown in Fig. A.1, a pump beam is near resonant with transition V1 with a vertical polarization. Since transition V2 is also vertically polarized, the pump beam is also off resonantly coupled to transition V2. The Hamiltonian can be written as

$$H = \hbar \begin{pmatrix} \omega_{14} & X_{12}^* & 0 & 0 \\ X_{21} & \omega_{24} & 0 & 0 \\ 0 & 0 & \omega_{34} & X_{34} \\ 0 & 0 & X_{43}^* & 0 \end{pmatrix} \tag{A.1}$$

where $X_{ij} = \frac{-\mu_{ij} * E}{2\hbar}$, μ_{ij} is the dipole moment and E is the pump field strength. From the optical Bloch equations, we write out the density matrix equations

$$\begin{aligned}
\frac{d\rho_{11}}{dt} &= -i(X_{12}^*\rho 21 - X_{21}\rho_{12}) + \Gamma_{21}\rho_{22} + \Gamma_{31}\rho_{33} + \Gamma_{41}(\rho_{44} - \rho_{11}) && \text{(A.2)} \\
\frac{d\rho_{22}}{dt} &= -i(X_{21}\rho 12 - X_{12}^*\rho_{21}) - \Gamma_{21}\rho_{22} - \Gamma_{24}\rho_{22} && \text{(A.3)} \\
\frac{d\rho_{33}}{dt} &= -i(X_{34}\rho 43 - X_{43}^*\rho_{34}) - \Gamma_{31}\rho_{33} - \Gamma_{34}\rho_{33} && \text{(A.4)} \\
\frac{d\rho_{44}}{dt} &= -i(X_{43}^*\rho 34 - X_{34}\rho_{43}) + \Gamma_{24}\rho_{22} + \Gamma_{34}\rho_{33} + \Gamma_{41}(\rho_{11} - \rho_{44}) && \text{(A.5)} \\
\frac{d\rho_{21}}{dt} &= -i(X_{21}\rho 11 - X_{21}\rho_{22} + \rho_{21}\omega_{21}) - \gamma_{21}\rho_{21} && \text{(A.6)} \\
\frac{d\rho_{34}}{dt} &= -i(X_{34}\rho 44 - X_{34}\rho_{33} + \rho_{34}\omega_{34}) - \gamma_{34}\rho_{34} && \text{(A.7)}
\end{aligned}$$

In the above equations, Γ_{ij} (γ_{ij}) is the decay (dephasing) rate from state i to state j.

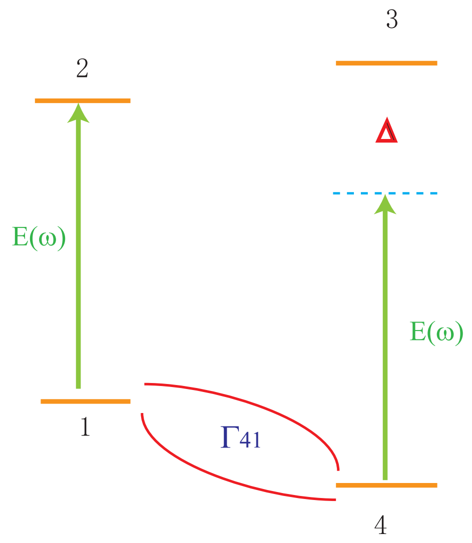

Figure A.1: Schematic of a Four Level Structure

We rewrite the density matrix elements in the field interaction picture

$$\rho_{21} = \widetilde{\rho}_{21} e^{-i\omega t}, \rho_{34} = \widetilde{\rho}_{34} e^{-i\omega t} \tag{A.8}$$

Substituting the above formula into equations A.6 and A.7, we obtain

$$\widetilde{\rho}_{21} = \frac{iX_1(\rho_{22} - \rho_{11})}{i\delta_1 + \gamma_{21}} \widetilde{\rho}_{34} = \frac{iX_2(\rho_{33} - \rho_{44})}{i\delta_2 + \gamma_{34}} \tag{A.9}$$

where $X_1 = \mu_{21}.E/2\hbar$ and $X_2 = \mu_{34}.E/2\hbar$.

We insert $\widetilde{\rho}_{21}$ and $\widetilde{\rho}_{34}$ back to equation A.2-A.4 and obtain the rate equations

$$\begin{aligned}
\frac{dn_1}{dt} &= \frac{2X_1^2(n_2 - n_1)\gamma_{21}}{\gamma_{21}^2 + \delta_1^2} + \Gamma_{21}n_2 + \Gamma_{31}n_3 + \Gamma_{41}(n_4 - n_1) && \text{(A.10)} \\
\frac{dn_1}{dt} &= \frac{-2X_1^2(n_2 - n_1)\gamma_{21}}{\gamma_{21}^2 + \delta_1^2} - (\Gamma_{21} + \Gamma_{24})n_2 && \text{(A.11)} \\
\frac{dn_3}{dt} &= \frac{-2X_2^2(n_3 - n_4)\gamma_{34}}{\gamma_{34}^2 + \delta_2^2} - (\Gamma_{31} + \Gamma_{34})n_3 && \text{(A.12)} \\
\frac{dn_4}{dt} &= \frac{2X_2^2(n_3 - n_4)\gamma_{34}}{\gamma_{34}^2 + \delta_2^2} + \Gamma_{24}n_2 + \Gamma_{34}n_3 + \Gamma_{41}(n_1 - n_4) && \text{(A.13)} \\
& && \text{(A.14)}
\end{aligned}$$

where $\delta_1 = \omega_{21} - \omega$, $\delta_2 = \delta_1 + \Delta$ and Δ is the sum of the electron and hole Zeeman splitting. By solving the rate equations, we obtain

$$n_1 = \frac{2\Omega_1^2\gamma_{21} + \Gamma_2\gamma_{21}^2 2\Gamma_{31}\Omega_2^2\gamma_{34}}{[(4(\Gamma_{24} + \Gamma_{31})\Omega_2^2\gamma_{34} + \Gamma_{24}\Gamma_3(\gamma_{34}^2 + \Delta^2))]2\Omega_1^2\gamma_{21} + 2\Gamma_{31}\Gamma_2\Omega_2^2\gamma_{21}^2\gamma_{34}} \tag{A.15}$$

If we assume $\Omega_1 \cong \Omega_2 = \Omega$, $\Gamma_{24} \cong \Gamma_{31} = \Gamma$, $\gamma_{21} \cong \Gamma$, $\Gamma_2 \cong \Gamma_3 = 2\Gamma$, the formula of n_1 can be simplified to

$$n_1 = \frac{\Omega^2 + \Gamma^2}{4\Omega^2 + 2\Gamma^2 + \Delta^2} \tag{A.16}$$

Therefore, the optical pumping efficiency is $1 - n_1$.

APPENDIX B

Derivation of The Probe Absorption Formula for the Mollow Absorption Spectrum

In appendix A, we will derive the analytical formula for the probe absorption under a strong optical pump field presented in Chapters 3 and 4. Considering a two level system shown in Fig. B.1, a pump beam is near resonant with the atomic transition and a probe beam scan across it. Since the pump beam is much stronger than the probe, we can solve the probe to the first order and pump to all order. First we ignore the probe beam and solve the pump to all order. The Hamiltonian in the field interaction picture with rotating wave approximation can be written as

$$H = \hbar \begin{pmatrix} 0 & X_1 \\ X_1 & \delta_1 \end{pmatrix} \tag{B.1}$$

where $X_1 = \frac{-\mu * E_1}{2\hbar} = -\Omega_1/2$, μ is the dipole moment ,E_1 is the pump field strength, and $delta_1 = \omega_1 - \omega_o$ is the pump detuning from the resonance. From the optical Bloch equations, we write out the density matrix equations

$$\begin{aligned} 0 &= iX_1(\rho^o_{21} - \rho^o_{12}) - \Gamma\rho^o_{22} && \text{(B.2)} \\ 0 &= -iX_1(\rho^o_{22} - \rho^o_{11}) - (\gamma - i\delta_1)\rho^o_{12} && \text{(B.3)} \\ 1 &= \rho^o_{11} + \rho^o_{22} && \text{(B.4)} \\ & && \text{(B.5)} \end{aligned}$$

In the above equations, Γ (γ) is the decay (dephasing) rate from state 2 to state 1. Solving the above equation, we can obtain the density matrix elements ρ^o_{22},ρ^o_{11},ρ^o_{21}

corresponding to all orders to the pump E_1. Then we write out the density matrix equation in the pump field interaction picture including the probe field

$$\begin{aligned} \frac{d\rho_{22}}{dt} &= (iX_1 + iX_2 e^{-i\Delta t})(\rho_{21} - \rho_{12}) - \Gamma \rho_{22} && \text{(B.6)} \\ \frac{d\rho_{12}}{dt} &= (-iX_1 - iX_2 e^{i\Delta t})(\rho_{22} - \rho_{11}) - (\gamma - i\delta_1)\rho_{12} && \text{(B.7)} \\ 1 &= \rho_{11} + \rho_{22} && \text{(B.8)} \\ & && \text{(B.9)} \end{aligned}$$

We try a solution with a form of

$$\rho_{ij} = \rho_{ij}^{o} + \rho_{ij}^{1}, \tag{B.10}$$

where

$$\rho_{ij}^{1} = a_{ij} + b_{ij} e^{i\Delta t} + c_{ij} e^{-i\Delta t} \tag{B.11}$$

Δ is the probe detuning from the pump frequency, b_{12} corresponds to the probe absorption and c_{12} corresponds to the new four wave mixing signal.

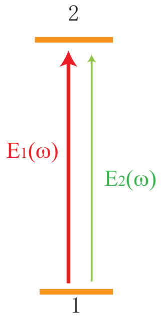

Figure B.1: Schematic of a Two-Level System. A weak beam (green arrow) probe a level-system driven by a strong pump (red arrow).

We substitute Eqn. B.10 into Eqn. B.9 and equate constants and the coefficients of $e^{i\Delta t}$. We obtain

$$\begin{aligned} 0 &= 2iX_1 b_{22} + (\gamma - i\delta_1 + i\Delta) b_{12} + iX_2(\rho_{22}^{o} - \rho_{11}^{o}) && \text{(B.12)} \\ 0 &= (-i\Delta - \Gamma) b_{22} + iX_1 b_{21} - iX_1 b_{12} + iX_2 \rho_{21}^{o} && \text{(B.13)} \\ 0 &= 2iX_1 b_{22} - (\gamma + i\delta_1 + i\Delta) b_{21} && \text{(B.14)} \\ & && \text{(B.15)} \end{aligned}$$

Solving the above equations, we obtain the absorption coefficient

$$\alpha = \mathrm{Im}\left[\frac{\alpha_o \Gamma A[i\Gamma A^*(A^* + i\Delta) + \Delta(\frac{\Omega_1^2}{2} - \gamma B + i\,(B + i\Delta)\,\delta_1 + \delta_1^2)]}{\begin{array}{c}(\Gamma^2 AA^* + i\Omega_1^2\gamma\Delta)(B^2 + \delta_1^2) + \gamma\Omega_1^4 B + \Gamma(\Omega_1^2(\gamma + B)(\gamma B + \delta_1^2) + \\ i\gamma^2 B^2\Delta + i\delta_1^2\Delta(B^2 + \gamma^2 + \delta_1^2))\end{array}}\right], \quad \text{(B.16)}$$

where $A = \gamma + i\delta_1$, $B = \gamma + i\Delta$, and α_o is a constant.